DEVELOPMENT OF SOLUTION-PHASE EXTREME ULTRAVIOLET SPECTROSCOPY AND PHOTOPHYSICS OF μ-OXO-BRIDGED FE(III)PORPHYRINS

BY

KORI MARIE SYE

DISSERTATION

Submitted in partial fulfillment of the requirements
for the degree of Doctor of Philosophy in Chemistry
in the Graduate College of the
University of Illinois Urbana-Champaign, 2021

Urbana, Illinois

Doctoral Committee:

Associate Professor Josh Vura-Weis, Chair
Associate Professor Alison R. Fout
Assistant Professor Hee-Sun Han
Assistant Professor Mikael Backlund

ABSTRACT

A sample delivery method is developed to extend the field of transient M-edge x-ray absorption spectroscopy to study molecular complexes in the solution-phase. A gas-accelerated liquid sheet method is adapted to operate in the vacuum conditions needed for XUV transmission. Gas-generated liquid sheet of chlorinated solvents transmissible to XUV photons are characterized and stabilized under vacuum conditions. A method for measuring the thickness of a liquid sheet *in situ* is described and the high-pressure pumping system for generating the liquid sheet is detailed. The instrument for M-edge absorption spectroscopy is adapted to handle the gas load for the vacuum chambers. The first transmission spectrum of XUV in the energy of 40-90 eV is collected through a flowing liquid sheet of dichloroethane. It is determined that with the noise level present in the liquid sheet, a transient spectrum of a liquid sheet containing FeTPPCl could be collected with a reasonable signal to noise ratio. However, it is found that the liquid sheet of an iron monoporphyrin was unstable in the XUV sample chamber under high vacuum conditions. The transient M-edge absorption spectroscopy technique is also used to probe the excited state dynamics of an iron stacked porphyrin, $(TPPFe)_2O$, oxidation catalyst in the solid state. The relaxation pathway upon photoexcitation at several pump wavelengths is studied to determine the stability and lifetime of the catalytically active Fe(IV)oxo intermediate state. With a combination of optical and XUV absorption techniques, it is found that upon excitation, the stacked porphyrin formed an Fe(II)/Fe(III) containing LMCT state which decays in less than 1 ps. The remaining excited states of the stacked porphyrin are XUV dark and are identified as a relaxing through the pathway containing an Fe(III)TPP+ and Fe(III)TPPO- subunits with the charges on the porphyrin ligand. It is found that the Fe(IV)oxo intermediate state is not observed in these studies and is likely a small percentage of the relaxation pathway.

TABLE OF CONTENTS

CHAPTER 1: Introduction to Ultrafast Extreme Ultraviolet Spectroscopy

1.1 Introduction

Ultrafast M-edge absorption spectroscopy can be used to probe the dynamics of excited states in complexes containing first-row transitions metals.[1] M-edge spectroscopy measures the transitions from the 3p to the 3d orbital of a metal center with extreme ultraviolet (XUV) light from 20 – 100 eV, and is analogous to K-, and L-edge spectroscopy.[1] Both K-edge and L-edge spectroscopies are performed at synchrotrons or x-ray free electron lasers, with time resolutions of picoseconds and femtoseconds, respectively.[2] These user-based facilities offer high photon counts and ultrafast time resolution, but beamtime for these methods is limited. Fortunately, the use of tabletop sources to generate XUV light with femtosecond time resolution has provided a more widely available source of x-ray spectroscopy.[3]

M-edge absorption spectroscopy has been able to study first row transition metal containing complexes in the gas-phase and solid-state at attosecond and femtosecond timescales.[4] This technique has been able to probe magnetic properties of metal complexes[5], spin cross-over dynamics of iron photosensitizers[6], the ultrafast photophysics of metal dithiolate coordination complexes[7], and metalloporphyrins[8,9]. This technique has also been able to study charge transfer and polaron formation in semiconductors and metal oxides.[10,11] This powerful core level spectroscopy has elucidated the excited state dynamics of several complexes with a tabletop technique.

1.2 High Harmonic Generation for XUV Photons

The XUV light used for table M-edge absorption spectroscopy is created through a process called high harmonic generation (HHG). This process creates a continuum of XUV light with peaks at the odd harmonics of the driving laser.[12] The process of high harmonic generation is detailed in Figure 1.1. This process begins by focusing a NIR laser (800 nm) into a semi-infinite gas cell containing a noble gas (Ne, Ar, or He) where coherent pulses of XUV light are produced.[13] This process can be explained with a semi-classical 3 step model.[12] The first step, ionization, is when the intense laser field perturbs the coulombic potential of an electron in a gas molecule, allowing the electron to tunnel through the potential barrier. The second step, propagation, is when the ionized, free electron, is accelerated by the electric field of the laser and gains energy in this process. The final step, recombination, is when the field of the laser changes

sign, the electron is then recombined with the parent ion, and the excess energy is emitted as pulses of XUV light. A continuum of XUV is generated from these pulses. The range of XUV energies is due to the difference in kinetic energy during the propagation step of the model. The cut-off energy of the harmonics can be described by the following equation:

$$E_{cutoff} = I_p + 3.17U_p \approx I_L\lambda_L{}^2$$

where I_p is the ionization potential of the gas atom, U_p is the pondermotive energy of a free electron in an intense field, I_L is the laser intensity, and λ_L is the wavelength of the driving laser.[12] This equation shows that the energy range of XUV generated can be changed based on the gas used and the energy of the driving laser. For example, using Ne gas extends the XUV energy range to 100 eV[9] while using Ar gas can produce more XUV flux in the 30-50 eV range[10]. The driving laser wavelength can be altered with an optical parametric amplifier to increase[14] or decrease[15] the energy range of the XUV continuum. For significant build-up of XUV light to form a continuum, phase-matching conditions need to be met.[16,17] Phase-matching refers to the matching of the phase of the driving laser with the phase of the emitted XUV photons. By using a semi-infinite cell with a loosely focused beam interacting with the gas medium, the area over which the phase-matching occurs is increased and more flux of the XUV photons can be generated.[18,7]

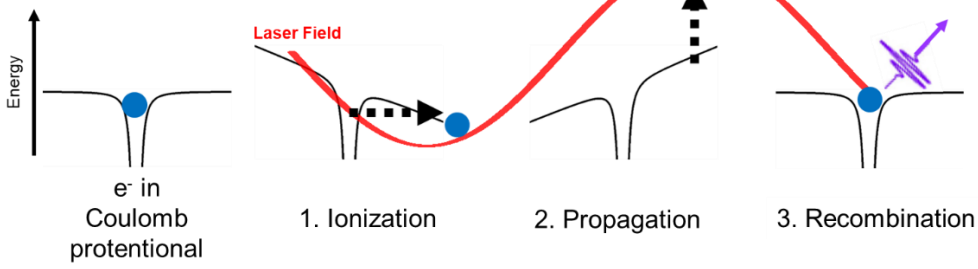

Figure 1.1: Semi-classical model for the high harmonic generation process.

1.3 Tabletop Source of an XUV Continuum

M-edge absorption spectroscopy with XUV photons is performed under vacuum due to the short attenuation length of XUV photons and the strong absorption of XUV light by air. Vacuum chambers need to be operated at high vacuum pressures of 10^{-6} to 10^{-8} torr. The XUV

system used in the Vura-Weis lab is operated in transmission mode and depicted in Figure 1.2.[3] A Ti:Sapphire laser (800 nm, 4 mJ, 35 fs, 1 kHz) is focused into the semi-infinite gas cell, containing Ar or Ne gas, where the HHG process generates pulses of XUV photons. These XUV photons pulses are approximately 20 fs and generate a continuum of XUV between 30 to 100 eV, depending on the noble gas used.[3] At the end of the semi-infinite gas cell, a 0.002 inch stainless-steel shim, with several layers of Scotch tape, separates the gas cell from the HHG vacuum chamber.[19] A small hole is burned through the shim by the driving laser and the gas pressure in the cell is regulated by a pressure-flow feedback system.[3] For this XUV system, the conditions for XUV generation can be tuned to create a semi-continuous XUV spectrum and optimize the flux of XUV photons.[19] The focal position of the NIR laser in the gas cell, the gas pressure, the pulse compression, and the input laser power can all be adjusted to optimize the XUV continuum.[20] After the XUV pulses with the residual 800 nm light pass through the HHG vacuum chamber, the pulses enter the optics vacuum chamber. The beams are reflected off a Silicon mirror and sent through an Aluminum filter which block the residual 800 nm light and the XUV photons greater than 72 eV in energy.[3] The beam is then focused to the sample position with a toroidal mirror. The transmission through the sample is then focused onto a diffraction grating with a second toroidal mirror and dispersed onto a CCD.[3] The resolution of the spectrometer is measured with the absorption peaks of Xe or Xe^+ and is typically 0.3 to 0.5 eV.[19] The bottom portion of Figure 1.2 also shows that part of the driving NIR laser can be diverted to the pump path for the transient XUV system or to a UV/Vis transient absorption system.

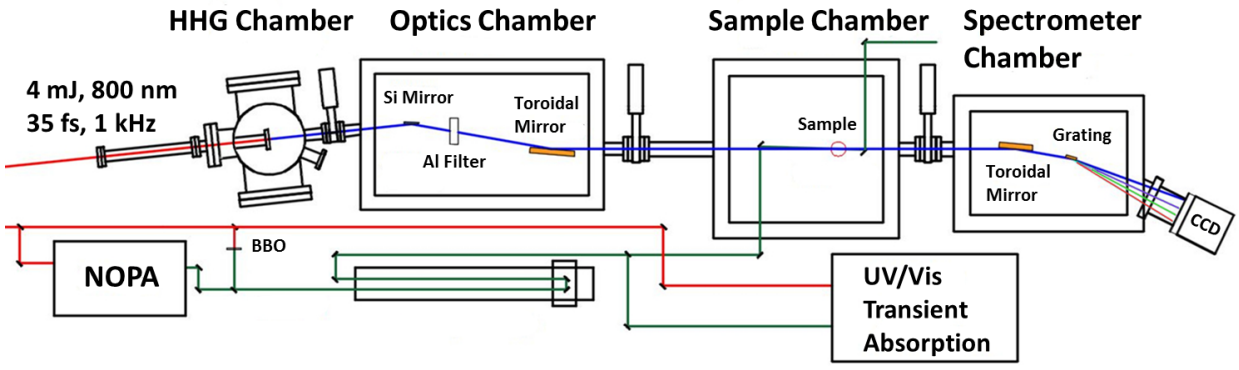

Figure 1.2: Top: Layout of the XUV system vacuum chambers. Bottom: NOPA and 400 nm pump path and pathway to the UV/Vis transient absorption system.[3]

1.4 M-edge Absorption Spectra with XUV Light

M-edge absorption spectroscopy is element-specific and is sensitive to the spin, oxidation state, and ligand field environment of the metal.[3] Figure 1.3a shows the continuum of XUV light with the absorption edges of Fe, Co, and Ni labeled. For M-edge spectroscopy, the dipole allowed transition from the 3p to the 3d valence orbitals allows for an increased absorption cross section of M-edge absorption spectroscopy compared to K-edge absorption spectroscopy.[1] The broadness of the M-edge absorption is smaller compared to K-edge absorption due to the increased lifetime of the final core-hole excited state.[21,7] An M-edge absorption spectra also contains a Fano line shape due to the relaxation pathways of the core-hole excited state.[22,7] Figure 1.3b shows the M-edge absorption spectra of Fe_2O_3 and Ni_2O. The transitions contributing to the absorption featured of the Fe_2O_3 have been detailed in the literature but will be briefly explained.[23] The absorption spectrum of Fe_2O_3 contains a large peak at 57.5 and a small peak at 53.7 eV. This absorption peaks can be predicted accurately using a semiempirical ligand field model.[1] For this model, the Fe^{+3} cation is considered in an octahedral ligand field with the O^{2-} anions.[23] The ground state for this electronic configuration is $^6A_1$ with two, 3p to 3d transitions allowed by spin and dipole selection rules.[23] These two allowed transitions are observed as the two absorption peaks in the Fe_2O_3 spectra. The allowed transitions that constitute an M-edge absorption spectrum for metal complexes can be simulated using programs like CTM4XAS.[24]

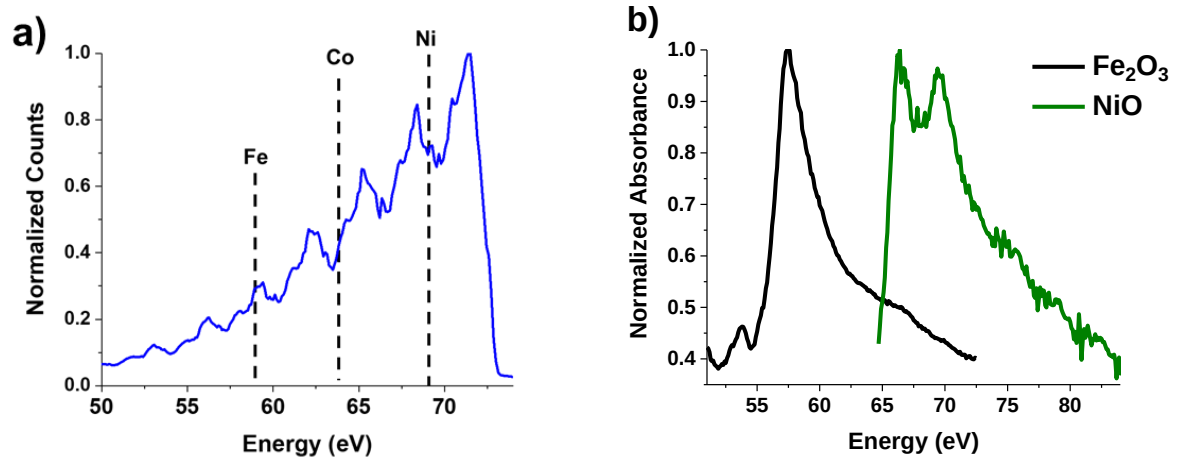

Figure 1.3: a) The continuum of XUV light generated with neon gas with the position Fe, Co, and Ni absorption edges labeled. b) The normalized and scaled absorption spectra of Fe_2O_3 and NiO.

1.5 Conclusion

With the element and oxidation state specificity and ultrafast time resolution of M-edge spectroscopy, this technique is ideal for studying the excited state dynamics of molecular complexes. The second and third chapter of this dissertation will detail how this M-edge absorption technique is being extended to solution-phase samples to study homogeneous catalysts. The fourth chapter will detail how ultrafast M-edge spectroscopy has been used to investigate the excited state dynamics of an iron porphyrin known to catalyze oxidation reaction.

CHAPTER 2: Liquid Sheet for XUV Absorption Spectroscopy

2.1 Introduction

The Vura-Weis group has established that tabletop sources of XUV light can be used to study the ultrafast dynamics of molecular complexes and semiconductors relevant to catalysis and photovoltaics.[9,10,25,6] However, this technique is currently limited to gas-phase and solid-state samples.[4] Solid-state samples can be examined as 5-100 nm thin films on silicon nitride substates. To truly understand the dynamics of a homogeneous catalysts, the complexes needs to be probed in solution.[26] X-ray based techniques used for studying the K-edge and L-edge of metal complexes have been used with solution-phase samples relevant to homogeneous catalysis and redox reactions.[27,28] These studies are done using hard and soft x-rays available at synchrotrons or free electron lasers (XFELS).[29] Expanding tabletop XUV sources to study solution-phase samples will allow for the study of molecular complexes with a more widely available soft x-ray source.

2.2 Requirements for Solution-Phase M-edge Spectroscopy

One of the main hurdles to studying molecular complexes in the solution-phase with XUV absorption spectroscopy is preparing a sample thin enough to transmit a detectable amount of XUV photons. The short attenuation length of XUV light and a low photon flux of the tabletop source limits the number of photons that can transmit through the sample. To determine the type of solvent and required pathlength required, the absorption of several solvents by XUV light (40-80 eV) were simulated using the atomic scattering factors.[30] The pathlength of a solution-phase sample needs to allow enough XUV photons to transmit to allow for an acceptable signal to noise ratio for transient XUV experiments. The transmission through 100 nm of Si_3N_4 is used as the benchmark for allowable XUV transmission because it is the substrate used for many of the solid-state ground state and transient XUV experiments.[3,10] Simulated data show that chlorinated solvent with a pathlength of 500 nm were about as transmissive as 100 nm of Si3N4 in the XUV range of 40 – 80 eV, shown in Figure 2.1. Specifically, for a 500 nm solution of 50 mM FeTPPCl in $CHCl_3$, about 2.5 x 10^5 photons/s/.1eV can transmit through the sample. This requires only 10 hours of data collection to achieve a signal to noise ratio of 5:1 for the expected transient signal.

For the tabletop XUV light source, there is a spatial chirp in the XUV beam which interacts with thickness variations in samples and can create artifacts in absorption spectra that obscure true absorbance peaks.[31] Therefore, a solution-phase sample for XUV absorption needs to have minimal thickness variations to avoid errors in the absorption spectra. The short attenuation length requires that the XUV absorption spectroscopy technique operates under high vacuum conditions. Therefore, the submicron thin solution-phase sample must be stable under vacuum conditions. Various methods have been developed for soft x-ray absorption techniques for operating a solution-phase sample and will be detailed in the next section. A solution-phase sample delivery method needs to be developed that is compatible with the tabletop XUV source for M-edge spectroscopy.

2.3 Background of Solution Phase Sample Methods for X-Ray Spectroscopy

Various methods have been developed to flow liquid sample through vacuum at micron to submicron thicknesses for soft x-ray absorption spectroscopy. Liquid flow cells have been developed that can operate under vacuum conditions.[32,7] These methods are advantageous because a low flow rate is needed for the cell and only a small amount of sample is required for data collection, which can be easily recycled. These flow cell methods use Si_3N_4 windows to separate the liquid flow from the surrounding vacuum. However, the windows significantly cut the XUV transmission.[7] Flow cell methods must be modified to prevent the windows from bowing outwards towards vacuum and drastically increasing the pathlength. This results in further loss of the XUV transmission.[7] The low XUV transmission significantly increases the noise and limits the ability to measure the M-edge absorption spectra of a sample.

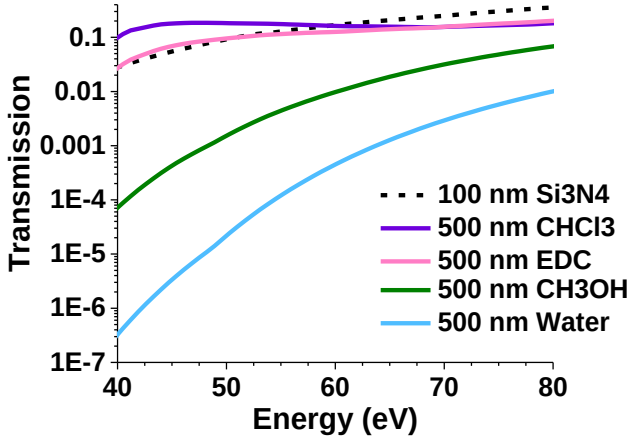

Figure 2.1: The simulated transmission of liquids and Si_3N_4 in the XUV range of light.[30]

For hard x-ray absorption spectroscopy, cylindrical jets are used to deliver liquid phase samples. The thickness of the jet can be up to 50 microns which is too thick for soft x-ray experiments. In 2015, one of

the first sheet jet liquid delivery methods for vacuum conditions was introduced in by Ekimova et al. for use at the synchrotron radiation source BESSY II at the Helmholtz-Zentrum in Berlin.[33] This method was developed to perform transmission mode soft x-ray absorption spectroscopy which requires a submicron to few microns sample thickness. This method created a sheet jet solution-phase sample by colliding two angled liquid jets to form a thin leaf-like sheet upon collision. A thin sheet is formed from the laminar liquid jets with high Reynolds due to the surface tension of the liquid and fluid inertia with a thick rim that is orthogonal to the plane of the colliding jets.[33,34]

Inspiration for this method came from free falling sheet jets that have been used for decades in CW dye laser systems for reducing lasing thresholds and maintaining long term stability.[35,36] With this sheet jet method, soft x-ray absorption spectroscopy of the nitrogen K-edge of an aqueous solutions of NH_4^+ was performed. The thickness of a flowing sheet jet in vacuum has been measured using interferometry.[37] A disadvantage for this method of sample delivery is that a liquid flow rate between 3 mL/min and 6 mL/min is required to generate the liquid sheet. This high flow rate requires liters of sample solution for an experiment that is hours long, which is infeasible for samples produced on the milligram scale. Sample recycling has been implemented to mitigate the large volumes required to supply the high flow rate.[33,38] A liquid sheet jet sheet was used to determine the absolute absorption cross section at the L-edge of dilute Manganese complexes.[38] A liquid sheet has also been used to perform x-ray absorption spectroscopy at Cr L-edge. The L-edge of $Cr^{III}(acac)_3$ in an ethanol solution was measured and the absolute absorption cross section was calculated.[39]

Liquid sheet jets have been used with tabletop femtosecond soft x-ray sources to study organic molecules and inorganic salts in aqueous solutions in Kleine *et al*[40] and Smith *et al*[14]. The HHG source for these studies produces pulses in the energy range from 220 to 450 eV. Liquid sheet jets were used to probe the absorption at the oxygen edge (expanding the to water-window range, 284-538 eV) using a tabletop HHG source.[14] The molecules studied with transient soft x-ray absorption were between the carbon (~280 eV) and nitrogen (~400 eV) K-edges.[40] This study is the first transient soft x-ray spectra of a liquid-phase sample in the water-window region using a colliding sheet jet with a thickness near 600 nm. For the study in Smith *et al*, the strong-field ionization of ethanol and methanol and the excited state dynamics at the

carbon K-edge were monitored.[14] While these studies have shown that solution-phase samples can be probe with tabletop generated XUV photons, it has not been shown that solution-phase samples can be used in the 40-80 eV range of XUV photons used for M-edge spectroscopy.

Recently, a research team at the Linac Coherent Light Source (LCLS) at the SLAC National Accelerator Laboratory developed a method of generating submicron thick liquid sheets that are stable in vacuum[41]. These sheets are generated using a microfluidic chip with a central channel for liquid flow and two channels that collide Helium gas flow with the central channel. The colliding gas channels use gas acceleration to form the liquid sheet from the central channel. The liquid sheet is formed at the tip of the nozzle and is a leaf-like shape that can be up to 1 mm long and 500 nm wide (depending on the solvent used) with thick boundaries of flowing liquid and a submicron thin inner section. The implementation of the gas acceleration allows for the control of the liquid sheet width and thickness, which is unavailable with the colliding jet. With the microfluidic chip, free-flowing liquid sheets with thickness down to 10-50 nm can be formed with flow rates less than 0.5 mL/min. The microfluidic chip was made by Micronit Microtechnologies BV using standard hard lithography. The angle of the converging gas channels and the distance from the point of channel convergence to chip exit was optimized to form the micron to submicron sheet thickness. The microfluidic chip contains a central channel that narrows near the exit and two colliding channels that narrow near the exit. With this technique, the Fe L_3-edge absorption spectrum for 100 mM $Fe(CN)_6^{(3-)}$ was measured at LCLS. The spectrum matches the transmission of the solution in a static flow cell.

2.4 Guide for Using Gas-Accelerated Sheets with Chlorinated Solvents

The gas-accelerated sheet[41] developed by scientists at LCLS and produced using microfluidic chips was chosen for the XUV system over a colliding sheet-jet[33] because the gas-accelerated sheet allowed for the tuning of the sheet to submicron thicknesses and a flow rate under 0.5 mL/min. This low flow rate ensures that smaller volumes of precious samples can be used for hours long experiments. Because the XUV system in the Vura-Weis laboratory does not have a bottom flange output a liquid recovery apparatus that prevent liquid from accumulating in a vacuum chamber cannot be easily installed. Without a liquid recovery system, method of the colliding jets to form a sheet jet is not feasible due to greater than 4 mL/min flow rate required to

form the jet. The lower flow rate of the gas-accelerated liquid sheet will allow for smaller amount of liquid accumulated in the vacuum chamber.

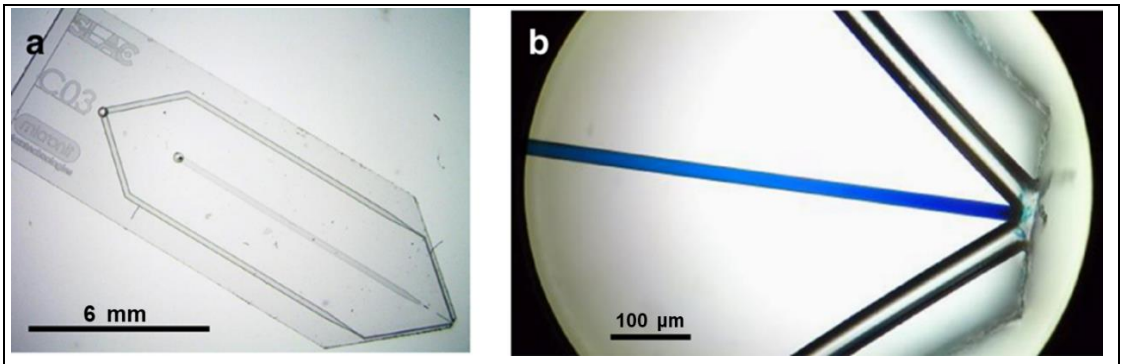

Figure 2.2: The borosilicate microfluidic gas-dynamic chip developed by LCLS and produced by Micronit Technologies. A) The chip dimensions are 6 by 19 mm and the input for the gas and liquid channels are on the underside of the chip with the upside of the chip containing the letterings from left to right. The left most channel input contains channels that meet at the nozzle of the chip. The right most channel feeds to the center of the nozzle. B) Depicted is a close-up of the nozzle of the chip. The central channel contains blue dye and starts from the right most channel. The converging channels start from the left most channel (the figure is adapted from reference 41).

The microfluidic gas-dynamic chip, depicted in Figure 2.2, contains a central channel that leads to the nozzle of the chip and outer channels and converge of the tip of the nozzle with the central channel. The colliding channels converge with the central channel at an angle of ±40° at the exit of the nozzle. A liquid sheet is formed from a central liquid channel and colliding gas channels at the output of the chip nozzle. The three channels meet at the narrowing tip of the nozzle where the liquid sheet will form. The central and colliding channels contain ports that align with the exit of liquid and gas channels of a PEEK holder developed by Neptune Fluid Flow Systems LLC.

Depicted in Figure 2.3 a) is the PEEK holder mounted on an optics post with the output channels facing upwards. The PEEK holder is 1'' x 1'' x 0.5'' and contains a face to hold the microfluidic chip. This front face of the holder contains the output channels which are holding the viton o-rings. The transparent microfluidic chip is placed in the cutout with the ports of the chip and the out channels of the holder aligned. Figure 2.3 b) shows the assembled chip and holder mounted in a post holder. An aluminum plate is fastened to the holder with two screws.

This plate compresses microfluidic chip onto the o-rings with inputs of the liquid and gas channels of the chip aligned to the holder outputs. The o-rings used are viton with a durometer of 75 with a cross section of 0.023 in, an inner diameter of 0.041 in and outer diameter of 0.087 in. Viton gaskets were used because of the chemical compatibility with chlorinated solvents.

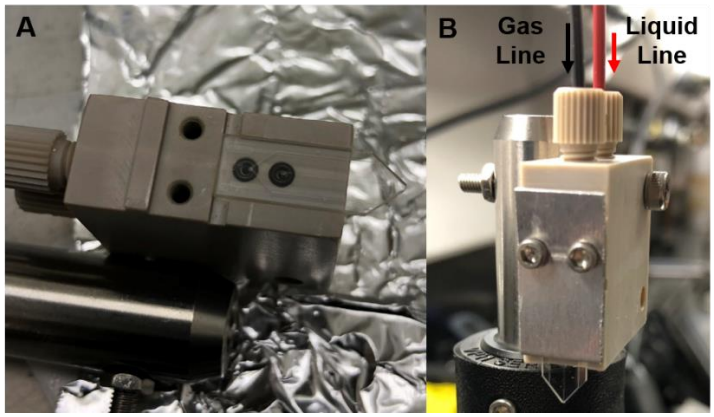

Figure 2.3: a) PEEK holder mounted to an optics post. The output top and bottom channels of the PEEK holder contain o-rings in the groves. The transparent microfluidic chip is place in the insert for the chip and the chip input channels are aligned with the holder output channels. b) The holder and chip secured with an aluminum face plate. The top of the holder has a front gas line and a back liquid line. The microfluid chip is visible extruding from the bottom of the faceplate and holder interface.

The top of the holder contains two Upchurch fittings screwed into the input ports of the holder. The input port closest to aluminum plate flows to the output port closest to the screw holes on the front face of the holder. The input port further from the aluminum plate flows to the output port further down the face of the holder. The purpose of the holder is to secure the microfluidic chip and allow for liquid to flow with the holder to the central channel of the chip and for gas to flow through the holder to the colliding channels of the chip. The PEEK holder contains a face where the microfluidic chip is input and a top with two tapped holes for up-church connections.

A liquid sheet is generated through a gas acceleration process using the microfluidic chip. The generation process with Helium gas flow and water is depicted in Figure 2.4.[41] Helium is used as the accelerating gas because it is soft x-ray transmissive and does not freeze in the liquid nitrogen cold trap.[42] In the top figure, on the far left, a jet of liquid is formed by flowing water through the central channel of the microfluidic chip. With the flow rate of the water help constant, the gas flow of Helium is slowly increased through the colliding channels. The change in images from left to right show how the jet changes and how a sheet is formed as the He gas flow is increased. The sheet is formed from the collision of the gas flow with the jet of liquid. Increasing the gas flow spreads out the plane of the sheet. The center of the sheet has a thickness that can be tuned from a few microns to submicron thickness depending on the rate of gas flow

used. The sheet is surrounded by a thick boundary. The underlying physics of the gas accelerated sheet formation is similar to the formation of the liquid jets discussed previously.[33]

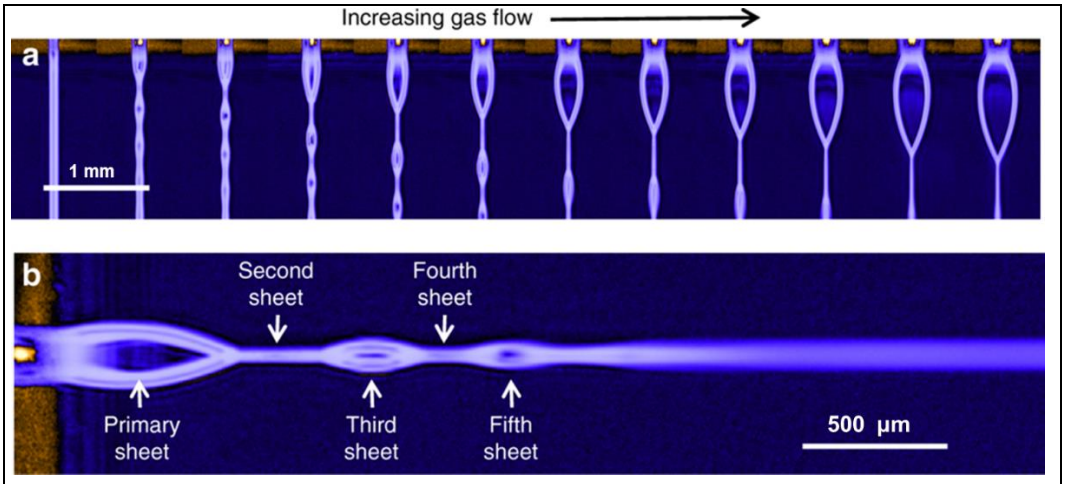

Figure 2.4: The creation of the sheet with the microfluidic chip (Figure adapted from ref 41).

Both the central and colliding channels of the chips are prone to clogging at the narrowing of the channels near the nozzle of the chip. Currently, the clogs cannot be removed and the chips are unusable after clogging. Due to the microfluidic channels, great care must be taken to prevent particles from entering the liquid or gas lines during assembly. Clean and fresh gloves were used when assembling the liquid and gas lines. Fresh aluminum foil was placed on the bench top for a clean working surfacing while assembling the holder, gas lines, and liquid lines. All fluidic connections, gas connections, and holder were sonicated in Millipore filtered water for 20 minutes. The pieces were air-dried on fresh aluminum foil. A Precolumn PEEK Filter (IDEX, A-335) was used for both the liquid line and gas line. For the liquid line, a PEEK Frit 2 µm .125" x .065" x .250" (IDEX, A-704) is used as the filter because the small porosity will prevent large particles from entering the liquid line and

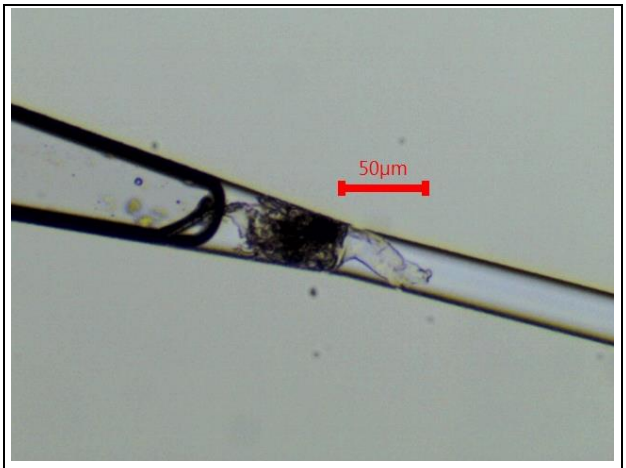

Figure 2.5: Image of clog in the central channel of a Micronit microfluidic chip as the channel narrows from 200 µm to 30 µm towards the nozzle of the chip. The liquid present is chloroform and the particle lodged in the channel is unknown.

clogging the central channel of the chip. A 2 μm PEEK Frit filter was found to be more effective at prevent clogging than a 10 μm PEEK Frit filter. For the gas line, a stainless-steel frit (IDEX, A-107) was used due to the long filtration lifetime and was found to be sufficient at preventing clogging. It was found that the central line with liquid flow would clog more frequently than the colliding channels with gas flow. After attaching the liquid and gas lines to the holder and before inserting the chip, solvent and gas were flowed through the lines for several minutes to allow for any particulates to flow through the line.

To flow the solvent through the chip to form the liquid sheet, initially an HPLC pump was used. The pulsation from the HPLC dual pumps caused uncontrollable thickness changes in the liquid sheet which is not acceptable for XUV absorption studies. The pumping source was changed to a high-pressure syringe pump (Chemyx Fusion 6000 high-pressure syringe pump) with a 200 mL stainless-steel syringe. A stainless-steel syringe with viton o-rings were chosen because of their resistance to the chlorinated solvents used to generate the liquid sheet. Using a high pressure syringe pump has been shown to produce stable liquid flow for radiolysis experiments.[43] Using high-pressure syringe pump, the sheet formation was stable for several hours at atmosphere and there were not pulsations that destabilized the sheet.

To collect a ground state spectrum of a liquid sheet sample, the solution flow for the liquid sheet needs to alternate between a reference solution and a sample solution. To achieve this, two high-pressure syringe pumps were used, one with a reference solution and one with the sample solution. A switcher was used so that two syringe outputs could be attached to a device with one output to the liquid line to the vacuum chamber. The switcher could then be used to manage the flow of liquid into the vacuum chamber. A 6 Port DuraLife Switching Valve (IDEX, MXP7900-000) was used for the liquid flow to the liquid sheet so it could be switched back and forth between a reference of pure solvent solution and a concentrated sample solution. This switcher was chosen to minimize a pressure change when switching between pumps. Any pressure changes of the solution flow to the liquid sheet would change the thickness of the liquid sheet. The switcher was also chosen because the liquid contact components are compatible with the chlorinated solvents used.

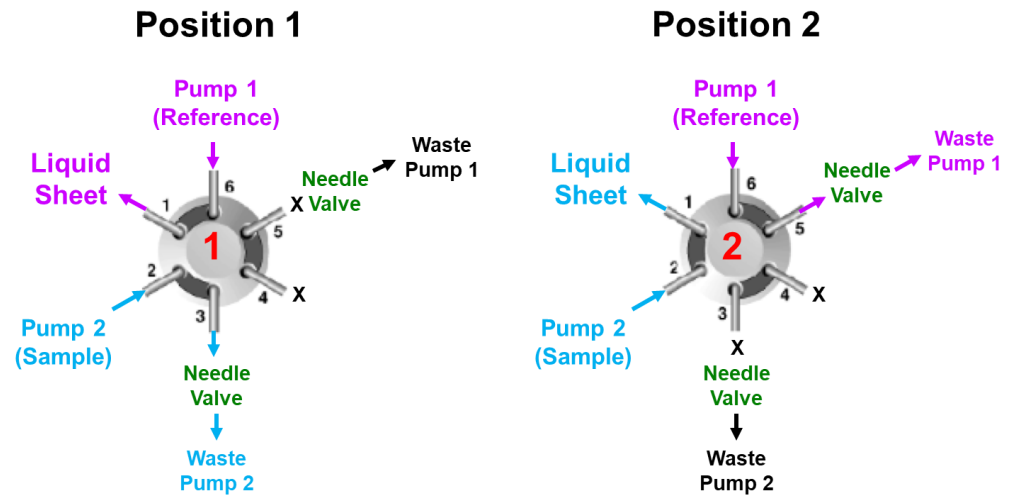

Figure 2.6: Switching Diagram used for the two high pressure syringe pumps with the 6 Port DuraLife Switching Valve showing the flow patterns between the two valve positions. Left is switcher "Position 1", used to flow the reference solution from syringe "Pump 1" to the liquid sheet line. Right is switcher "Position 2", used to flow the sample solution from syringe "Pump 2" to the liquid sheet line (image modified from an IDEX data sheet).

The inputs of the switcher were designed to allow for easy alternation between the reference and sample solutions for ground state absorption studies. The switching diagram from Figure 2.6 shows the two positions the switcher can be set to with the two syringe pumps, one output to liquid sheet, and two waste out puts connected (the sixth output is not needed and stoppered). The "Position 1" is used to flow the reference solution from syringe "Pump 1" to the liquid sheet line. At the "Position 1" the liquid from syringe "Pump 2" is sent to the "Waste Pump 2" outlet. There is a needle valve used before the "Waste Pump 2" outlet so that the needle valve can restrict the liquid flow and maintain the high backing pressure needed to form a liquid sheet. This high backing pressure is maintained with the needle valve so the when the switcher position is change from "Position 1" to "Position 2" there will be enough backing pressure in syringe "Pump 2" to generate a liquid sheet. At the "Position 2", the liquid from syringe "Pump 2" will flow to the liquid sheet output and generate a liquid sheet. The liquid flow from syringe "Pump 1" will then flow to "Waste Pump 1" through a constricted needle valve to maintain a high backing pressure for syringe "Pump 1". With a high backing pressure maintained in both syringe pumps, the switcher position can be alternated back and forth with little disruption to the flow and thickness of the liquid sheet. When switching between liquid flow from one syringe pump to another, it was found to approximately 5 minutes were needed from the moment of

switching to when the solution of the new pump would flow completely through the liquid sheet. This 5 minute window is the time it takes for the solution from the second syringe pump to travel through the tubing and connections from the syringe pump to the chip holder. The time window will vary depending on the tubing length and connections used.

The procedure for taking a ground state XUV spectrum of a sample requires the concentrated solution of the sample in pump 2 and a solution of the reference solvent in pump 1. While transmitting XUV through the liquid sheet, the liquid flow will need to be switched back and forth between pump 1 and pump 2 to collect the sample transmission and reference transmission. It is important to collect the transmission through the sample and the reference as close in time as possible to generate an absorbance spectrum due to the instability of the XUV source. Noise can be introduced into the spectrum if the reference and sample spectrum are not taken within a few minutes of each other.

2.5 Calculation of the Liquid Sheet Flow Velocity

To determine the rate at which the solution in the liquid sheet is refreshed, the flow velocity of the liquid jet was determined at the output of the chip nozzle. The flow velocity can be determined using the volumetric flow rate and the diameter of the exit point of the chip nozzle. A typical volumetric flow rate (Q) used to generate a liquid sheet is 0.22 mL/min and the output diameter of the chip nozzle (ø) is 0.13 mm. The flow velocity (v) is determined on the following formula:[44]

$$v = \frac{Q}{\pi * \left(\frac{\emptyset}{2}\right)^2}$$

For a solution with a flow rate of 0.22 mL/min, the flow velocity of the sheet is 276 mm/s (or 276 μm/ms). In our instrument, the XUV probe and is ~100 μm in diameter and the visible pump is set to ~200 μm diameter. This flow rate therefore ensures that a new sample volume is pumped/probed with each shot of the 1kHz laser.

2.6 Thickness Determination for Chlorinated Sheet Generation

Since the liquid sheet needs to be a submicron thickness to ensure enough XUV photons can be transmitted to collect an XUV absorption spectra, it is essential to measure the thickness of a liquid sheet. Several studies have used interference methods to determine the thickness of a

flowing liquid sheet.[45,33,37,41] An advantage of monitoring the reflected interference patterns of the liquid sheet is that the thickness can be determine in situ by comparing the colored bands to the simulated colored bands of the solvent at a given thickness.

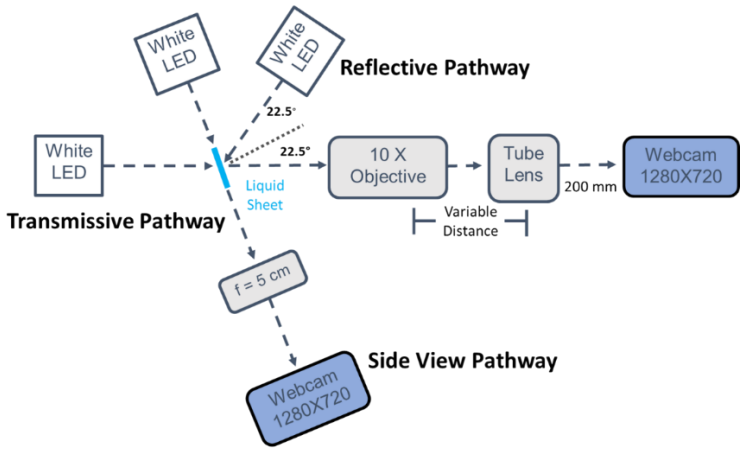

Figure 2.7: The imaging pathways used in the test chamber. The reflective imaging pathway uses a white LED flashlight as a white light source. This light source is reflected off the flowing liquid sheet at a 22.5° angle from normal incidence. The light then travels through a 10X objective, then through a tube lens, followed by the light focusing onto a webcam. The transmissive imaging uses a white LED flashlight and imaging the plane of the liquid sheet. This pathway transmits light through and around the liquid sheet and directs the light through the 10X objective, tube lens, and onto the webcam. The side view imaging pathway uses a white LED flashlight as white light source and has the light traveling parallel to the plane of the sheet. The light is then focused through a planoconcave lens (f = 5 cm) onto a webcam.

The imaging pathways used to view the liquid sheet are depicted in Figure 2.7. A 10x magnification infinity corrected objective (Mitutoyo, MY10X-803) with a long-range working distance of 34 mm was used. The image is then focused with a tube lens for wide field imaging with a focus length of 200 mm (Thorlabs, ITL200). The tube lens focuses the image onto a camera (Logitech, C270). These optics were chosen so the sheet can be magnified with 1 µm resolving power based on the objective chosen. These infinity-corrected optics also allow for the distance between the objective and the tube lens to vary without affecting the quality of the image. This also allows for the objective to be in vacuum chamber near the flowing sheet while the tube lens is several inches away from the objective and out of the vacuum chamber. Both the reflective imaging pathway and the transmissive imaging pathway feed into the objective and onto the same webcam. Only one pathway can be used at a time to ensure the image quality. The purpose of the transmissive pathway is to observe any droplets or particles are present on the nozzle while the sheet is running. The transmissive pathway is also used to align the microfluid chip to the webcam and to adjust the focusing of the objective or tube lens.

The purpose of the sideview pathway is to image the nozzle of the chip as a sheet is flowing. Imaging the nozzle helps to understand the stability of the sheet under vacuum

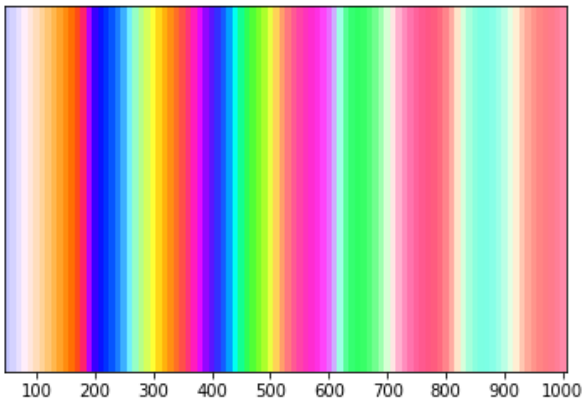

Figure 2.8: Simulated colored bands of chloroform with unpolarized light at a 22.5° angle.

conditions. The droplets that form and interact with the sheet can be observed and the conditions that cause the droplet formation and sheet instabilities can be noted. The purpose of the reflective imaging setup is to image the reflected interference bands of the running liquid sheet. When reflecting the white light from a running liquid sheet, the interference patterns can be imaged from the sheet like in Figure 2.9. The colored bands are the thin-film interference fringes due to the constructive and destructive interference of light being reflected by the planes of the submicron thin liquid sheet.[46] This method for thickness determination was used in the first characterization as a gas-accelerated liquid sheet with water as the solution.[42] For that study, the simulation of the color due to the thin-film interference of water was compared to the running water liquid sheet. The thickness of the running liquid sheet was determined by matching the color of the liquid sheet band to color of the simulated band. For XUV transmissive solutions like chloroform and dichloroethane, the color of reflected interference for the varying solvent thickness was determined by calculating the spectral reflectance spectrum for each thickness of solvent.[47] Each thickness spectrum is then converted to a color based on the International Commission on Illumination (CIE) color matching functions.[48] Figure 2.8 shows the simulated colored bands of chloroform reflected at a 22.5° angle from 50 nm to 1000 nm thick.

The angle of reflection for the simulation is that used for the reflective imaging pathway. This angle value was chosen so that the angle would be wide enough to enough for optics and the light source would not be in the way of the transmissive imaging pathway or in the way of the object. The simulated color at each thickness of chloroform can be compared to the color of the reflected interference bands of a liquid sheet of chloroform to determine the thickness of the liquid sheet at the band. Figure 2.9 shows a chloroform sheet formed at atmosphere compared to the simulated chloroform colors ranging from 50 nm to 1000 nm. Arrows are used to show areas where the reflected color and simulated color qualitatively match. The liquid sheet of chloroform is shown to have band corresponding to approximate thicknesses of 150 nm, 250 nm, 375 nm, and 675 nm. This thickness determination method has shown that in atmosphere, liquid sheets with a desired thickness near 500 nm can be formed.

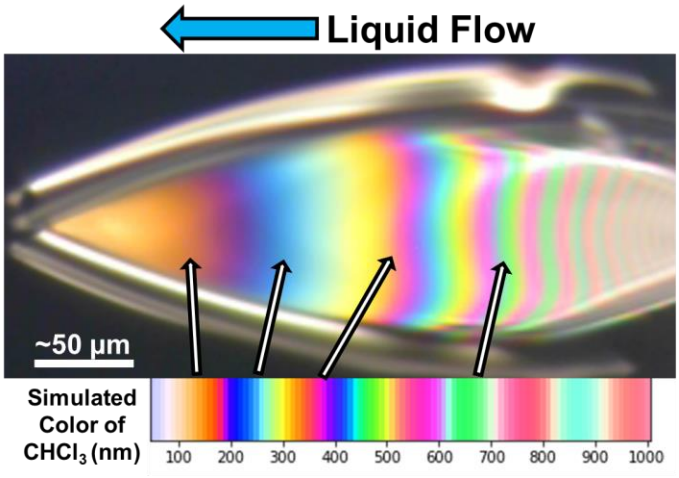

Figure 2.9: The chip nozzle is on the right side of the image of each sheet with the liquid flowing from the right to the left. A chloroform liquid sheet (0.14 mL/min) formed at atmosphere. The color of the sheet is compared to the simulated color based on the thickness showing that the sheet ranges from about 200 to 500 nm on the left side of the sheet.

2.7 Design of a Cold Trap and Liquid Sheet Test Chamber

To study the formation of liquid sheets of chlorinated solvents under vacuum conditions, a test chamber was designed to accommodate the materials needed for liquid sheet generation including vacuum feedthroughs for the gas and liquid lines detailed above for the liquid sheet generation. A custom 10'' conflat (CF) flange was designed with multiple ports for the cold trap, differential pumping, and liquid/electronics feedthroughs. The cold trap is composed of a 1 1/3'' CF flange nipple to a 1 1/3'' CF to 2 ¾'' CF zero length reducer. The reducer is connected to a 2 ¾'' stainless-steel nipple. The cold trap is capped with a 2 ¾'' aluminum flange for improved thermal conductivity. One end of a copper bar is connected to the aluminum flange and the other end is connected a copper container with a volume of 289.5 mL. The large volume of the copper container is designed so that a liquid sheet of chloroform can run continually in vacuum for up to

12 hours before needing to empty the container. This will allow enough time for transient spectroscopy of a liquid sample to occur which can require several hours of data collection to achieve a sufficient signal to noise ratio.

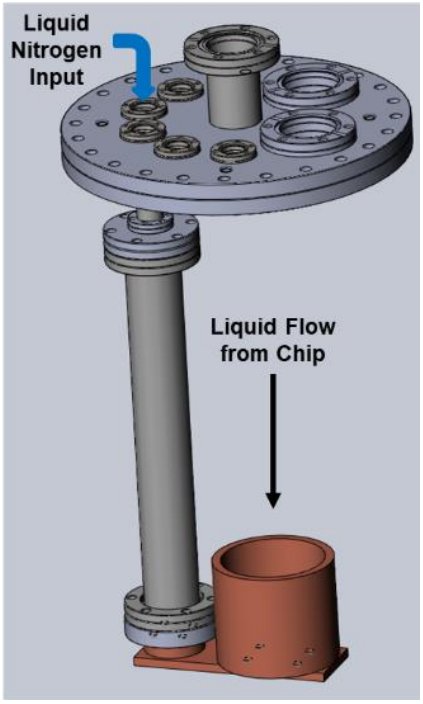

Figure 2.10: The stainless-steel flange designed with multiple ports. The CAD drawing of the custom 10 in stainless-steel (SS) conflat (CF) flange with cold trap assembly attached to a CF flange on the underside of the 10 in CF flange. The cold trap assembly consists of a SS nipple capped at the bottom with an Al flange. The copper rod attaches a copper catcher on a copper bar to the Al flange. The SS nipple insulates the liquid nitrogen (LN2) while the Al flange transfers the heat from the copper components and cools the copper pieces. The liquid flow into the microfluidic chip will be collected and cooled into the copper collector so that the liquid does not evaporate and increase the pressure of the vacuum chamber.

The copper cold trap is designed so that it can fit into the sample chamber of the XUV system. The XUV sample chamber is a 26'' x 25'' stainless steel box with a lid with a 10'' CF blank flange. The chamber sits atop a laser table, preventing a way of having an opening in the bottom of the chamber to allow the liquid from the liquid sheet to be removed from the chamber. Because the liquid from the liquid sheet cannot be removed and needs to stay in the vacuum chamber, it is essential to collect and freeze the liquid. Freezing the liquid will prevent the evaporation and increase in chamber pressure.[41] The cold trap assembly is mounted onto the bottom of the 10'' CF flange for the lid of the XUV sample chamber or the vacuum test chamber. Liquid nitrogen is poured through the port on the 10'' flange into the stainless-steel nipples and the bottom aluminum flange. The 2 ¾'' stainless-steel tube acts as a dewar (with relatively poor thermal conductivity to the 10" flange) while the aluminum flange acts as a conductor and transfers the heat from the copper pieces into the liquid nitrogen allowing for the copper pieces to cool down.

Figure 2.11 depicts the test chamber used to conduct the experiments needed to test the stability of the liquid sheet under vacuum conditions. The optics post that holds the chip is fed through the opening of the XYZ manipulator and then attached to the flange and secured to the XYZ manipulator. The XYZ manipulator used is a multi-axis motorized manipulator with a 2.75'' flange (Huntington Mechanical Laboratories, MPM-275-

4Z). The manipulator contains a bottom flange that attaches to a vacuum chamber and top flange that can be moved by the multi-axis motors. The top and bottom flanges are connected with a flexible connection that allows the top flange to travel 1.5 inch horizontally the X and Z direction and 4 inches vertically in the Y direction. This manipulator can maintain ultra-high vacuum pressures and allow for the chip to be moved while operating under vacuum.

The stainless-steel lid contained a central, raised 2.75-inch flange where the XYZ manipulator was mounted. A small table jack was used to support the weight of the manipulator after it was mounted to the chamber. The stainless-steel lid also contained two 2.75-inch flange opening and six 1.33-inch flange openings. One of the 2.75-inch flange ports is used for the flange containing the connections to the gas and liquid lines. The second 2.75-inch flange port is used for a connection to the roughing line for when the lid is used on the sample chamber of the XUV instrument. One of the six 1.33-inch flange ports is used for a thermo couple connection so that the temperature of the copper cold trap can be monitored. The 1.33-inch flange port that contains a 1.33-inch flange port on the underside of the stainless-steel lid is used to mount the cold trap. Liquid nitrogen is poured down this flange opening to cool the cold trap. A funnel is used to control the flow of the liquid nitrogen and prevent back-splashing.

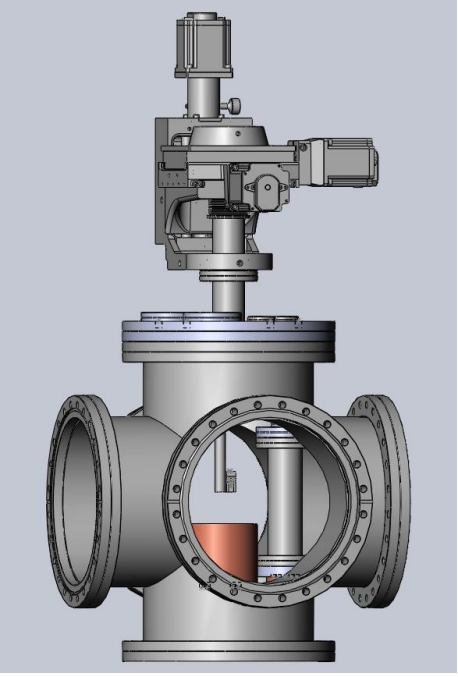

Figure 2.11: A CAD assembly of the test chamber for generating liquid sheets under roughing vacuum. A six-way 10'' stainless steel cross is used as the vacuum chamber. The stainless-steel lid with the mounted cold trap (depicted fully in Figure 2.10) is top atop the test chamber with the cold trap suspended from the lid. Atop the stainless-steel lid is the XYZ manipulator used to move the positive of the holder and chip. The chip is attached to an optics put which is mounted to a 2.75 in flange which is attached to the XYZ manipulator.

2.8 Stabilization of Chlorinated Solvent Sheets Under Vacuum

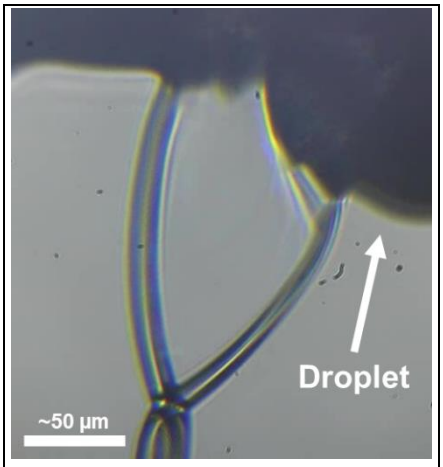

Figure 2.12: Liquid sheet of chloroform (0.2 mL/min) in vacuum (10^{-1} Torr). The sheet is unstable and interacting with the droplets of chloroform that accumulate at the nozzle of the nozzle of the chip. Image taken in transmission mode to show the droplet.

To determine if a stable liquid sheet of a chlorinated solvent with submicron thickness could be formed under vacuum the test chamber described above was used to form liquid sheets at roughing vacuum pressures (~10^3 Torr). The conditions of solvent flow and backing gas pressure were needed to determine which conditions are needed to form a stable sheet. Figure 2.11 shows a liquid sheet of chloroform formed under roughing vacuum pressures. The image is taken in transmission mode to show the droplet that is formed on the nozzle of the chip. The droplet interferes with the chip and the sheet is askew. During this experiment, the sheet thickness was monitored with the reflective imaging of the interference bands, and it was found that the thickness of the liquid sheet changed rapidly as the droplets were formed. The conditions of the liquid sheet generation were changed, and it was found that the sheet was more stable under vacuum when the flow rate was increased from 0.2 mL/min to 0.35 mL/min. However, droplets would periodically form and interfere with the liquid sheet. It was been shown that a perturbation of the edge of a liquid sheet disturbs the sheet formation and can lead to the sheet breaking.[49] Therefore, it is essential to determine the conditions required to form a sheet that prevents the formation of disruptive droplets.

The microfluidic chips used contain a silane-based hydrophobic coating. The hydrophobic coating of the chip was successful for the formation of aqueous liquid sheets.[41] The effect of the hydrophobic coating on the formation of chloroform droplets of the nozzle of the chip was tested. Several types of oleophobic coating were attempted with the microfluidic chip to repel the chlorinated solvents.[50] Three types of oleophobic coating, detailed in the supporting information, were applied to the microfluidic chips. However, there was no improvement in the stability of the chloroform liquid sheet under roughing vacuum using these coatings. The microfluidic chips were then plasma cleaned to remove the outer lay of the hydrophobic coating.[51] Figure 2.13 shows a liquid sheet of chloroform under roughing vacuum. The sheet was stable for several hours under roughing vacuum.

Figure 2.13 shows the transmissive image of the chip and chloroform running and small droplets can be seen on either side of the sheet at the nozzle of the chip. It was found that these small droplets formed and persisted throughout the liquid sheet generation, however, the droplets did not move and did not interfere with the liquid sheet. Figure 2.14 shows the reflect imaging of a chloroform liquid sheet under roughing vacuum conditions. This chloroform liquid sheet was formed with a flow rate of 0.4 mL/min with He used to generate the sheet. Figure 2.14 also contains the image of the simulated color for the reflection of chloroform at thicknesses from 50 nm to 1000 nm. Arrows are drawn to show where the reflective band of the sheet corresponds to the simulated color based on the chloroform thickness. Therefore, the arrows point to the sections of the chloroform liquid sheet that are approximately 400 nm, 475 nm, and 550 nm in thickness. These corresponds are the ideal thickness needed to transmit approximately 10% of the XUV photons through a liquid sheet of chloroform.

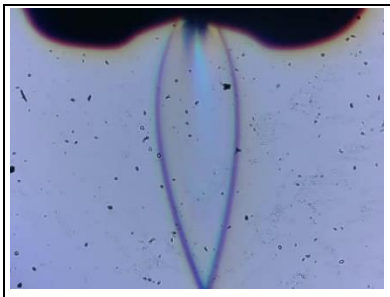

Figure 2.13: Chloroform sheet with He gas flow. The sheet is flowing from a chip that has been recently plasma cleaned. The small droplets on the nozzle are not interfering with the sheet and the sheet is stable (the black speckles are imperfections and dust particles on the webcam).

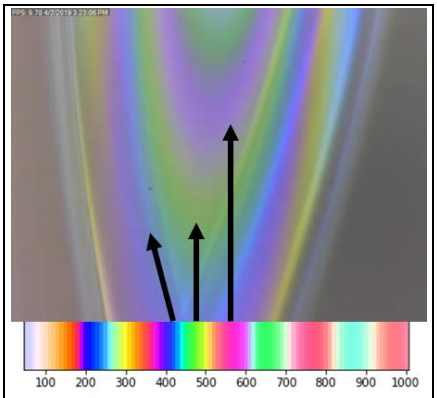

Figure 2.14: Chloroform sheet at 0.4 mL/min from a plasma cleaned chip under roughing vacuum. The bottom section of the image is the simulated color for the reflection of chloroform at thicknesses from 50 nm to 1000 nm.

2.9 Conclusion

To truly understand the impact of the solvent environment on the excited state dynamics of molecular complexes with M-edge spectroscopy, a solution-phase sample delivery method needs to be developed. While solution-phase methods have been developed for soft x-ray techniques and some tabletop XUV sources, none have been developed for the energy range of 40-100 eV. A gas-accelerated liquid sheet method has been adapted to work in the conditions needed for XUV transmission in this range. This work has shown that a stable liquid sheet of a chlorinated solvent can be generated under roughing vacuum pressures. The next step is to be test these chlorinated solvent liquids sheets with the XUV absorption spectroscopy technique and move forward with studying molecular complexes in the solution-phase.

2.10 Acknowledgements

I would like to thank you the research team at LCLS including Daniel DePonte, Jake Koralek, and Bob Sublett for the assistance in learning to use the gas-accelerated liquid sheets. I would also like to thank Kristopher Benke for teaching me the fundamentals of solution-phase sample delivery in vacuum.

CHAPTER 3: XUV Transmission of Liquid Sheets Under Vacuum

3.1 Introduction

With the stabilization of the liquid sheet of a chlorinated solvent under roughing vacuum, the liquid sheet was tested in the XUV spectroscopy system. While the work in the previous chapter was conducted using a test vacuum chamber at roughing pressures, it is essential to be able to stably operate a liquid sheet in the conditions of the XUV system. It needs to be shown that XUV photons can be transmitted through a liquid sheet and show that XUV M-edge absorption through a liquid sheet sample is feasible. While XUV photons from a tabletop source in the energy range of between 220-450 eV and 284-538 eV have been transmitted through solution-phase sample, XUV photons have not been transmitted through solution-phase samples in the 40-80 eV energy range.[40,14] This lower energy range can measure the M-edge absorption of first row transition metals and will expand the field of studying molecular complexes in the solution phase with ultrafast XUV absorption spectroscopy.

3.2 Solution-Phase Excited State Dynamics of FeTPPCl

With the solution-phase sample delivery method for XUV spectroscopy, the XUV absorption of 5,10,15,20-tetraphenyl-21H23H-porphine iron(III) chloride (FeTPPCl) can be studied. This metalloporphyrin contains an Fe(III) center and can serve a model complex for heme-proteins. The iron monoporphyrin was chosen as the first complex to be studied to determine the solution-phase excited state dynamics because the excited state dynamics have been well documented in the solid state with transient XUV spectroscopy.[8] Before transient XUV absorption studies were performed, it was thought that upon excitation of the FeTPPCl, the iron center would relax through a metal centered excited state.[52] With transient XUV spectroscopy, the metal center of FeTPPCl was probed directly and it was found that the excited iron porphyrin did not decay through a metal-centered excited state, but rather through a vibrationally hot ground state.[8] Studying the excited state dynamics of the FeTPPCl in the solution-phase would better replicate the conditions of biological complexes or homogeneous catalysis systems.[53]

3.3 Stabilization of FeTPPCl in EDC Liquid Sheets Under Vacuum

Because the plasma cleaned microfluidic chip was found to produce stable liquid sheets of pure chloroform as shown in the previous chapter, these chips were used to generate liquid

sheets of FeTPPCl in dichloroethane (EDC). EDC was used as the solvent for the concentration solutions of FeTPPCl because it was found to form more stable liquid sheets than using chloroform. Figure 3.1 shows the reflective imaging view of the sheet on the left and the transmissive view of the nozzle on the right. The transmissive image on the right is perpendicular to the plane of the sheet (imaging pathway is detailed in Figure 2.7). The reflective image of the FeTPPCl in EDC shows a mass formed on the upper right side of the sheet. This mass can also be seen protruding from the nozzle, through the droplet in the right image. Despite producing a stable sheet for chloroform, the plasma cleaned chip, would not produce a stable film for a solution of FeTPPCl in EDC.

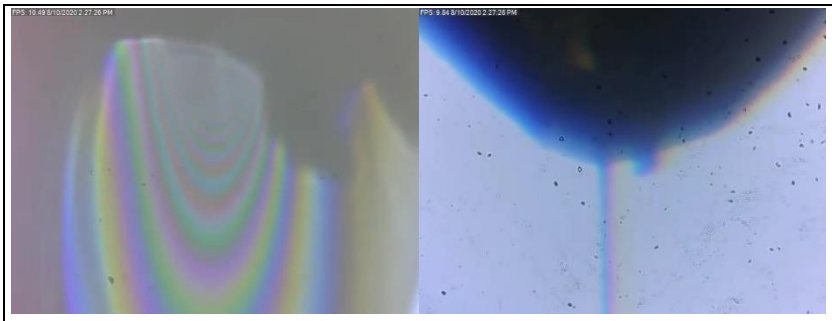

Figure 3.1: A liquid sheet of FeTPPCl in EDC under roughing vacuum generated with a plasma cleaned chip. A particulate or ice is formed on the nozzle of the chip which destabilized the liquid sheet.

While plasma cleaning the microfluidic chips removed the hydrophobic coating on the outer regions of the chip, some coating may have remained in the inner channels. The microfluidic chips were then custom ordered without any coating on the borosilicate chips. These uncoated chips were used to generate liquid sheets of an FeTPPCl in EDC. Figure 3.2 shows a stable FeTPPCl in EDC liquid sheet running under roughing vacuum. The left image for the reflective imaging of the liquid sheet with colored interference bands. The right image shows the side view of the microfluidic chip with the jet visible. The FeTPPCl in EDC sheet formed with this uncoated chip was found to be stable under roughing vacuum pressures for several hours. This method of liquid sheet generation was found to be acceptable for attempting to generate a liquid sheet of FeTPPCl in EDC in the XUV instrument and attempt M-edge absorption spectroscopy.

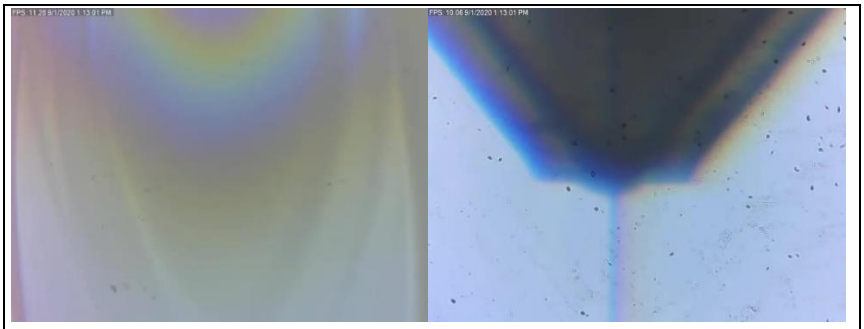

Figure 3.2: A stable liquid sheet of FeTPPCl in EDC under roughing vacuum generated with an uncoated chip.

3.4 Differential Pumping for Liquid Sheet in the XUV Chambers

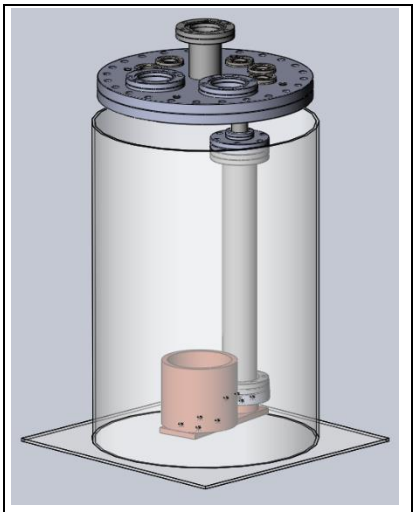

Figure 3.3: Stainless Steel enclosure for use in the XUV sample chamber to limit the vapors and gas load from increasing the pressures of the other chambers. The stainless-steel lid and cold trap are surrounded by the stainless-steel enclosure in the sample chamber.

Due to the short attenuation length of XUV light discussed previously, it is essential to operate XUV spectroscopy at high levels of vacuum to ensure enough photons are available for ground state and transient absorption experiments. When flowing a liquid sheet sample, both the solvent and the He gas needed to form the liquid sheet contribute to an increase in the vacuum chamber pressure. A differential pumping plan was designed to limit the flow of gas between the vacuum chambers to prevent an increase in pressure in the vacuum chambers adjoined to the sample chamber. Differential pumping involves inserting conductance barriers with a small orifice that limits the gas flow between sections of the vacuum chambers.[54] Figure 3.4 depicts the vacuum chambers of the XUV system and the gray barriers represent the conductance limiting barriers with an orifice diameter of 1 cm and the combined pumping speed from the turbomolecular pumps. The spectrometer chamber contains two barriers to ensure the charge-coupled detector (CCD) is operated at a pressure below 1x 10^{-6} Torr. The CCD needs to be cooled to -60 °C to limit the noise level. Figure 3.4 shows the pumping speed underneath an arrow that represents a turbomolecular or roughing pump speed. The CCD can be damaged by condensation of water if the chamber pressure increases. Figure 3.3 depicts the CAD drawing of the stainless-steel

enclosure designed to surround the chip flowing with liquid and the cold trap. This enclosure contains two small holes for the inlet and outlet of the XUV probe and pump paths. The enclosure is placed in the sample chamber and a roughing line is attached to one of the 2.75 in flanges to alleviate the pressure increases in the sample chamber.

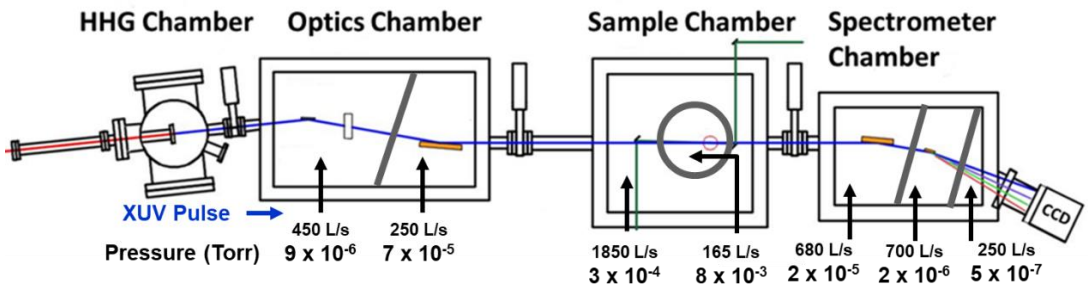

Figure 3.4: The vacuum chambers for the XUV absorption instrument. Estimates for the pressure in each chamber with the additional turbos and the barriers added.

3.5 Imaging Pathway for the XUV Sample Chamber

To image the liquid sheet in the sample vacuum chamber, a transmissive pathway was used. The reflective imaging pathway and 10X objective could not be used due to the space constraints of the sample chamber. The pathway used for the pump wavelength was used for the imaging pathway. A dichroic mirror (Thorlabs, DMLP567) which transmit light above 567 nm and reflects light below 567 nm was used to reflect the 400 nm pump and transmit the light from an LED flashlight. Because the imaging light contained only wavelengths above 567 nm, the liquid sheet image contains a yellow or orange hue, seen in Figure 3.6. The transmitted light is sent into the sample chamber through a port and focused down near the sample position where the chip holder is mounted using a f = 50 lens. Downstream from the chip holder, a plano-convex f = 12.5 cm lens collimates the transmitted light which is sent out of the sample chamber to a webcam which captures the transmitted image.[7] The imaging pathway was aligned to the sample position so that the liquid sheet can be monitored during data collection.

3.6 Mounting the Chip Holder in the Sample Chamber

All the necessary components for liquid sheet generation need to be added to the XUV sample chamber to operate the liquid sheet. Because the flange size of the XYZ manipulator was 2.75 in and there was no side flange access to the sample chamber, the chip holder needed to be assembled before being mounted into the vacuum chamber. Also, because of the size restriction, the chip holder and sample cell holder needed to fit into the opening with a bore diameter of 1.375 in. The chip holder with an attached sample cell for holding solid-state reference sample, is shown in the Supplementary Figure 5.2. The stainless-steel enclosure was put inside the sample chamber and aligned so that the pump path, XUV path, and imaging path could pass through the holes. The stainless-steel lid with the attached cold trap needed to be lifted and put into the sample chamber so that the cold trap did not block the beam and fit into the center of the stainless-steel enclosure. The holder with the chip and the attached gas and liquid lines were mounted to a 24 inch long, ½ in diameter optics post, depicted in Figure 3.5. Because the liquid and gas lines needed to be attached to the flange with the fluidic connections, the liquid and gas lines attached to the holder were fed through the central flange opening and subsequently attached to the flange with the fluidic connection. The chip holder on the long optical post was then fed through the central flange opening and placed on the bottom of the chamber with the optical post protruding out of the central flange. The XYZ manipulator was then placed on top of the central flange of the lid. The optics post with the holder was then mounted to a flange that was then attached to the top flange of the XYZ manipulator.

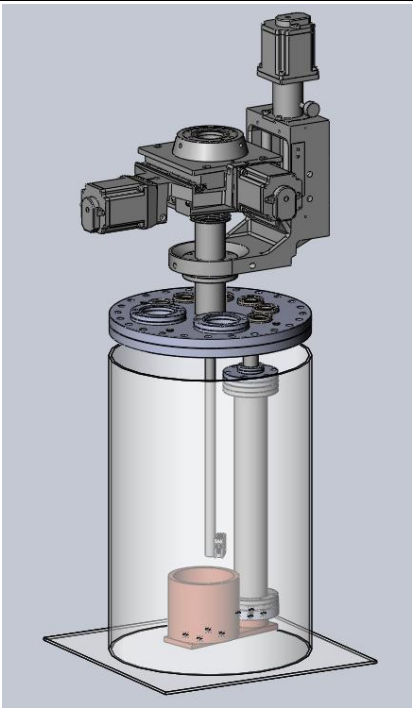

Figure 3.5: The chip holder on a long optics from the XYZ manipulator into the stainless-steel enclosure.

3.7 Stabilizing the Chip Holder in the Sample Chamber

When the chip holder was initially mounted to the flange on the XYZ manipulator, shown in Figure 3.5, it was found that under vacuum that holder would vibrate horizontally. This vibration moved the chip approximately 100 μm on either side, this vibration interfered with the

formation of a uniform thickness to be measure from the running EDC liquid sheet. The holder was likely moving from the vibrations from several vacuum pumps necessary to perform XUV spectroscopy and was susceptible to the vibration due to being suspended from a long post. The longer post needed in the XUV sample chamber as opposed to the test chamber explains why this vibration problem was not encountered in the test chamber. To stabilize the vibration, a thicker 1-inch diameter optics post was used as the last 0.5 inch of the long ½ diameter optics post to mount the chip to the top flange of the XYZ manipulator. A fluorocarbon gasket (Kurt J. Lesker, GA-0275V), as opposed to a copper gasket was used to assemble the top flange. The fluorocarbon gasket allowed for the flange to be tighten more and it was thought that the compressible fluorocarbon could absorb some of the vibrations. It was found that both the wider optics post base and the fluorocarbon gasket stopped the vibrations and stabilized the optics post.

3.8 Start-Up Process for Running the Liquid Sheet Under Vacuum in the Sample Chamber

To start the process of running a liquid sheet of EDC under vacuum in the sample chamber, the following steps were taken to ensure the stability of the liquid flow and prevent damage to the microfluidic chip. The sample chamber was filled with nitrogen gas and the cold trap was cooled to roughly -23 °C with liquid nitrogen. The nitrogen flow can be stopped once the cold trap has been cooled. The EDC liquid flow and He gas flow can then be started and tuned to form a liquid sheet. Once a stable liquid sheet is formed at atmosphere, the sample chamber can be closed and the chamber can slowly, over the course of 10 to 20 minutes, be opened to the roughing pump to evacuate the gas from the sample chamber. As the pressure in the chamber decreases, the sheet will become thinner and both a higher flow rate of EDC and higher pressure of He will be needed to maintain the desired sheet thickness. Due to the compressible bellow attaching the top and bottom flange of the XYZ manipulator, the mounted chip holder will be compressed downward, and the vertical position of the chip will need to be moved back to the sample position. Once the vacuum chamber is at an acceptable roughing pressure near 1×10^{-1} Torr, the turbos on the chamber can be turned on and bring the vacuum chamber to high vacuum. For these liquid sheet experiments, with the liquid sheet operating with liquid and gas flow and the turbomolecular pump at full speed, the pressure in the sample chamber was roughly 8.0×10^{-3} Torr. This pressure can be lowered in the future by performing more extensive leak testing on the vacuum chamber, cold trap, and connections made to the stainless-steel lid. The pressure in the sample chamber was at an acceptable level to open the

sample chamber to the adjoining vacuum chambers. With the gate valves separating the four-vacuum chamber, depicted in Figure 3.4, the pressure in the detector chamber with the CCD was 2.0×10^{-5} Torr. While the liquid sheet was running during data collection, the CCD was not cooled as a precaution for the prevent any damage to the device. In future experiments when the suspected leaks in the liquid sheet apparatus are patched and the pressure in the detector chamber is lowered, the CCD will be cooled to lower the noise of detection.

3.9 XUV Transmission Through an EDC Liquid Sheet

The above procedure was used to start-up the liquid sheet in the XUV sample chamber, and a stable EDC liquid sheet was generated and characterized. Figure 3.6 shows a transmissive image of EDC sheet running in the sample chamber with XUV flux transmitting through the liquid sheet. This *in situ* imaging allowed for the liquid sheet to be monitored during all the XUV absorption experiments conducted. The liquid sheet in Figure 3.6 is of the sheet with a flow rate of 0.22 mL/min of EDC and with He with a backing pressure of 60 psi that was adjusted with a needle valve. The true value of the He gas pressure was unknown and a flow meter would be needed to measure the gas flow after the needle value and into the vacuum chamber. The EDC liquid sheet in Figure 3.6 is approximately 330 µm in width at the widest section and 660 µm in length at the longest section. The thickness of the sheet cannot be determined from the image due to the lack of interference bands and was later determined using XUV absorption.

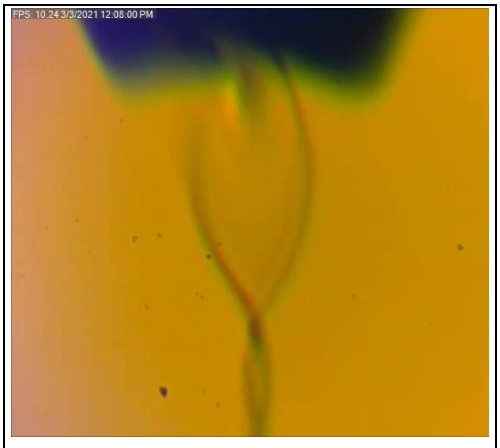

Figure 3.6: Stable EDC sheet under vacuum in sample chamber with XUV transmitting through the sheet.

While the EDC liquid sheet was running in the sample chamber, the XUV photons were transmitted through the center of the sheet and the total counts per shot were recorded on the CCD. The total counts were monitored over a 45-minute period while the conditions of the liquid sheet flow rate and gas pressure were not changed. The left plot of Figure 3.7 shows the variation in the total number of XUV counts record on the CCD through the XUV sheet during a 45-minute period. The fluctuations of the XUV could be caused from a change in the XUV generated during the HHG process or a change in the thickness of the EDC liquid sheet. It has been found that the XUV photons and

subsequent spectra generated greatly depend on the conditions of HHG generation.[31] The XUV instrument has been found to be sensitive to the temperature and humidity of the room. The left plot of Figure 3.7 below shows how the total XUV counts fluctuate over a roughly 8.5-minute period. The right plot of Figure 3.7 shows that the temperature of the laboratory containing the XUV instrument during the time that the XUV counts was monitored through the EDC liquid sheet. The temperature of the room also appears to fluctuate over an 8.5-minute period. Therefore, part of the fluctuations of the XUV counts over the 45-minute period through the liquid sheet may be due to fluctuation in the room temperature and the effect on the HHG conditions. The total flux was measured on the uncooled CCD through vacuum, and it was found that the percent change from the mean of the counts was ±2% (shown in Supplementary Figure 5.1). This value represents the change in flux that occurs due to the change in the room conditions.[31] The percent change from the mean of the XUV counts through the EDC sheet was found to be ±6%. It appears that while the fluctuations in the XUV counts from the HHG generation condition may account for part of the change in the XUV counts through the EDC sheet, a change in the thickness of the XUV sheet likely accounts for a greater percentage of the change from the mean. Thickness of the sheet was calculated over this time, not accounting for the XUV fluctuations due to the HHG process, and the thickness of the EDC sheet over the spot size the XUV beam probes varies from 310 nm to 370 nm with an average thickness of 340 nm.

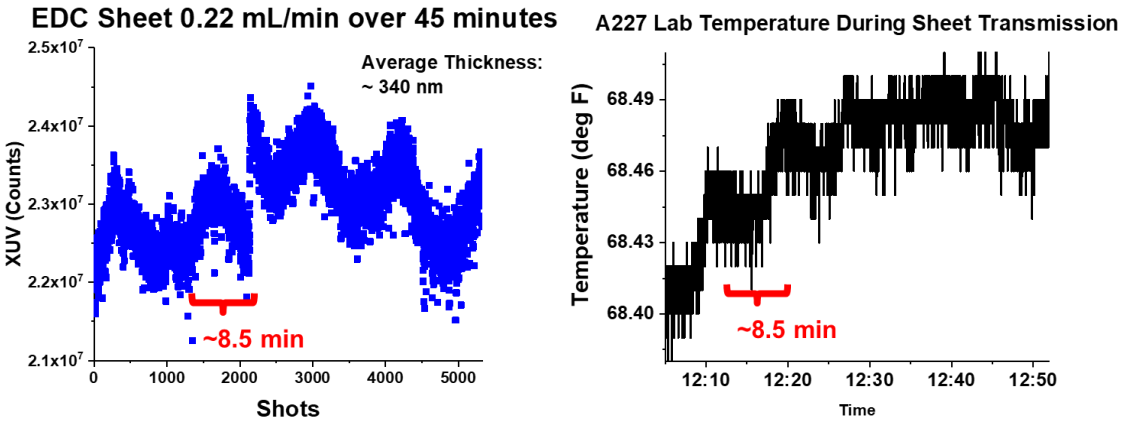

Figure 3.7: Percent change of the XUV is about ±6% change. This is greater than the ±2% change of the mean flux for the uncooled CCD.

The EDC liquid sheet was raster scanned to measure the XUV counts with each position. The purpose of this measure is to see how the thickness changes along the plane of the sheet and determine the area of the sheet with the most uniform thickness. A uniform thickness has been found to prevent harmonic artifacts from affecting XUV absorption spectra. Figure 3.8 shows the sample map of the EDC liquid sheet operating at 0.22 mL/min. The sample map was taken with 80 µm step sizes in the horizontal direction and 175 µm in the vertical direction. The thickness of each step is calculated from the XUV absorption at each point. The process of collecting all of the sample step required roughly two hours in total. Over this time the thickness of the liquid sheet may have varied, evidenced by the 60 nm range of thickness calculated over the 45-minute period discussed above.

The pattern of the thickness variation is similar to the thickness variation observed in the interference bands of the liquid sheet in Figure 2.14 from the previous chapter. The thickness varies over the plane of the sheet with the largest change in thickness near the top of the liquid sheet. Center of the liquid sheet has a thickness of roughly 290 nm. The thickest portion of the liquid sheet is at the top of the sheet in the center with a thickness of 730 nm. The thinnest portion of the liquid sheet is 150 nm thick near the bottom of the sheet. Based on the sample map and the raster size steps, the width of the liquid sheet at the widest point is approximately 240 µm and the length at the longest point is approximately 700 µm. The section with the most uniform thickness appears to be at the vertical center of the liquid sheet with the center thickness of 290 nm at 240 µm horizontal (H) step, 215 nm at 320 µm H step, and 190 nm at 160 µm H step. Collecting a sample map of the varying thickness of the liquid sheet can be used to select the section with the most uniform thickness for an XUV absorption spectra. The XUV transmission spectra of the EDC sheet was collected and is shown in Figure 3.9 a). This is the first XUV transmission spectrum of a chlorinated solvent in the energy range of 40 eV to 80 eV. The transmission spectrum contains

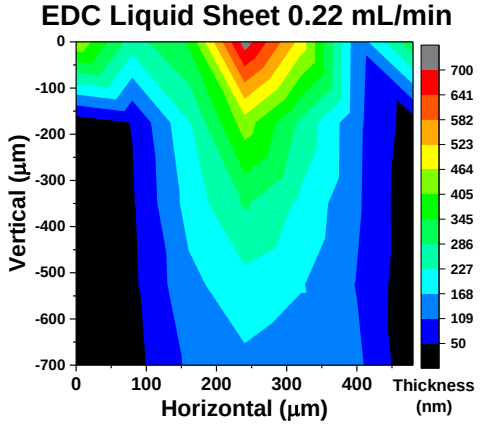

Figure 3.8: A sample map of the EDC liquid sheet flowing at 0.22 mL/min. The horizontal step size is 80 µm and the vertical step size is 175 µm.

the harmonic structure, like in the spectrum of the XUV source in Figure 1.3. An XUV absorbance spectra was also collected with vacuum used as the reference. The absorbance spectrum in Figure 3.9 b) contains significant harmonic structure in the baseline of the spectrum. This prevalent harmonic structure may indicate that the spot measured on the liquid sheet does not have enough of a uniform thickness to prevent harmonic structure in the absorption spectrum.[31] The increased noise in the spectra may also be effected by the unstable operation of the liquid sheet. For a sheet jet operated for L-edge experiments, it was found that the noise level of the experiment increased when the sheet jet was less stable.[38]

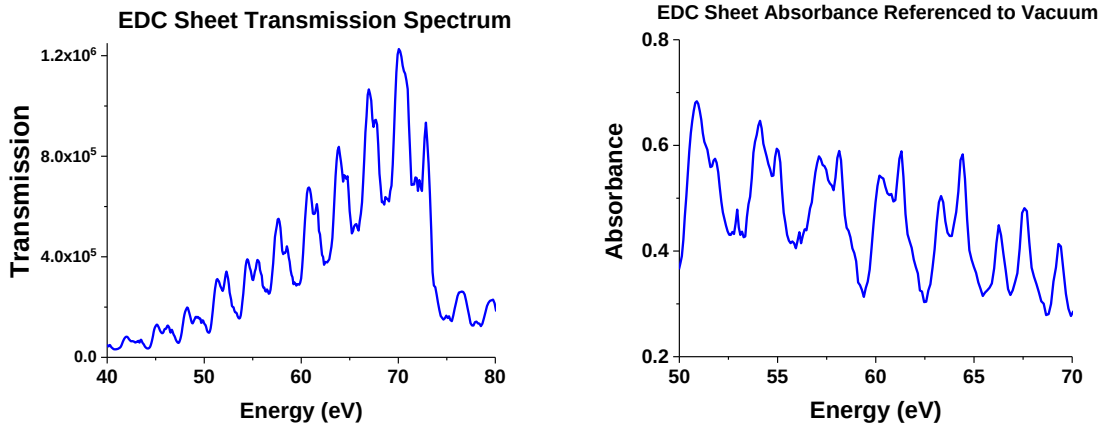

Figure 3.9: a) The XUV transmission spectrum of an EDC liquid sheet. B) The absorption XUV transmission spectrum of an EDC liquid sheet. The thickness of the EDC sheet at the probed position is 250 nm.

3.10 Prediction of Noise Effect on Transient XUV Spectra

Although the harmonic structure of the ground state absorption spectra has a major contribution to the spectrum of EDC, a difference spectrum with transient XUV data collection is less susceptible to the noise generated from a varied thickness sample spot. A pump beam which is larger than the probe beam can be used to produce a uniform excited-state spatial distribution and reduce misalignment between the pump and probe beams. It was found that for this XUV instrument, that a minimum of doubling the pump beam size relative to the probe size to reduce the harmonic structure in the transient spectra.[31] A calculation was done to determine if a transient signal from an FeTPPCl liquid sheet could be observed over the noise of the liquid sheet and the condition of the XUV instrument. The transmission spectra collected through the EDC liquid sheet over the 45-minute period were used to simulate the pump-on and pump-off

spectra. These transmission spectra represent the noise that would be excited from the liquid sheet and from the XUV instrument. Using a ground state and excited state spectrum of the FeTPPCl at the simulated concentration in the liquid sheet sample, the averaged difference spectra of an FeTPPCl excited at 400 nm was simulated at various excitation fractions. Figure 3.10 shows the estimated transient absorption signal from a simulated stable liquid sheet of FeTPPCl with a concentration of 14 mM. The figure shows that positive feature at 55 eV signal is greater than the noise for all the excitation fractions used. For the bleach feature at 57.4 eV, the signal to noise ratio is high with a 20% excitation, but the ratio improves as the excitation fraction is increased to 30 % and 40%. From this figure, a 20% excitation fraction can used to see the features of the transient signal, with a high excitation fraction improving the signal to noise ratio. This simulation supports the idea that a transient signal from a concentrated solution of FeTTPCl in an EDC liquid sheet could likely be observed over the noise of the sheet and the instrument.

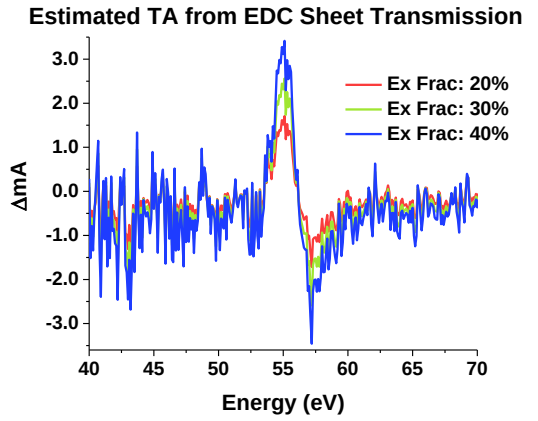

Figure 3.10: With large excitation fraction and several averages (for sheet noise), tXUV of a stable FeTPPCl seems feasible.

3.11 Ground State Attempt of an FeTPPCl Liquid Sheet

A ground state XUV absorption spectra of a 10 mM FeTPPCl in EDC liquid sheet referenced to a pure EDC sheet was attempted. The process of switching solutions used for liquid sheet generation for a reference and sample to collect a ground state absorption spectrum is described in the previous chapter. The Figure 3.11 shows the ground state spectra obtained from averaging scans of the transmission of the FeTPPCl sheet and referencing averages of scans from the transmission through pure EDC. The absorbance value of the plot is less than 100 mA, suggesting that the thickness of the reference EDC sheet is only slightly thinner than the thickness of the FeTPPCl in EDC sheet. It has been found that the having the thickness of a reference like the thickness of a sample improves the ground state absorption spectra and reduces harmonic artifacts.[55] This similar thickness also indicates that the backing pressure of the reference syringe pump and sample syringe pump were similar and switching the pumps did not greatly impact the thickness of the sheet. In the spectrum, however,

there are large harmonic artifacts present and the iron signal from the FeTPPCl is not visible. This signal may have been improved with an increased number and scans and averages. However, the liquid sheet of the FeTPPCl became unstable and prevent further collection of ground state XUV absorption spectra.

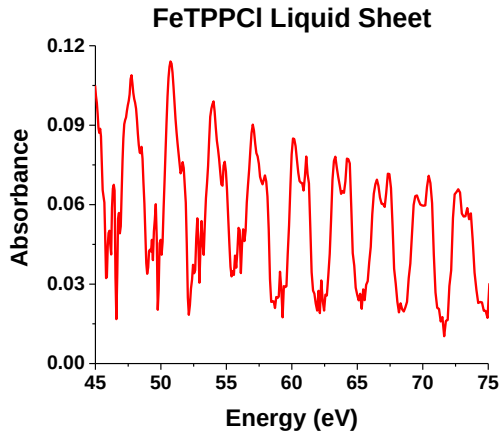

Figure 3.11: The XUV absorption spectrum of an FeTPPCl in EDC liquid sheet. The signal to noise obscures the absorbance signal from the iron center of the iron porphyrin.

It was found that the FeTPPCl liquid sheet became unstable about 30 minutes after the sheet was generated. While collecting the transmission through the FeTPPCl in EDC liquid sheet, it was found the large particulates visible in the live video of the liquid sheet were interfering with the XUV transmission. Figure 3.12 a) shows the FeTPPCl in EDC liquid sheet running in the XUV sample chamber at roughly 8.0×10^{-3} Torr. The nozzle of the chip is at the top of the image and there are large black pieces protruding from the nozzle. It was found that these pieces formed and would interfere with the liquid sheet or block the XUV transmission. These pieces would form rapidly and consistently and would come from the nozzle of the chip. At the bottom of Figure 3.12 a), a black mass is visible at the bottom of the image. This mass is an icicle that is forming from the copper cold trap. This icicle also interfered with the liquid sheet and blocked the XUV transmission. The temperature of the copper cold trap was adjusted and the icicle was removed, however, the pieces from the nozzle continued to form and interfere with the collection of a FeTPPCl in EDC liquid sheet ground state. When switching from generation an FeTPPCl sheet to a pure EDC sheet, the pure EDC sheet became unstable and the pieces were formed from the nozzle as well. Figure 3.12 b) shows a pure EDC liquid sheet running in the sample chamber with the pieces protruding from the nozzle. Due to the instability of the FeTPPCl in EDC liquid sheet, a ground state spectrum of FeTPPCl with an iron signal was not obtained. This instability also prevented the collection of transient XUV absorption of the FeTPPCl in an EDC sheet.

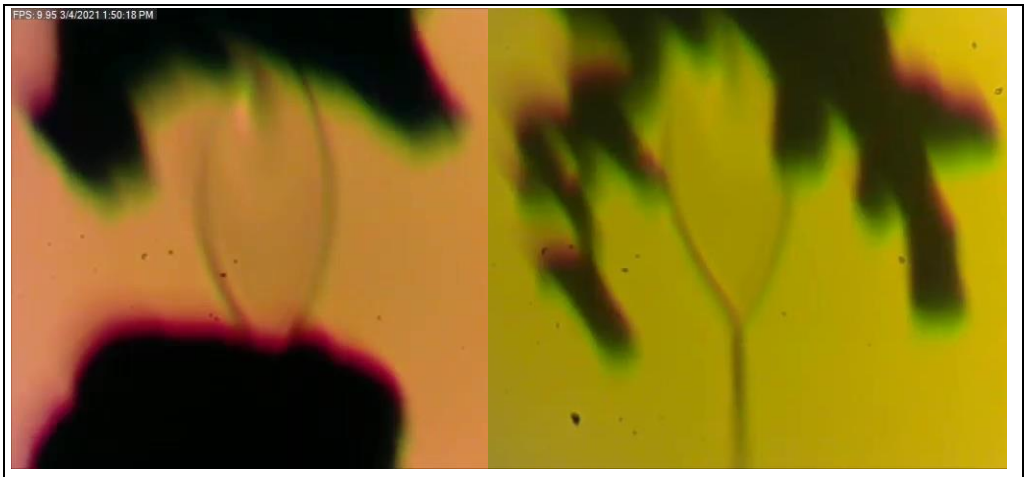

Figure 3.12: a) A liquid sheet of FeTPPCl in EDC. In a bottom of the image, the black spot is an icicle that is coming upward from the cold trap. The back spot protruding from either side of the sheet are particulate masses or icicle formations. B) A liquid sheet of EDC after running a liquid sheet of FeTPPCl in EDC.

3.12 Future Directions

Further experimental with solution-phase XUV spectroscopy requires determining the cause of the formation of these masses on the nozzle of the chip. Upon removal of the used chip holder from the sample chamber, the chip and part of the surrounding area was coated in a layer of solid porphyrin material. The concentration of the FeTPPCl solution in EDC may have been too concentrated and the porphyrin precipitated out the solution upon contact with the high vacuum environment and caused the buildup of the masses from the nozzle. For a sheet jet operated for L-edge experiments, it was found that solutions with higher concentrations resulted in a less stable sheet and increased the noise relative to the less concentrated solutions.[38] The concentration of the FeTPPCl was lowered to 10 mM, however, the liquid sheet formed was unstable and exhibited the same masses forming from the nozzle. The particulate masses may also be formed due to a buildup of static charge at the nozzle of the chip. Static electricity can be generated and when a liquid is passes at a high flow rate through plastic tubing.[56] The discharge of static charge may be causing the porphyrin to precipitate out of the solution. Alternatively, the masses formed may be icicles formed from nucleation centers of porphyrin material on the nozzle of the chip. The lower pressure of the XUV sample chamber compared to the test chamber may result in lower temperature and cause the solution to freeze at the chip nozzle. This

may explain why the particulate formation was not seen in the test chamber which was operated at roughing vacuum as opposed to the higher vacuum of the sample chamber.

To remedy the possibility of static charge build up contributing to the particulate formation, the chip and holder will be grounded. To prevent the potential formation of icicles from the chip nozzle, a small cartridge heater will be used to warm the chip. The concentration of the FeTPPCl can also be adjusted to find a concentration at which the particulates to do form on the nozzle. However, lowering the concentration of the porphyrin solution will decrease the signal for XUV absorption. A turbomolecular pump will be added to the test chamber to lower the pressure of the chamber to replicate the conditions more accurately the XUV chamber. These methods will be examined in test chamber at lower pressures to ensure a stable liquid sheet of FeTPPCl can be formed and remain stable for the several hours needed for ground state and transient XUV absorption measurements.

3.13 Conclusion

The conditions necessary for obtaining a stable liquid sheet of FeTPPCl in EDC under roughing vacuum pressures were determined. A method was determined for properly mounting a holder of the microfluidic chip to prevent vibrations and starting up the liquid flow for the sheet under vacuum conditions. The first transmission of XUV in the energy of 40 eV to 90 eV was collected through a flowing liquid sheet of EDC. A sample map of the liquid sheet determined the thickness variation of the flowing sheet. It was determined that with the noise level present in the liquid sheet, a transient spectrum of a liquid sheet containing FeTPPCl could be collected with a reasonable signal to noise ratio. However, it was found that the liquid sheet of FeTPPCl was unstable in the XUV sample chamber under high vacuum conditions. It has been postulated how these instabilities can be remedied, however, more work is needed to stabilize an FeTPPCl and allow for XUV absorption studies. Overall, this works shows the first major step of extended into field of M-edge XUV absorption spectroscopy the solution-phase.

3.14 Acknowledgements

I would like to thank Ryan Ash for help me set up the roughing lines for the XUV instrument. I would like to thank Hannah Toru for making the control boxes for several turbo pumps used for the differential pumping system. I would also like to thank Kristopher Benke,

Aastha Sharma, and Yusef Shari'ati for assisting during experiments collecting the XUV transmission through the liquid sheet.

CHAPTER 4: Photophysics of µ-Oxo-Bridged Iron(III) Porphyrins

4.1 Introduction

Iron porphyrins are of great interest to the field of catalysis because the structure mimics the active site of heme proteins.[57,58] Some proteins are known to perform oxygen atom transfer reactions with an Fe(IV)oxo intermediate state.[59] A stacked iron porphyrin $(TPPFe)_2O$, µ-oxo-bis((tetraphenylporphinato)iron(III)), was first synthesized in the 1960s and has been studied as a potential active site mimic.[60] This stacked porphyrin contains antiferromagnetically coupled Fe(III) porphyrins with a µ -oxo bridge between the iron centers separated by a distance of about 5.2 Å. Resonance Raman and X-ray crystallography studies have shown that the iron centers in the stacked porphyrin have a structure similar to the high-spin iron in the monoporphyrin Fe(III)TPPCl.[61,62,60,63] These stacked porphyrins have been shown to perform oxidation catalysis,[64] and are candidates for a type of energy storage that does not rely on a long-lived charge transfer state used with semiconductors.[65] These compounds are thought to undergo photodisproportionation, which means that upon photoexcitation one product will either be a stronger reductant or oxidant and can perform a useful redox reaction at a rate that is competitive with the back reaction.[65] This could be used to store photon energy in the form of a redox reaction with the photoproduct.

Stacked porphyrins can catalyze the oxygenation of a substrate upon irradiation with visible light. It was found the iron stacked porphyrin can oxidize dimethyl sulfide (DMS) and produced a stoichiometric amount of dimethyl sulfoxide (DMSO).[66] This established a two-electron photoreduction of the stacked porphyrin with the oxygenation of the DMS substrate. The oxygen atom transfer occurred at ambient temperature and pressure and an external co-reductant was not required to complete the oxidation.[66] A iron stacked porphyrin with a dibenzofuran spacer was found to catalyze the oxidation of several olefins with molecular oxygen.[64] This study showed that the modified iron stacked porphyrin was capable of performing challenging olefin oxidations.[64]

For stacked porphyrins, it is thought that upon photoexcitation one of the Fe-O bonds of the µ-oxo bridge undergoes a homolytic cleavage and a separated TPPFe(IV)O and an TPPFe(II) are formed[58], depicted in Figure 4.1. The TPPFe(IV)O is the stronger oxidant and can perform oxidation reactions. The original catalyst is then reformed after the two remaining TPPFe(II)

subunits react with O_2. To aid in the reformation of the initial catalyst, cofacial bisporphyrins were synthesized with a molecular spacer between the Fe(III) porphyrins subunits to limit the structural reorganization required for the Fe(II)TPP subunits to reform the μ-oxo bridge.[67] These cofacial bisporphyrins were further modified with a variety of molecular spacers to create a "Pacman effect".[64] The Pacman effect occurs when the bisporphyrin is clamped down in the native state with a short iron-iron distance, but when the bisporphyrin is photoexcited, one of the iron-oxygen bonds is cleaved and the iron centers separates. The effect is successful when the iron-iron distance increases, allowing for a larger space where a side-on oxidation of a substrate by the Fe(IV) can occur. The bisporphyrin then reforms the clamped structure with the oxygen present. A variety of "Pacman" bisporphyrin have been shown to perform the multielectron oxidation of the olefins with molecular oxygen and without the need for an external reductant.[64] While catalysis can be performed, the efficiency of this complex as a catalyst is low.

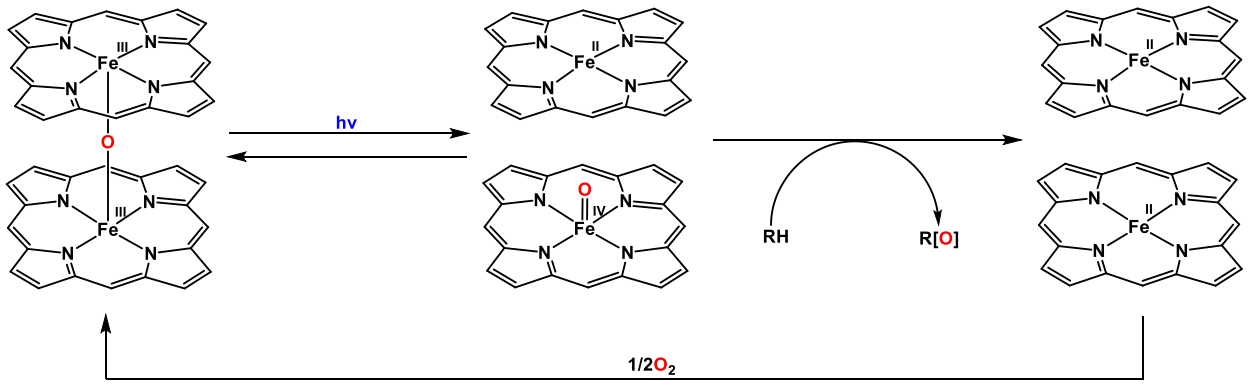

Figure 4.1: The proposed catalytic pathway for the iron stacked porphyrin. The Fe(IV)oxo intermediate oxidizes the substrate (R) with molecular oxygen (figure made in ChemDraw by Clare Leahy).

It has been found that the quantum yield of photodisproportionation and formation of the Fe(IV)oxo intermediate in the absence of substrate is low (~1 x 10^{-4}).[58] The quantum yield of photodisproportionation varies depending on the wavelength of light used with the highest measured value at 350 nm, and decreasing to the lowest measured value at 441 nm.[58] The stacked porphyrin is not photoactive at wavelengths greater than 500 nm.[58] This has led to speculation about the excited state manifold of this complex which is thought to be correlated to the wavelength dependence of the quantum yield. It has been proposed that these complexes are reacting from a highly distorted charge-transfer state due to the change of the bond order of the

bridging M-O-M system.[58] If the excited state leads to disproportionation, the success of the homolytic cleavage leading to the formation of the Fe(II)TPP and Fe(IV)TPPO could be wavelength dependent. The ability of escaping the initial solvent cage would depend on the amount of vibronic energy that is converted into separating the subunits is the formation of subunits is wavelength dependent.[58] This highly distorted charge transfer state can be thought of as a metal-to-metal charge transfer state. More work needs to be done to elucidate the excited state manifold of this complex.

4.1.1 Past Transient Optical Studies

Transient optical absorption studies have been performed to try to map the excited state manifold and identify the intermediate states formed upon irradiation of μ-oxo iron bisporphyrins. One goal has been to clearly identify an excited state containing the Fe(IV)oxo. Raman studies identified a stretch corresponding to the Fe(IV)=O at 852 cm^{-1} for the monoporphyrin[68,69,70]. Also, optical absorption of a Fe(IV)=O species was observed after the decomposition of an $(TPPFe)_2O$ at -80 °C.[71] Picosecond absorption studies were performed in the 1988 study by Guest *et al.* to determine the identity of the intermediate state in the photoexcitation of $(TPPFe)_2O$.[61] In this study, the stacked porphyrin was excited with a 25 ps pulse at 532 and 355 nm, though no difference in the kinetics were observed based on the wavelengths. As shown in Figure 4.2, two possible pathways have been postulated after photoexcitation. In the first pathway (labeled Pathway A), the stacked porphyrin disproportionates in an TPPFe(II) and a TPPFe(IV)O. This state will be referred to the Disproportionated state. The TPPFe(IV)O can then oxidize a substrate with molecular oxygen. In the second pathway (labeled Pathway B), the stacked porphyrin splits into Fe(III)TPP+, where the cation is localized on the porphyrin ring, and Fe(III)TPPO-, where the anion is localized on the porphyrin ring. This state will be referred to as the Anion/Cation state. Notably, the oxidation state of the metal centers in this state is unchanged from the parent molecule. Oxidation of the substrate will only occur if the iron stacked porphyrin follows Pathway A upon photoexcitation.

In past transient optical absorption studies, the excited state spectra observed were compared to the ground state electronic spectra of Fe(II), Fe(III), and Fe(IV) porphyrin model complexes, to try to identify the oxidation state of the excited state.[61] Upon comparison, the identity of the excited state was unclear due to the similarities of the absorption spectra of the

iron porphyrin model complexes. It was postulated that upon photoexcitation a combination of the Anion/Cation state and Disproportionated state were formed with the Anion/Cation state as likely over 80% of the photoproduct.[61]

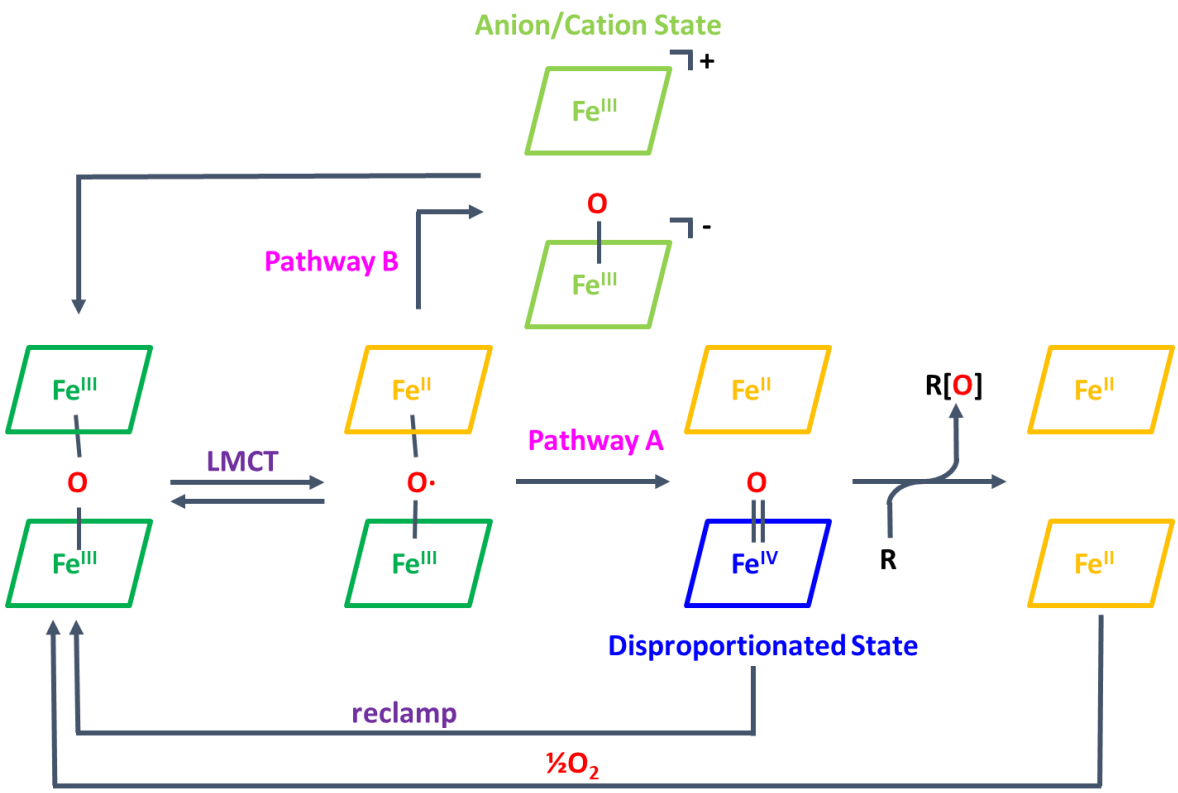

Figure 4.2: The proposed pathways of the iron stacked porphyrin upon photoexcitation (figure by Clare Leahy).

A 2003 study by the Nocera group performed picosecond optical transient absorption of similar μ-oxo iron Pacman porphyrins.[72] In this study, they identify a band at 360 nm as the ligand-to-metal charge-transfer (LMCT) band. It suggested that when using 405-nm pulses in this study, this excites the LMCT band and not the Soret band at 395 nm. For the transient experiments, Pacman iron porphyrins with a variety of structures and a simple stacked iron porphyrin were studied. Based on the transient results, the nature of the transient species was claimed to be the product of an LMCT excitation and that the Disproportionated state is prevalent as opposed to the Anion/Cation state. This conclusion is made based on comparing the excited state spectrum to the features observed in an Fe(IV) containing absorption spectrum. However, the comparison of the spectral features of the difference spectra to the Fe(IV) spectra

is not detailed. This conclusion is also based on the observation that the stacked porphyrin can catalyze oxidation reactions. However, the low quantum yield of oxidation reactions observed for stacked porphyrins may be explained by a small population of the Disproportionated state formed after photoexcitation. This study does not consider that the Anion/Cation state could account for a large percentage of the photoproduct and may be the state observed in the transient spectra. While this study suggests that the Disproportionated state forms upon excitation with 409 nm, little evidence is provided to disprove that the Anion/Cation state was formed.

4.1.2 Stacked Porphyrin Optical Absorption Features

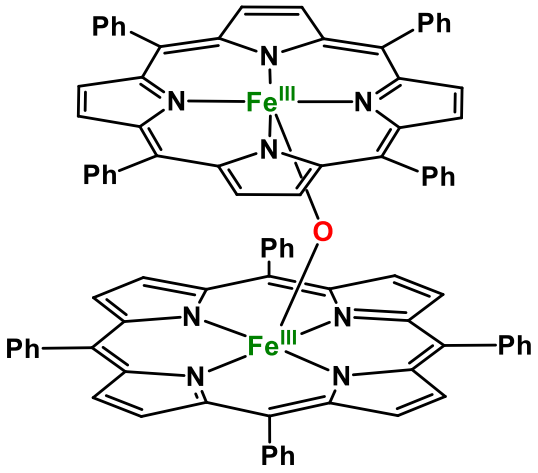

Figure 4.3 : Stacked porphyrin $(TPPFe)_2O$ with bridging oxygen, does not contain a bridging ligand. Figure created in ChemDraw by Clare Leahy.

The µ-oxo-bis((tetraphenylporphinato)iron(III)) was synthesized by the Vura-Weis group member Clare Leahy and is depicted in Figure 4.3.[73,60] Due to the wavelength dependence of the quantum yield of photodisproportionation, it is important to understand the absorption bands of the stacked porphyrin that are being excited with these transient absorption studies. The quantum yield of photodisproportionation has also been shown to be wavelength dependent for the complex $(FeTPPC)_2O$. It was found for that system, that the quantum yield increases when the excitation energy is increased from $ø = 5.2 \times 10^{-5}$ at 442 nm to $ø = 4.3 \times 10^{-3}$ at 334 nm. The quantum yield plateaus at the highest level at 334 nm and beyond to 290 nm.[74] It was speculated that the absorption band at 318 nm may be oxo-iron the charge-transfer excited state. When observing the optical absorption spectrum of the stacked porphyrin there are several absorption features, shown in Figure 4.4. There is a large peak around 410 nm, a small peak near 320 nm, and two small peaks near 575 nm and 610 nm. Martin Goutermann established the four-orbital model to explain the absorption spectra of free-base and metal porphyrins.[75] It was proposed that the absorption bands of the porphyrins are from the two HOMOs and LUMOs. The mixing of these states gives rise to a state with higher energy, the Soret band, and states with lower energy, the Q-bands.[75] The 410 nm peak corresponds to a porphyrin-based π to π* transition, the Soret Band, as seen in mono-porphyrins.[76] The weak peaks past 500 nm

correspond to the Q bands of the porphyrin. The small peak near 320 nm is similar to the halide-to-metal charge-transfer of the Fe(III)TPPCl[77] and is thought to be the oxygen-to-metal charge-transfer state of the stacked porphyrin.[72] A fault of the previous transient absorption studies may have been that the excitation energy used is not successful in breaking the Fe-O bond and initiating the disproportionation. Both transient studies may have been exciting porphyrin-based transitions that did not cleave the Fe-O bond and observed excited state absorption spectra unrelated to the formation of an Fe(IV). Transient absorption studies with an excitation wavelength of 355 nm or below with sub-picosecond time resolution may be needed in order to study the excited state dynamics associated with the formation of an TPPFe(IV)O intermediate.

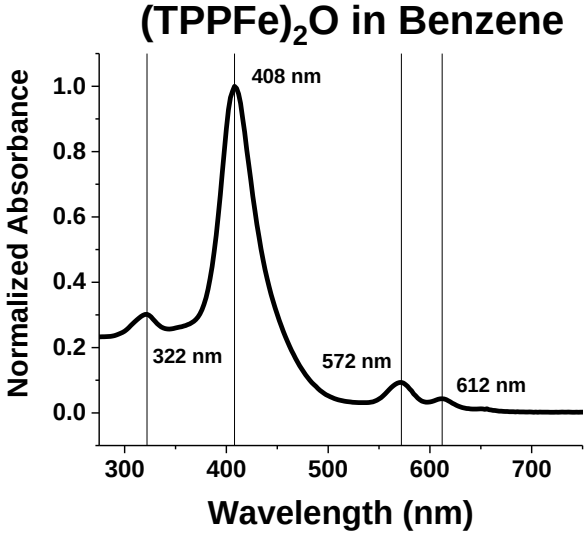

Figure 4.4: Visible absorption spectrum of the stacked porphyrin in benzene, normalized to the peak at 408 nm.

4.1.3 Transient Spectroscopy to Probe Iron Oxidation States

Performing OTA studies of the stacked porphyrin upon photoexcitation can provide insight into the excited state features of the ligand environment of the stacked porphyrin. Directly probing the iron centers of the stacked porphyrin systems upon excitation can elucidate the oxidation state of the iron centers at each step. The use of tabletop femtosecond M-edge spectroscopy use been previously used to elucidate the excited state dynamics of an iron monoporphyrin. By directly examining the excited states of the metal center of FeTPPCl, it was determined that the relaxation pathway upon excitation of the Soret band did not decay through a metal centered excited state.[8] That study provided insight from the metal center that was unavailable with previous studies that examined the excited state dynamics that used transient optical absorption spectrum that only provided spectral information about the ligand environment.[52,78]

It has been shown that the Fe(IV)oxo intermediate of an irradiated iron stacked porphyrin is the catalytically active state for oxidation reactions.[64] Ultrafast XUV spectroscopy and OTA

spectroscopy can determine if there is a difference in the excited state dynamics when the stacked porphyrin is excited into the Soret band at 400 nm or near the LMCT band at 350 nm. With this information, there may be ways to synthetically alter the stacked porphyrin to promote the formation of the desired Fe(IV)oxo state, either through stabilizing that intermediate or changing the time scale of the dynamics and prevent the reformation of the ground state.

4.2 Methods

4.2.1 Generation of 350 nm and 325 nm Pump Wavelengths

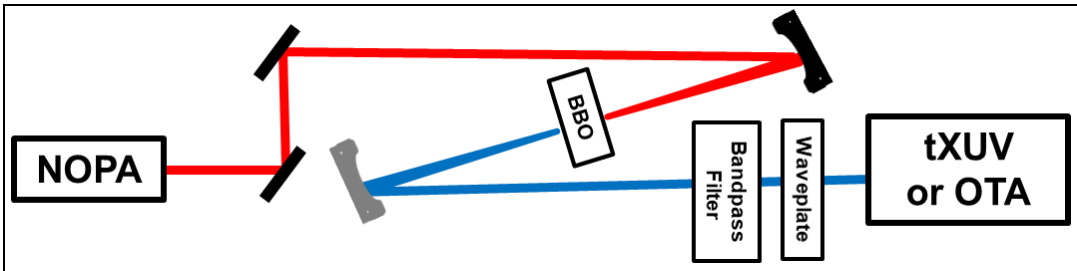

Figure 4.5: The experimental set up to generate 350 nm or 325nm pulses. In the figure, the black rectangles represent Al mirrors. The gray mirror represents a UV enhanced aluminum mirror. The mirrors in the shape of a rectangle with a circular cutout represent concave mirrors with focusing lengths of 150 mm.

Both 350 nm and 325 nm were used as excitation wavelength in this study. The pathway for the generation of 350 nm or 325 nm light is depicted is Figure 4.5. To generate pump wavelengths in the UV range, the visible output from a noncollinear optical parametric amplifier (NOPA, TOPAS-White) is subjected to second harmonic generation (SHG).[79] For this process, a secondary output from the Ti:sapphire driving laser (800 nm, 4 mJ, 35 fs, 1 kHz) is directed into the NOPA.[6] The NOPA can generate visible pump pulses from 450 nm to 750 nm with pulse widths down to 35 fs. At 700 nm and 650 nm, the NOPA power is 20 mW and 18 mW, respectively. To allow for the most reflection possible, protected silver mirrors (Thorlabs, PF10-03-P01) are used to reflect the 700 nm or 650 nm and UV-enhanced aluminum mirrors (Thorlabs, PF10-03-F01) were used to reflect the 350 nm or 325 nm light. The 700 nm or 650 nm output pulses are reflected with protected silver mirrors (Thorlabs, CM254-150-P01, f = 150 mm) into a focusing configuration for the BBO to increase the power output of the second harmonic generation. The beam was focused to decrease the beam size and increase the conversion efficiency of the SHG.[80] The BBO (United Crystals, Type 1, SHG 700 nm, 10x10x1.0 mm) was mounted in a rotatable mount so that the angle of the BBO could be

adjusted to maximize the output power of the 350 nm or 325 nm light. The output of the BBO was then reflected off a UV-enhanced aluminum-coated concave mirror (Thorlabs, CM254-150-P01, f = 150 mm) to refocus the 350 nm or 325 nm output.

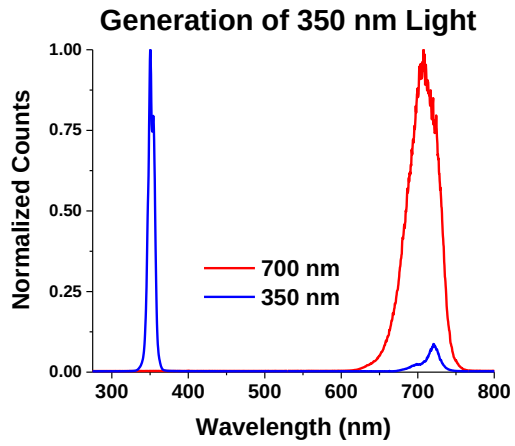

Figure 4.6: The generation of 350 nm light from the second harmonic generation from 700 nm input through a BBO. The counts are normalized and show a peak at 350 nm for the light generation and the 700 nm output from the NOPA.

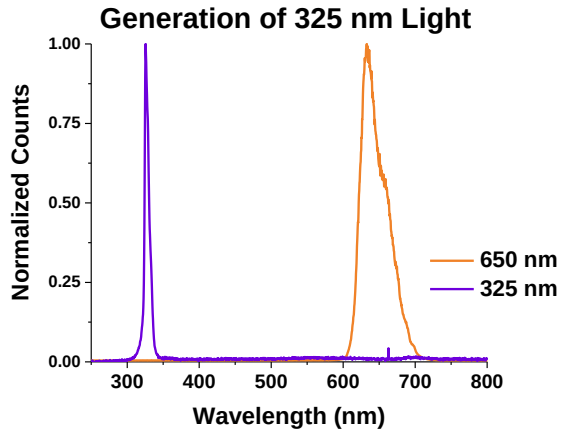

Figure 4.7: The generation of 325 nm light from the second harmonic generation from 650 nm input through a BBO. The counts are normalized and show a peak at 325 nm for the light generation and the 650 nm output from the NOPA.

The output is then directed into a bandpass filter (Thorlabs, FGUV11) which filters out the residual 700 nm or 650 nm light and transmits about 80% of the 350 nm (3.4 mW) or 325 nm (2.9 mW) light. The light is then sent through a waveplate polarizer so the polarization of the pump beam can be adjusted depending on the type of sample used. The pump beam was set to magic angle polarization relative to the probe for solution phase transient absorption measurements and the pump beam was set to a parallel polarization relative to the probe beam for solid state samples.[52] UV-enhanced aluminum mirrors were then used to send the 350 nm or 325 nm pump beams into the sample chamber for tXUV experiments or to the OTA instrument. The 700 nm light spectrum used to generate the 350 nm pulse and the generated 350 nm spectrum are depicted in Figure 4.6. The 650 nm light spectrum used to generate the 323 nm pulse and the generated 323 nm spectrum are depicted in Figure 4.7.

4.2.2 Sample Preparation

Samples of the stacked porphyrin were prepared using a method of imbedding the stacked porphyrin in a polystyrene solution and creating a 200 nm to 400 nm thick polymer film.

This method of film preparation is detailed in unpublished work by the Vura-Weis lab member, Yusef Shari'ati.[81] The method can create submicron films with a uniform thickness needed for ground state M-edge absorption measurements. Dry, oxygen-free benzene was used as the solvent for the stacked porphyrin sample with concentrations ranging from 0.06 mM to 0.32 mM depending on the excitation fraction needed for the selected pump wavelength. An optical spectrum was taken of the stacked porphyrin samples before and after the transient optical experiments to ensure there was no damage to the sample from being pumped.

4.2.3 Transient Optical Absorption Spectroscopy

Optical transient absorption spectroscopy of the stacked porphyrin was performed in benzene solution with pumping at 400 nm, 350 nm, and 325 nm. The optical transient absorption spectroscopy was performed with broadband, approximately 100 fs, probe pulses generated through white light generation from 800 nm pulses focused into a sapphire plate.[8] The white light is transmitted through the sample and refocused onto a spectrometer. The 400 nm pulses were generated from 800 nm pulses sent through a BBO crystal by second harmonic generation. The transient absorption was collected to a delay time of 1 ns for the 400 nm pump and to a delay time of 3 ns for the 350 nm and 325 nm pumps. The delay window was extended to 3 ns for the 350 nm and 325 nm pump wavelengths after the 400 nm pumped transient data showed the long-lived signal had not fully decayed by 1 ns. The 3 ns delay time is the longest time delay available with the delay stage used for the transient optical spectroscopy instrument. The stacked porphyrin in benzene was pumped to an excitation fraction of 21.5% with 1.2 μJ of the 400 nm output with a pump diameter of ~330 μm. The stacked porphyrin in benzene was pumped to an excitation fraction of 8.3% with 1.4 μJ of the 350 nm output with a pump diameter of ~320 μm. The stacked porphyrin in benzene was pumped to an excitation fraction of 5.7% with 0.7 μJ of the 325 nm output with a pump diameter of ~320 μm. The excitation fraction of the stacked porphyrin pumped with 400 nm pump is greater due to the increased absorption of the complex at 400 nm compared to 350 nm and 325 nm.

4.2.4 Transient XUV Absorption Spectroscopy

The tabletop XUV probe was generated through the process of high-harmonic generation (HHG), previously described in the first chapter. The 1 kHz, 35 fs, 800 nm pulse of the NIR driving laser is focused into a semi-infinite gas containing approximately 100 Torr of Neon to

generate approximately 20 fs XUV pulses in the energy range from 40-90 eV.[3] The residual NIR pulses were filtered using a 100 nm thick Al foil and creating a flux of 10^5 photons per pulse are available at the sample position. [8] The spectrometer resolution is measured using the absorption lines of Xe and Xe^+ and has been found to be near 0.4 eV FWHM for these experiments. Transient absorption of the thin film of Fe_2O_3 is used to determine the instrument response function (IRF) of each pump wavelength. For the 400 nm pump, the average IRF was found to be 90 fs FWHM and for the 350 nm pump, the average IRF was found to be 130 fs FWHM. The stacked porphyrin in polystyrene was pumped to an average excitation fraction of 16.8% with 1.2 μJ of the 400 nm. The stacked porphyrin in the polystyrene film was pumped to an average excitation fraction of 17.6% with 1.1 μJ of the 350 nm output from a BBO which doubled 700 nm output from the NOPA.

4.3 Stacked Porphyrin OTA Results

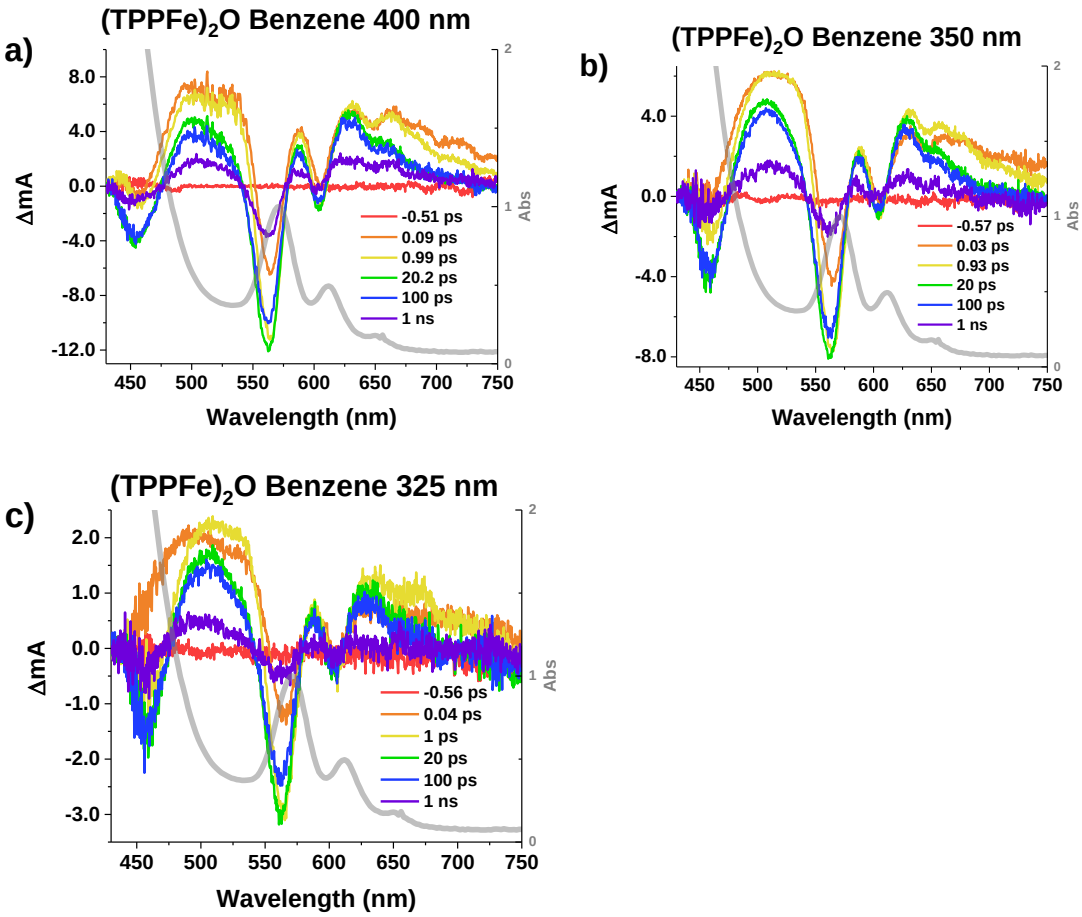

Figure 4.8: The spectral slices for the transient optical absorption of the iron stacked porphyrin in benzene pumped at a) 400 nm, b) 350 nm, and c) 325 nm. The electronic spectrum of the stacked porphyrin is plotted in gray for each plot.

In Figure 4.8, the optical transient absorption spectra of the stacked porphyrin in benzene at various delay times are plotted for each pump wavelength used a) 400, b) 350 and c) 325 nm. The transient spectra represent the difference spectra (Pump ON – Pump OFF) at a selected delayed time from the excitation of the sample. The ground state electronic spectrum of the stacked porphyrin in a solution of benzene is plotted as a thick, gray line with the difference spectra. The electronic spectra of the stacked porphyrin are normalized to the Q-band at 572 nm for each of the above plots so that the magnitude and position of the absorption bands of the ground state of the stacked porphyrin can be compared to the position and magnitude of the transient absorption bands of the stacked porphyrin as the signals grow or decay over time. The contour plots of the transient optical absorption of the iron stacked porphyrin in benzene pumped

at 400 nm, 350 nm, and 325 nm showing the dynamics at each time point out to nanosecond range are depicted in Supplementary Figure 5.3.

For the transient absorption spectra of the stacked porphyrin pumped at 400 nm, at delay times near 10 fs and 1 ps, a broad positive feature is present centered near 515 nm. Between 10 fs and 1 ps, this positive feature at 515 nm decays slightly. Between 10 fs and 1 ps, the positive feature from 620 nm to 750 nm also decays slightly. However, the bleach feature at 560 nm appears to gain nearly a third of the original magnitude between 10 fs and 1 ps. Near 450 nm, a bleach feature appears after 1 ps and gains its full intensity of the decay by 20 ps. After 1 ps, the positive feature near 620 nm maintains the full magnitude of the positive feature, while the positive feature past 650 nm decays significantly. By 20 ps, the large bleach feature near 560 nm appears to be at its maximum intensity. The smaller bleach at 605 nm also appears to be at the maximum of the bleach by 20 ps. Both bleach features decay after 20 ps and are continuing to decay at 1 ns. By 100 ps, the bleach at 450 nm is at the maximum of the decay and the positive feature at 620 nm maintains the maximum of the positive feature. By 100 ps, the bleach feature at 560 nm is decaying along with the continued decay of the broad positive feature centered at 515 nm.

The transient absorption spectrum pumped at 400 nm can be compared to the static UV-vis spectrum of the stacked porphyrin to elucidate the identity of the transient states. The strong bleach feature at 560 nm is slightly blue shifted from the absorption of the Q-band of the ground state centered at 570 nm. The smaller bleach feature at 605 nm is only slightly blue shifted from the Q-band of the ground state centered at 612 nm. Therefore, these bleach features most likely correspond to the ground state bleach of the Q-bands of the stacked porphyrin. The positive features centered at 515 nm and between 620 nm and 750 nm correspond to the formation of an excited state with new absorption features at these wavelengths. The bleach at 450 nm appears within the Soret band of the stacked porphyrin. The delayed formation of this bleach suggests that the initial excited state species lacks absorption in this region.

The transient absorption spectrum of the stacked porphyrin pumped at various wavelengths can be compared to see the effect of the pump wavelength on the excited state dynamics. The pump wavelengths of 400 nm, 350 nm, and 325 nm appear to have similar effects on the stacked porphyrin excited state dynamics. The transient absorption spectra at all pump

wavelengths contain a broad positive feature near 515 nm that decays after 1 ps. All transient absorption spectra contain the ground state bleach of the Q-bands and the positive absorption features past 620 nm. The transient absorption spectra appear to differ with respect to the transient features near 450 nm at early delay times. For both the 400 nm and 350 nm pumped transient absorption spectra, before 1 ps, there is no absorption near 450 nm and a small bleach begins to appear after 1 ps. For the 325 nm pumped transient absorption spectra, at 40 fs there is a positive feature at 450 nm that maintains positive absorption until about 1 ps. After 1 ps, a small bleach forms at 450 nm and continues to grow into a larger bleach, maximizing by 20 ps and decaying past 1 ns. A positive feature before 1 ps at 450 nm is only present in difference spectrum of the stacked porphyrin pumped at 325 nm and is not present when the complex is pumped at 350 nm or 400 nm.

4.3.1 Kinetic Analysis of Stacked Porphyrin OTA

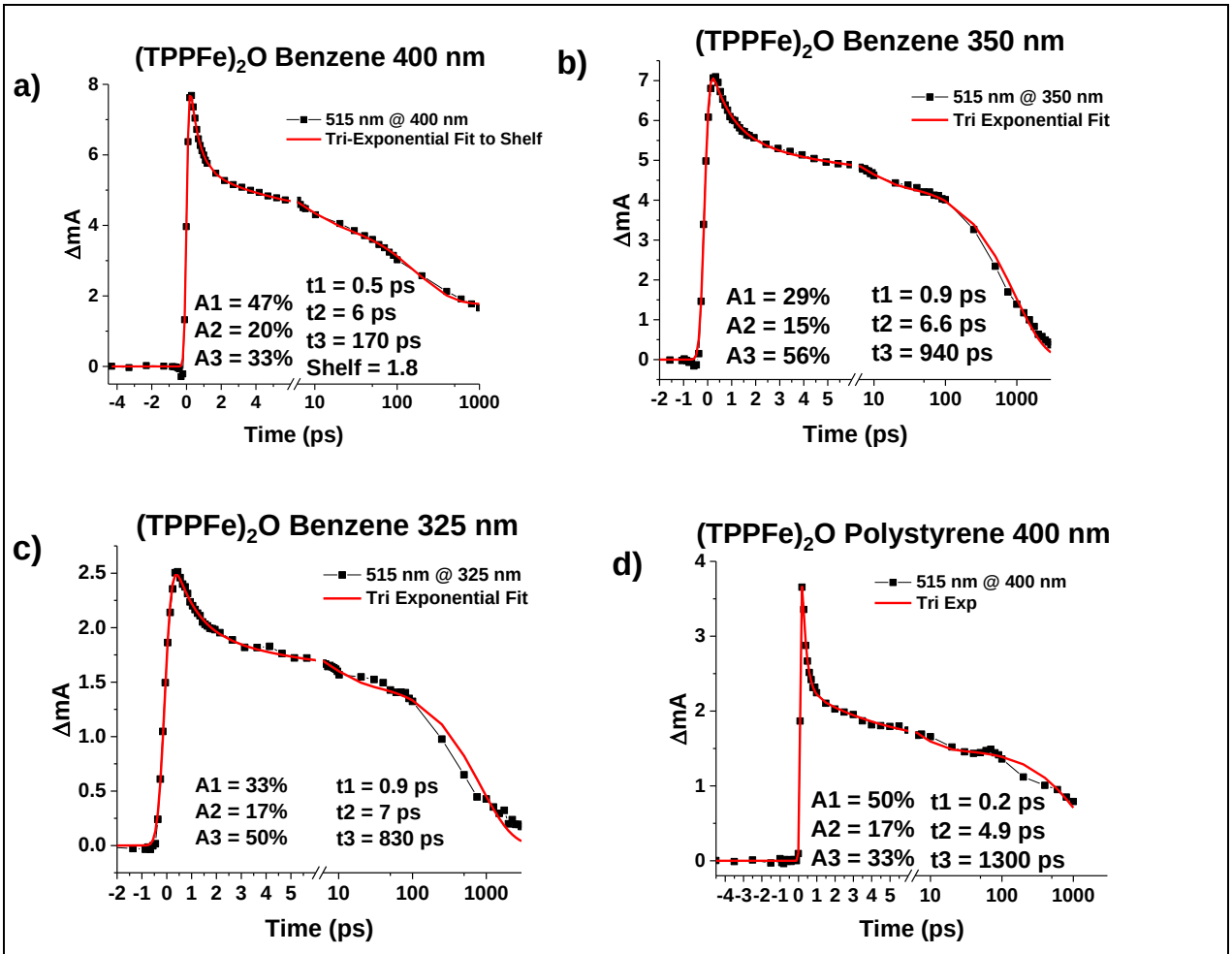

Figure 4.9: Probe wavelength 515 nm for the stacked porphyrin pumped at a) 400 nm, b) 350 nm, and c) 325 nm in benzene and d) for the stacked porphyrin in polystyrene pumped at 400 nm.

The analysis of the kinetics of certain probe wavelengths can be used to determine the dynamics of the excited states of the stacked porphyrin and determine how many excited states may be present. The center of the broad positive feature at 515 nm was analyzed for each of the pump wavelengths used, depicted in Figure 4.9. The errors for the lifetimes determined are detailed in Supplementary Table 5.2. The trace at 515 nm was best fit with a tri-exponential function. For this probe wavelength, a bi-exponential function was attempted but was found not to fit the trace well at time early than 10 ps. A four-exponential fit was also used for the 515 nm probe wavelength however, the fit did not offer much improvement to the triexponential fit. The lifetimes associated with the tri-exponential fit of the stacked porphyrin in benzene pumped at 350 nm are τ_1 = 0.9 ps, τ_2 = 6.6 ps, and τ_3 = 940 ps. The lifetimes associated with the tri-

exponential fit of the stacked porphyrin in benzene pumped at 325 nm are τ_1 = 0.9 ps, τ_2 = 7 ps, and τ_3 = 830 ps. The time constants for the tri exponential fits for the 350 nm and 325 nm pump of the stacked porphyrin are similar and suggest the existence of similar decay pathways. The lifetimes of the first state when pumped with 350 nm and the 325 nm wavelengths are both less than 1 ps, the second state lifetimes are both between 6 and 7 ps and the third state lifetimes are both greater than 800 ps. When a tri-exponential function was fit without a shelf for the 400 nm pumped data, the first lifetime was 0.8 ps, the second lifetime was 45 ps and the third lifetime was 1560ps. The lifetime of the first and third terms are like the data pumped at 350 nm and 325 nm. However, the lifetime of the second term is significantly different. The second lifetime value for the 400 nm pumped data was obtained from poor fit to the region between 1 ps and 10 ps of the 515 nm time trace (see Supplementary Figure 5.4). For the stacked porphyrin probe wavelength of 515 nm pumped at 400 nm, the tri-exponential function needed to be fit to a shelf for the section of the probe kinetic between 1 ps and 10 ps accurately. In Figure 4.9a, the tri-exponential function gives a lifetime of τ_2 = 6 ps which is like the value of the second lifetime obtained from the tri-exponential fits of 515 nm pumped at 350 nm and 325 nm in Figure 4.9b and Figure 4.9c. The value of the shelf obtained for the 400 nm pumped data was 1.8 and has resulted in a shorter lifetime of the third state of 170 ps. This third lifetime is significantly shorter than the values obtained for the stacked porphyrin pumped at 350 nm and 325 nm. The lifetime of the third state for the tri-exponential fit to the shelf is 170 ps and the lifetime of the third state without the shelf is 1560 ps. The delay time window for the 400 nm pumped data was out to 1 ns whereas the data for the 350 and 325 nm had a delay window out to 3 ns. This longer time window may have allowed for a more accurate fit of the lifetime of the third and longest-lived state. For the 400 nm pumped data, a tri-exponential fit is needed to accurately fit the first and the third lifetime and a tri-exponential fit to a shelf is needed to accurately fit the first and the second lifetimes. An experiment with the stacked porphyrin pumped at 400 nm out to a delay time of 3 ns or greater may be needed to accurately fit all lifetimes. For all pump wavelengths, the suggested lifetime for the three excited states is about 1 ps for the first state, about 6.5 ps for the second state, and around 1 ns for the final and longest lives state.

The probe wavelength for the kinetics of the stacked porphyrin in a polystyrene film can be compared to the kinetics in a solution of benzene. Figure 4.9d depicts the probe wavelength of the stacked porphyrin in a polystyrene film pumped at 400 nm. The probe wavelength is fit with

a tri-exponential function and the time constants determined are τ_1 = 0.2 ps, τ_2 = 4.9 ps, and τ_3 = 1300 ps. The time constants obtained for the polystyrene film are similar to the time constants obtained in the benzene solution. The lifetime of the initial state is shorter for the polystyrene thin film sample, and the lifetime of the final state is longer. It appears that the polystyrene matrix versus benzene solution does not drastically change the time constants observed at the 515 nm probe wavelength.

The time constants suggested for the states at the 515 nm probe above are further supported when examining the probe at 450 nm time trace for the stacked porphyrin transient optical absorption pumped by all three wavelengths, depicted in Figure 4.10. For the 400 nm pumped data in Figure 4.10a, a bleach feature is present at 450 nm and a bi-exponential fit is used to best fit the data. The first lifetime determined is 5.3 ps and the second lifetime is 800 ps. For the 350 nm in Figure 4.10b, a bi-exponential fit determined is 7 ps and the second lifetime is 650 ps. The first lifetimes determine for the 450 nm probe of around 6 ps for both pump wavelengths correspond to the lifetime of the second state determined from the 515 nm probe. The second lifetimes determined for the 450 nm probe of greater than 600 ps for both pump wavelengths correspond to the lifetime of the third state determined from the 515 nm probe. It appears that the 450 nm probe does not have a change in absorption corresponding to the first excited state seen by the 515 nm probe with a lifetime near 1 ps. However, the 450 nm probe wavelength of the stacked porphyrin pumped at 325 nm shows an initial positive feature appearing before 2 ps which decays into a longer-lived bleach. This positive feature is not observed or is not as strong when the stacked porphyrin is pumped at 350 nm or 400 nm. For the probe wavelength 450 nm of the stacked porphyrin pumped at 325 nm in Figure 4.10c, the time trace is best fit to a tri-exponential function, the lifetimes determined are τ_1 = 0.8 ps, τ_2 = 9 ps, and τ_3 = 700 ps. These lifetimes are similar to the lifetimes obtained for the 515 nm probe suggesting that the lifetimes correspond to the same excited states. Based off these results, it seems that the first excited state for the stacked porphyrin does not have an absorption change before 1 ps when pumped at 400 nm and 350 nm but the first excited state has a positive absorption at 450 nm when the stacked porphyrin is pumped at 325 nm.

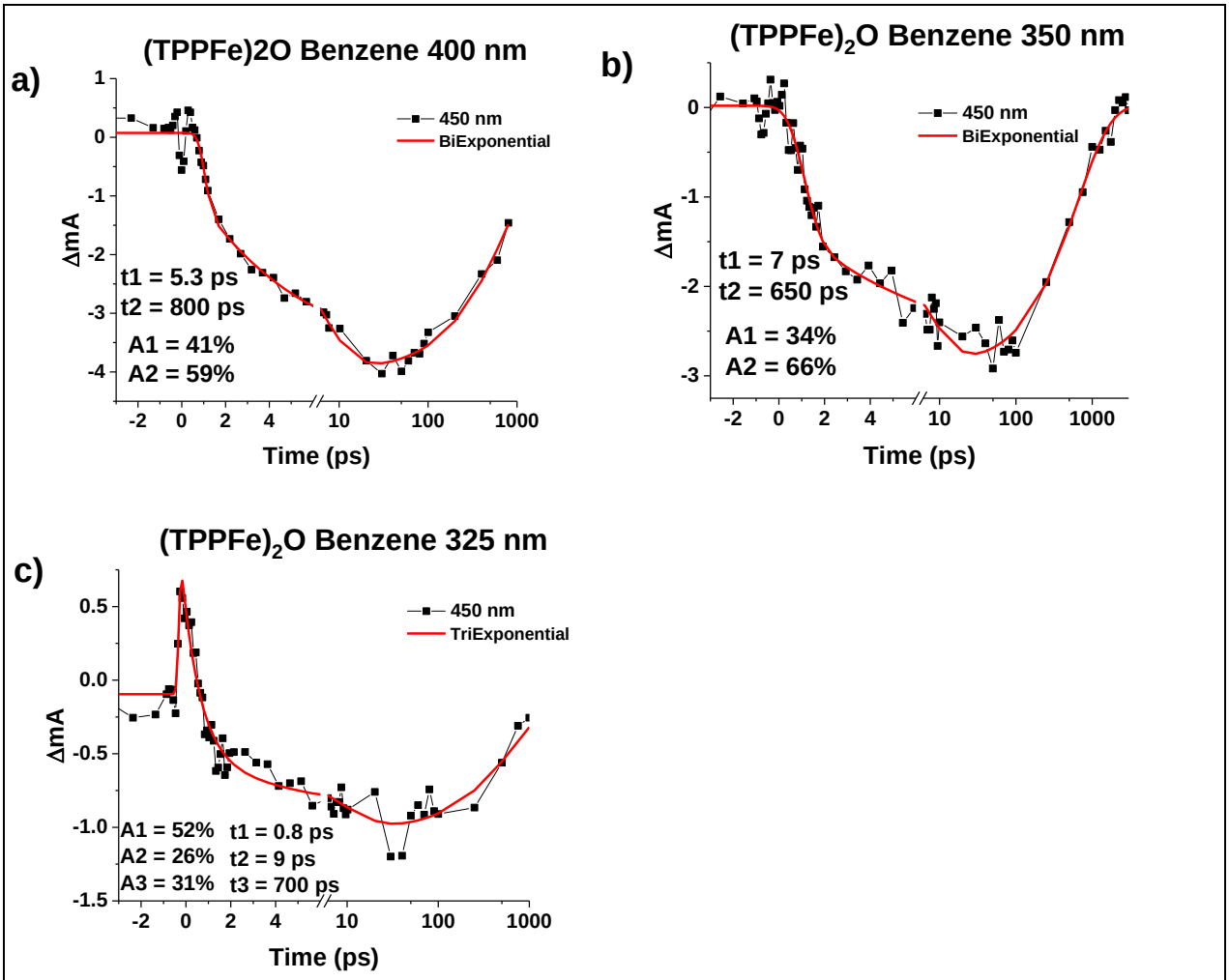

Figure 4.10: Probe wavelength 450 nm for the stacked porphyrin pumped at a) 400 nm, b) 350 nm, and c) 325 nm.

4.4 Stacked Porphyrin OTA Discussion

4.4.1 Global Analysis of the Stacked Porphyrin

For the stacked porphyrin transient visible absorption pumped at 400 nm, 350 nm, and 325 nm the spectral evolution in benzene is similar for all the pump wavelengths. A 3-state sequential model for global analysis was applied to all the wavelengths and produced similar component spectra and lifetimes for all the data sets using the program Glotaran.[82] The three-state sequential model for the global analysis depicts the decay back to the ground state (GS) with the sequence $X \rightarrow Y \rightarrow Z \rightarrow GS$, depicted in Figure 4.11. Due to the similarity of the transient spectra of the three states determined for each global analysis, the states for each pump wavelength have been labeled State X, State Y, and State Z and it is asserted that the identity of

the three states are the same for each pump wavelength. Due to the similarity of the time constants for all three states across the pump wavelengths used, an approximate lifetime based on the values from each pump wavelength will be assigned to each state. State X will be referred to as the state with a 1 ps lifetime, State Y as the state with the 10 ps lifetime, and State Z with the 1 ns lifetime.

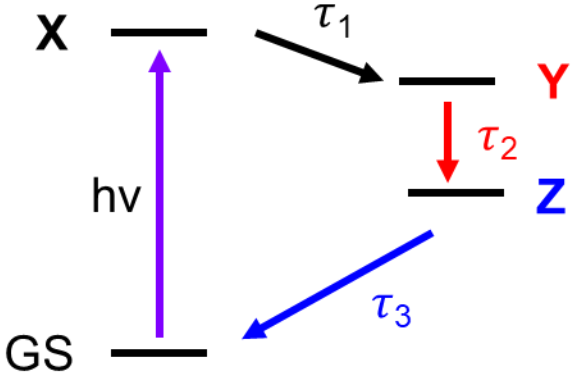

Figure 4.11: The three-state sequential model used for the global analysis of the optical transient spectra of the stacked porphyrin in benzene pumped at 400 nm.

In addition to the sequential model given above, a three-state parallel model was considered and used to fit the data set, as shown in Supplementary Figure 5.5.5. The three-state parallel model with a branching to the ground state from the second state was considered because of the similarities in the spectral features of the second and third state of the sequential model. It was thought that the second and third state may be hot and cold excited states of the same state.[6] However, when this model was used, the reconstructed fits did not fit the time traces of the positive feature at 515 nm or the bleach feature at 560 nm well for the stacked porphyrin data set shown in Supplementary Figure 5.6 . The three-state sequential model was chosen as the best model to represent the stacked porphyrin excited state dynamics because the reconstructed fits from the global analysis fit the time traces of time traces of the positive feature at 515 nm or the bleach feature at 560 nm well. The reconstructed fit matches the time traces well as seen in Supplementary Figure 5.7.

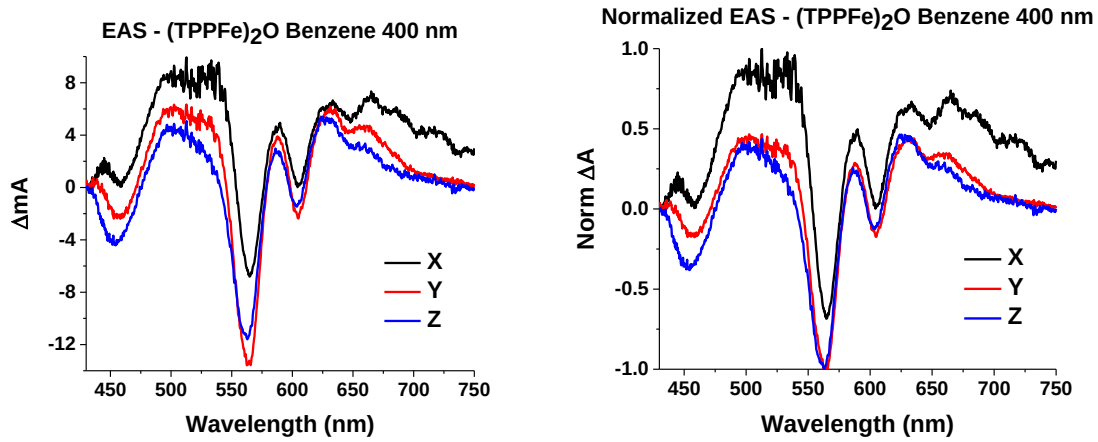

Figure 4.12: a) The component spectra obtained from the global analysis of a 3-state sequential model of the stacked porphyrin transient visible absorption in benzene pumped at 400 nm. The lifetime of State X is 1.0 ps, the lifetime of State Y is 8.6 ps, and the lifetime of State Z is 840 ps. b) The component spectra normalized to the strongest positive absorption signal and bleach signal.

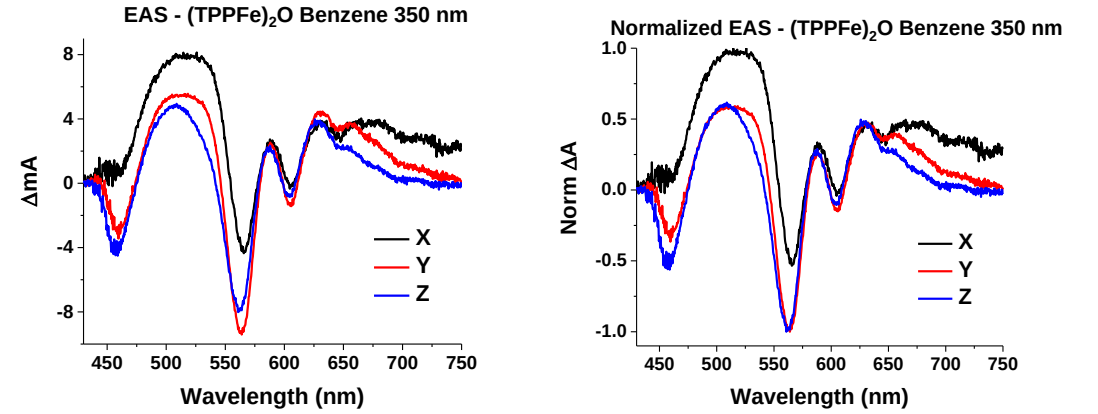

Figure 4.13: a) The component spectra obtained from the global analysis of a 3-state sequential model of the stacked porphyrin transient visible absorption in benzene pumped at 350 nm. The lifetime of State X is 0.9 ps, the lifetime of State Y is 5.9 ps, and the lifetime of State Z is 720 ps. b) The component spectra normalized to the strongest positive absorption signal and bleach signal.

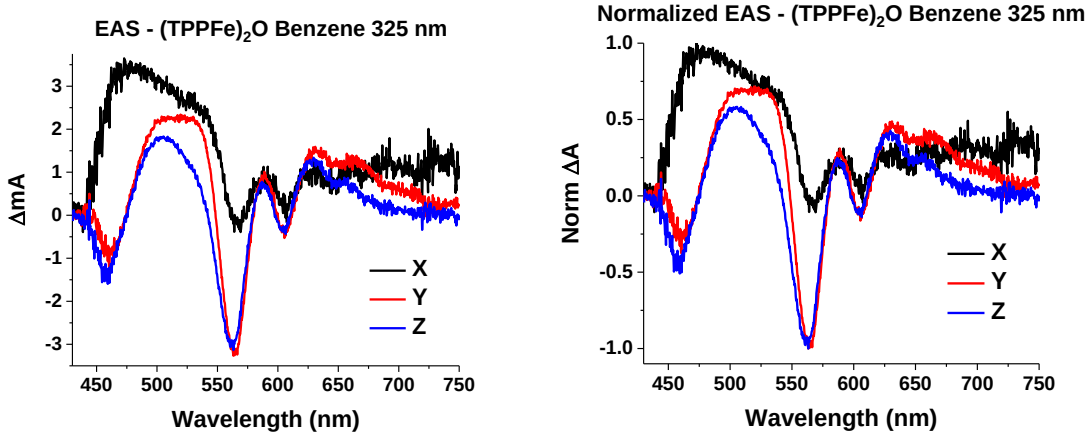

Figure 4.14: The component spectra obtained from the global analysis of a 3-state sequential model of the stacked porphyrin transient visible absorption in benzene pumped at 325 nm. The lifetime of State X is 0.5 ps, the lifetime of State Y is 4.0 ps, and the lifetime of State Z is 420 ps. b) The component spectra normalized to the strongest positive absorption signal and bleach signal.

4.4.2 Identifying the ~1 ps Excited State of the Stacked Porphyrin

The LMCT state for the stacked porphyrin contains two subunits, one with an Fe(II) center and one with an Fe(III) center. The transient spectrum will therefore show negative features corresponding to the loss of the Fe(III) porphyrin and positive features corresponding to the absorption spectrum of the newly-formed Fe(II) porphyrin. Previous literature has shown that when Fe(III)TPPCl is irradiated with 355 nm laser light, Fe(II)TPP + Cl• are produced which results in a positive feature forming at 450 nm.[77] This suggests that an excited state containing an Fe(II)TPP should contain a positive feature near 450 nm. The excited state spectrum from Fe(III)TPPCl in benzene at early times depicting the Fe(II) LMCT state can also be used to simulate an Fe(II) excited state for the stacked porphyrin. In Figure 4.15, the excited state spectrum of Fe(III)TPPCl at 490 fs, depicting a transient Fe(II) state, contains a sharp positive feature of 450 nm and a broad positive feature from 545 nm to 650 nm. Figure 4.15 also depicts an estimated excited state of a porphyrin containing an Fe(III) state generated from subtracting the electronic spectra of the iron stacked porphyrin from the spectrum of the monoporphyrin Fe(III)TPPCl. The Fe(III)TPPCl spectra presents the monoporphyrin Fe(III) containing states present in the Anion/Cation state.[61] This simulated excited state is meant to represent the Anion/Cation state formed after the stacked porphyrin follows Pathway B upon photoexcitation. The simulated difference spectrum contains a strong bleach at 450 nm and a positive feature near 515 nm. The summation of the simulated excited state shows a weak bleach to the blue of 450

nm and a weak positive feature to the red of 450 nm. The simulated spectrum has been scaled to have a similar magnitude, however, changing the magnitudes can result in a cancelation of absorption at 450 nm, a small bleach at 450 nm, or small positive feature at 450 nm. The state will also contain a broad positive feature from 600 nm to 700 nm. Looking at State X for the stacked porphyrin pumped at 400 nm and 350 nm in Figure 4.12 and Figure 4.13, a weak positive feature can be seen near 450 nm and a broad positive feature past 600 nm. State X for the stacked porphyrin pumped at 325 nm, in Figure 4.14, a stronger positive feature is present at 450 nm. This suggests that a greater population of the Fe(II) state is generated compared to the other excitation wavelengths. The band at 320 nm of the stacked porphyrin has been speculated as a charge transfer state so an excitation at 325 nm may result in a higher yield of the formation of the LMCT state.[74] The similarity of the spectral features of State X to and blue plot of an Fe(II) containing LMCT state in Figure 4.15 suggest that State X is an LMCT excited state.

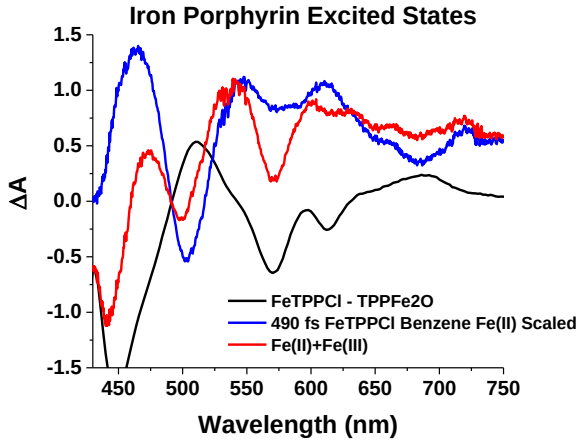

Figure 4.15: The speculated iron porphyrin excited states containing and Fe(II) and Fe(III) center. The black plot is the subtraction of the stacked porphyrin ground state visible spectrum from the ground state visible spectrum of FeTPPCl. This spectrum serves to simulate an Fe(III) porphyrin excited state subunit for the stacked porphyrin. The blue plot is the excited spectrum of FeTPPCl in Benzene at 490 fs. It has been established that this excited state contains an Fe(II) LMCT state of the iron porphyrin. The red plot is the addition of the Fe(III) and and Fe(II) simulated excited states.

The difference in the population of Fe(II) and Fe(III) in the initial excited state can explain the difference in the absorption features at early times when the stacked porphyrin is pumped at 325 nm versus 350 nm or 400 nm. When the stacked porphyrin is pumped at 325 nm, there is a positive feature at 450 nm which can be associated with the presence of an Fe(II) excited state, however, this positive feature is not present when the porphyrin is pumped at 350 nm or 400 nm. The presence of a positive feature at 450 nm may suggest that pumping the stacked porphyrin generates a large population of the LMCT excited state compared to the Fe(III) containing state, like the unreacted ground state of the stacked porphyrin, resulting in a positive absorption at 450 nm. At pump wavelengths of 350 nm and 400 nm, a smaller proportion of Fe(II) is

generated and the positive absorption is cancelled out by the negative absorption associated with the formation or a Fe(III) excited state.

4.4.3 Comparison of Component Spectra to Fe(IV) Simulated State

To determine if any of the excited states of the stacked porphyrin contain an Fe(IV) center, the component spectra can be compared to a simulation of the difference spectra of an Fe(IV) porphyrin. A study that formed a porphyrin containing a ferryl group collected the visible spectrum of the porphyrin of $TPPFe^{IV}=O$ in a solution of toluene at 183 K.[71] To simulate an excited state spectrum of the stacked porphyrin containing a ferryl group, the visible spectrum of the stacked porphyrin was subtracted from the visible spectrum of the porphyrin $Fe^{IV}=OTPP$. The visible spectrum of $TPPFe^{IV}=O$ was obtained by digitalized the plot in the study.[71] In Figure 4.16, the difference spectrum of a simulated Fe(IV) containing excited state is shown in the maroon plot. The different spectrum contains a large bleach starting at 500 nm and extending to lower wavelengths. A small positive feature is present at 510 nm and 545 nm and a small bleach is present at 570 nm. It should be noted that for the stacked porphyrin, an excited state with a ferry intermediate will also contain an Fe(II) center, the true excited state of the Ferryl intermediate will be a combination of both an Fe(IV) and Fe(II) difference spectra. The figure below contains only the Fe(IV) intermediate so those features can be compared to the component spectra to identify traits of a ferryl intermediate. In Figure 4.16, the Fe(IV) difference spectra is compared to the component spectra of states X, Y and Z of the stacked porphyrin pumped at 400 nm. Neither of the component spectra contain a large bleach that extends to 500 nm. All the component spectra contain a broad positive feature near 500 nm. The small bleach at 570 nm for the Fe(IV) simulated spectrum is similar to the bleach of the component spectra of the stacked porphyrin however, the magnitude and position do not match. The Fe(IV) simulated difference spectra does not appear to match well with any of the component spectra from the global analysis. There is not definitive evidence to support the presence of an Fe(IV) intermediate state upon excitation with 400 nm. Based on these comparisons, it appears unlikely that the stacked porphyrin followed Pathway A to the Disproportionated state after photoexcitation (shown in Figure 4.2). The component spectra of the stacked porphyrin pumped at 350 nm and 325 nm also do not match well with the simulated Fe(IV) intermediate spectrum as well (see Supplementary Figure 5.9).

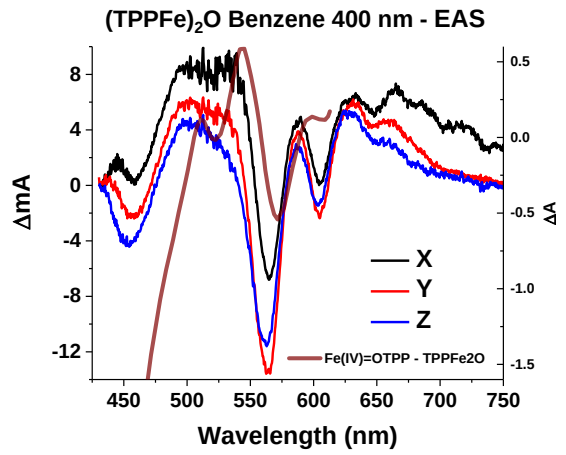

Figure 4.16: The comparison of component spectra of the stacked porphyrin pumped at 400 nm to a simulated Fe(IV) excited state. The black, red, and blue plots are States X, Y, and Z, respectively, from the global analysis of the stacked porphyrin pumped at 400 nm in benzene. The maroon plot is the subtraction of the stacked porphyrin ground state visible spectrum from the ground state visible spectrum of Fe(IV)=OTPP digitized from Chin *et al.*[71] This spectrum serves to simulate an Fe(IV) porphyrin excited state subunit for the stacked porphyrin.

4.4.4 Identifying the ~10 ps and ~1 ns Excited State of the Stacked Porphyrin

The component spectra of State Y and State Z can be compared to a simulated difference spectrum containing an Fe(III) excited state. A difference spectrum containing an Fe(III) state serves as a simulation of the Anion/Cation state formed after the stacked porphyrin follows Pathway B after photoexcitation (shown in Figure 4.2). As mentioned above, the estimated excited state of a porphyrin containing an Fe(III) state is generated from subtracting the electronic spectra of the iron stacked porphyrin from the spectrum of the monoporphyrin Fe(III)TPPCl. Figure 4.17 compares the spectral feature of States Y and Z to the simulated Fe(III) excited state. The spectra of the 3 plots all contain a bleach near 450 nm and a broad positive feature centered near 515 nm, bleaches near 560 nm and 610, and a broad positive feature past 625 nm. The similarity of the component spectra to the simulated difference spectrum support that idea that State Y and Z contain an Fe(III) center and can be identified as the Anion/Cation state.

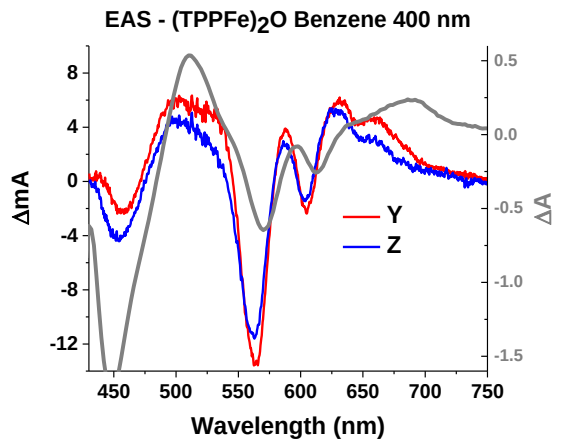

Figure 4.17: The comparison of component spectra of the stacked porphyrin pumped at 400 nm to a simulated Fe(III) excited state. The red and blue plots are States Y and Z, respectively, from the global analysis of the stacked porphyrin pumped at 400 nm in benzene. The gray plot is the subtraction of the stacked porphyrin ground state visible spectrum from the ground state visible spectrum of FeTPPCl. This spectrum serves to simulate an Fe(III) porphyrin excited state subunit for the stacked porphyrin.

Also, states Y and Z contain an almost identical spectral shape. The difference in the spectra of State Y and Z appear to be present in the magnitude of the bleach and 450 nm and the bleach at 560 nm, these differences are more pronounced in the unnormalized plot of the component spectra in Figure 4.12. The similarity of the component spectra of states Y and Z suggests that both states can be identified as the Anion/Cation state. It is proposed that state Y is the vibrationally hot Anion/Cation state and that State Z is the vibrationally cooled Anion/Cation state. The lifetime of State Y corresponds of 10 ps corresponds to the vibrational relaxation of the Anion/Cation state. This 10 ps timescale is similar to the timescales observed in vibrational relaxation in the excited states of a nickel porphyrin.[9]For both the single wavelength kinetics and global analysis, a long-lived state with a lifetime around 1 ns was found for each solvent environment and pump wavelength. It is proposed that this vibrationally cooled, long-live state is the Anion/Cation state with charge separated Fe(III)TPP+ and Fe(III)TPPO- subunits. The identity of this state as a charge separated state is supported because the 1 ns lifetime is typical for a charge separated state. In previous studies of porphyrin-fullerene polyads, it has been found that the charge separated species containing a positively charge zinc porphyrin and negatively charge fullerene decayed to recombine with a lifetime in the single nanosecond range.[83]

4.5 Speculation of Relaxation Pathway from OTA Results

Based on the kinetic and global analysis of the optical transient absorption of the stacked porphyrin, there are three excited states identified upon photoexcitation with 400 nm, 350 nm, or 325 nm. Significant differences in the relaxation pathway for each excitation wavelength were not found. The first state was identified as an LMCT state based off the similarity of the spectral features to the LMCT state identified from the iron monoporphyrin Fe(III)TPPCl. The second and third excited states were identified was a vibrationally hot and cold Anion/Cation state

containing two Fe(III) centers. This identification was made by comparing the spectral features of the component spectra to a simulated difference spectra containing an Fe(III) center. None of the excited states were thought to contain the Disproportionated state containing an Fe(IV) center. These OTA results suggest that the iron stacked porphyrin follows Pathway B after photoexcitation and generates the Anion/Cation state. To solidify the selection of this pathway, the metal center of the stacked porphyrin can be directly probe with transient XUV absorption spectroscopy. This technique will clearly identify the oxidation states of each stacked porphyrin excited state and determine the pathway of relaxation after photoexcitation.

4.6 Stacked Porphyrin XUV Absorption Results

4.6.1 Stacked Porphyrin Ground State and Simulated Excited States

The ground state XUV spectrum of the stacked porphyrin $(TPPFe)_2O$ in a polystyrene film was measured. The process of making polystyrene films of the stacked porphyrin is described in the next chapter. For the raw ground state absorption spectra the resonant feature at the iron $M_{2,3}$ edge is on top of a broad nonresonant background from the photoionization of the metal and ligand valence electrons.[3] The nonresonant absorption can be fit to a power-law baseline at the lower energy region and this background can be subtracted, to give only the metal resonant feature. The ground state spectrum is plotted in Figure 4.18. The resonant signal from the Fe $M_{2,3}$ edge is a peak centered at 57.4 eV. The iron absorption peak of the stacked porphyrin is at the same position of the iron peak in the monoporphyrin Fe(III)TPPCl, indicating the expected Fe(III) centers for both irons in the stacked porphyrin. The XUV absorption plots of the stacked and monoporphyrin are overlapped in the Supplementary Figure 5.11.

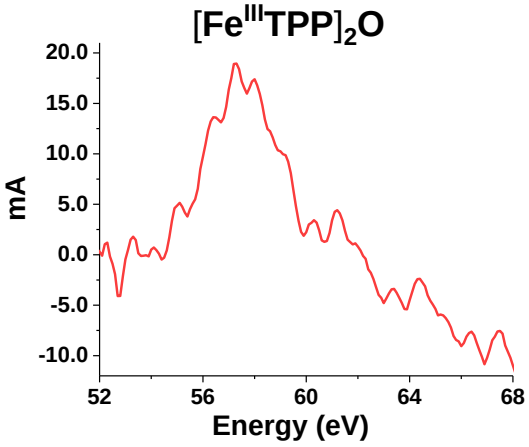

Figure 4.18: The ground state absorption spectrum of the iron stacked porphyrin in a polystyrene film. The nonresonant absorption baseline has been subtracted for this spectrum.

The XUV absorption of potential transient states for the iron stacked porphyrin $(TPPFe)_2O$ were simulated. Simulations were done by Clare Leahy using the program CTM4XAS.[24] The parameters for the simulations are detailed in Supplementary Table 5.1 and were modeled after the parameters used for the excite state simulations of the iron monoporphyrin.[8] The difference spectra for the excited states of the iron stacked porphyrin were determined from the simulated ground states of an iron monoporphyrin with the oxidation states of Fe(III), Fe(II), and Fe(IV). The ground state absorption spectra for these varying oxidation states is shown in Figure 4.19a. The absorption peaks of the simulated ground states can be explained by the allowed transitions observed in the correlation diagram corresponding to each oxidation state, detailed in the dissertation of Ryan Ash from the Vura-Weis group.[19] For the Fe(III) simulation, a d^5 high spin system, the allowed transitions correspond to a strong peak for transition from the $^1A_{1g}$ ground state to $^6T_1$ state and a weak peak from the ground state to a $^6T_1$ state that branched from a formally forbidden atomic state.[19] The black plot in Figure 4.19a shows the strong peak for the Fe(III) absorption at 58 eV and the weaker peak at 53.8 eV. For the Fe(II) simulation, a d^6 high spin system, from the ground state ^5D, there are three allowed transitions to ^5F, ^5D, and ^5P states which correspond to the three overlapping peaks at 55.5 eV, 57 eV, and 59 eV.[19] For the Fe(IV) simulation, a d^4 high spin system, from the ground state ^5D, there are three allowed transitions to ^5F, ^5D, and ^5P states which correspond to the three separated peaks at 55.5 eV, 59 eV, and 64 eV.[19]

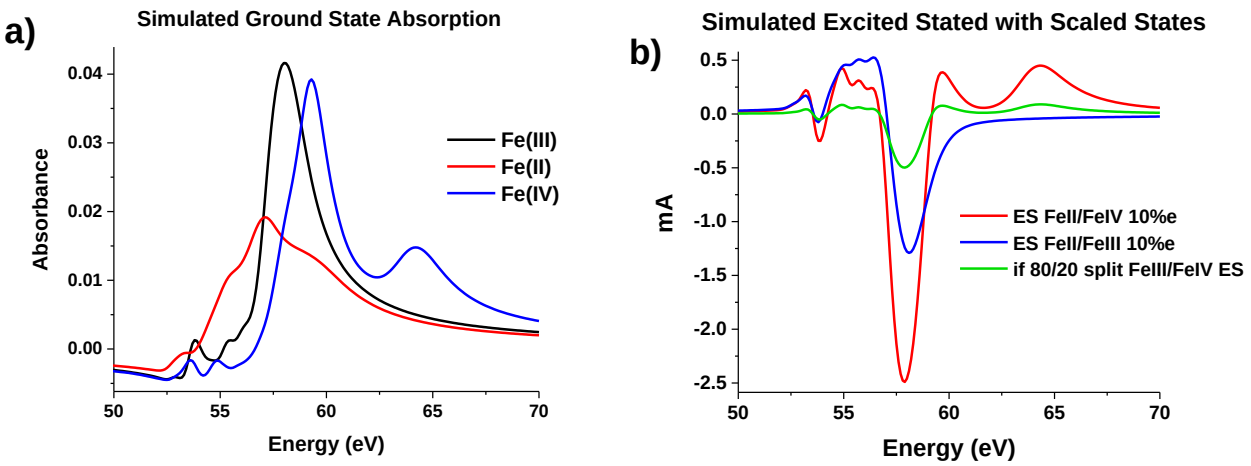

Figure 4.19: a) The ground state of the iron porphyrin with the oxidation states Fe(III), Fe(II), or Fe(IV). b) The simulated excited states of predicted combinations of iron oxidations states in b) of that stacked porphyrin calculated with CTM4XAS. The red plot depicts an excited state containing and Fe(II) and Fe(IV) center with a 10% excitation fraction. The blue plot depicts an excited state containing and Fe(II) and an Fe(III) center with a 10% excitation fraction. The green plot depicts the excited state spectrum containing a 80% of the Fe(III)/Fe(III) state and 20% of the Fe(II)/Fe(IV) state. These simulations were generated with the scaled excited stated for the varying iron oxidation states (calculations performed by Clare Leahy).

Figure 4.19b depicts the simulated excited states for the transient M-edge absorption of the stacked porphyrin containing two Fe(III) centers. The red plot in the figure shows the excited state spectrum containing an Fe(II) and Fe(IV) center with a 10% excitation fraction. This plot contains small positive absorption features at 55.5 eV, 60 eV, and 64.5 eV and a large bleach feature centered at 57.9 eV. The blue plot contains the simulated excited state containing an Fe(II) and Fe(III) center with an 10% excitation fraction. This plot contains a positive feature centered at 55.5 eV and a bleach feature centered at 58 eV. The green plot contains the simulated spectra of an excited state containing a combination of excited states with 80% from a Fe(III)/Fe(III) state and 20% from the Fe(II)/Fe(IV) state, like the outcome suggested from Guest *et al*.[61] This plot contains a bleach centered at 57.8 eV and small positive features at 55.5 eV, 60 eV and 64.5 eV. These simulations show what to expect from the excited state dynamics of the iron stacked porphyrin. This also shows that if a larger ratio of the Fe(III)/Fe(III) state is formed compared to the Fe(II)/Fe(IV) excited state (80:20), it will be difficult to observe the positive features at 60 eV and 64.5 eV. Overall, transient XUV spectroscopy will be able to probe the excited state dynamics of the iron centers of the stacked porphyrin and elucidate the excited state pathway.

4.6.2 tXUV of Stacked Porphyrin

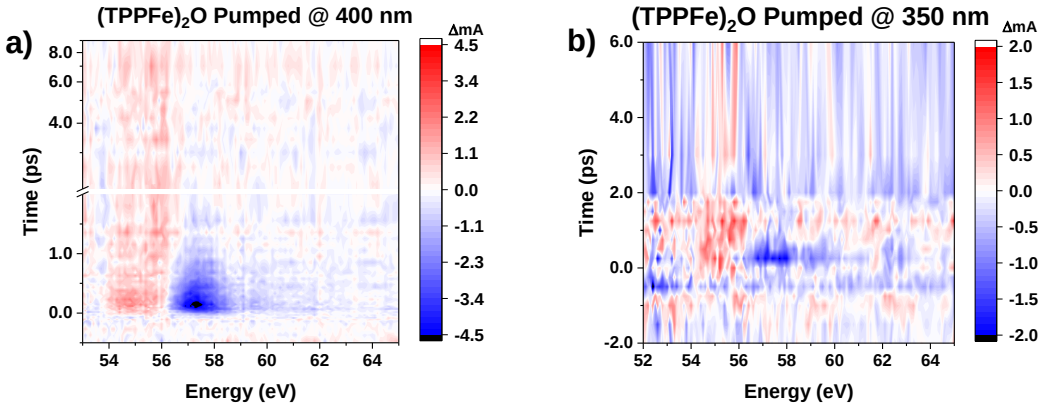

Figure 4.20: a) The contour plot of the stacked porphyrin pumped at 400 nm out to 9 ps. b) The contour plot of the stacked porphyrin pumped at 350 nm out to 6 ps.

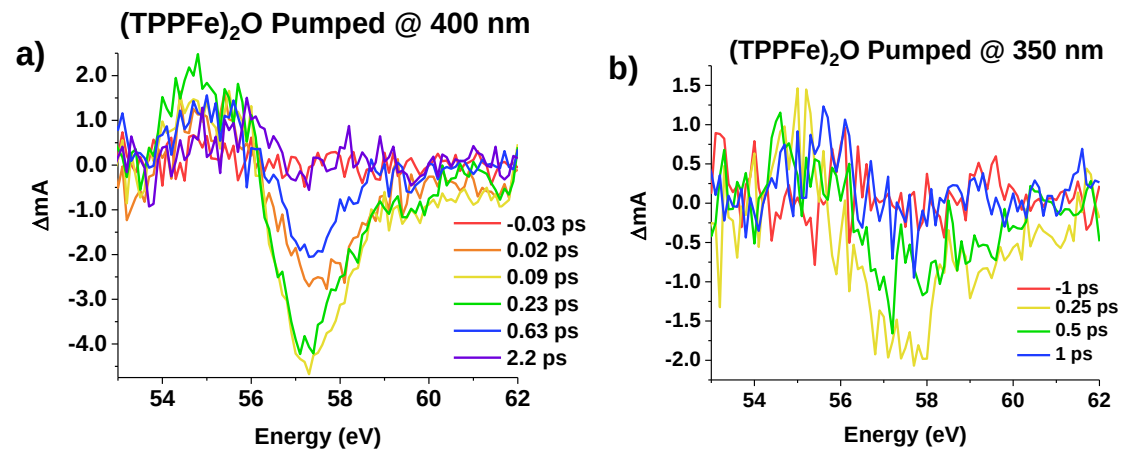

Figure 4.21: a) The XUV transient absorption spectra of the stacked porphyrin after 400 nm excitation. b) The XUV transient absorption spectra of the stacked porphyrin after 400 nm excitation.

Transient XUV spectroscopy was performed on polystyrene films of the stacked porphyrin $(TPPFe)_2O$ and was pumped with the wavelength 400 nm and 350 nm. Figure 4.20 shows the contour plot of the transient absorption spectra, where $\Delta A = -\log_{10}(I_{\text{pump on}}/ I_{\text{pump off}})$, of the stacked porphyrin pumped at 400 nm and 350 nm, respectively. Figure 4.20a shows the transient spectra out to a delay time of 9 ps. For this data set, there is a bleach feature centered at 57.5 eV and a positive feature centered at 55 eV. The energy range of the plot is cut off after 65 eV because there are no apparent absorption changes past 62 eV. Figure 4.20b shows the

transient spectra out to a delay time of 6 ps. For this data set, there is also a small bleach feature centered at 57.5 eV and a positive feature centered at 55 eV. The energy range of the plot also is cut off after 65 eV because there are no apparent absorption changes past 62 eV. Figure 4.21a contains the spectral slices of the stacked porphyrin pumped at 400 nm from -30 fs to 2.2 ps. This spectral evolution shows that the bleach at 57.5 eV appears by 20 fs, reaches the full intensity by 90 ps, and the signal slightly decays by 230 fs. The bleach figure begins to decay at 630 fs and has completely decay by 2.2 ps. The positive feature at 55 eV appears to grow in weakly by 20 fs and reaches the maximum positive absorption by 230 fs. The positive feature begins to decay after 230 fs and a small positive feature persists at 2.2 ps. Figure 4.20b contains the spectral slices of the stacked porphyrin pumped at 350 nm from -1 ps to 1 ps. The spectral evolution of the difference spectra shows that the bleach centered at 57.5 eV is present and at maximum intensity at 250 fs. The signal begins to decay after 0.5 ps and disappears by 1 ps. The smaller positive absorption feature appears by 250 fs and retains positive absorption through 1 ps. Both the spectral evolution of the stacked porphyrin pumped at 400 nm and 350 nm contain a bleach feature at 57.4 eV and a positive feature at 55 eV. The spectral features of the different pump wavelengths appear to form and decay at similar timescales.

4.6.3 Kinetic Analysis of Stacked Porphyrin tXUV

The analysis of the kinetics of certain probe wavelengths were used to determine the dynamics of the excited states of the stacked porphyrin. For the stacked porphyrin pumped at 400 nm, Figure 4.22a shows that the time trace at 54.8 eV was fits well with a mono-exponential function with a shelf with a value of 0.6. The time constant when fit with a shelf was 0.33 ps. Supplementary Figure 5.12 depicts the time trace of 54.8 eV fit with a bi-exponential decay function. The time constants found are $\tau_1 = 0.3$ ps $\pm$ 0.1 ps and $\tau_2 = 17$ ps $\pm$ 23 ps. The bi-exponential function fits the time trace well; however, the error of the second time constant is larger in magnitude than the time constant. This large error suggests that the bi-exponential function may not be able to fit the long-lived second state. The low error of the shelf used to fit the mono-exponential function suggests that the second state is long-lived past the 9 ps delay window of the time trace. This long lived state may be a heat signal that is sustained past the delay window of the time trace.[8] The time trace at 54.8 eV was collected out to 1 ns in a separate experiment, however, the signal to noise ratio of the time trace was too high to determine the lifetime of the second, long-lived signal. For the stacked porphyrin pumped at 400 nm, the time

trace was probed at 57.3 eV in Figure 4.22b. It was found that the time trace was fit well with a mono-exponential function with a time constant of 0.54 ps ± 0.04 ps. The time trace at 57.4 eV, representing the same bleach feature at 57.3 eV, was collected out to 1 ns to confirm the short-lived nature of the bleach feature. Figure 4.22c, depicts the time trace at 57.4 eV with a mono-exponential fit. The time constant obtained from the mono exponential fit is 0.50 ps ± 0.09 ps. This confirms that the bleach feature is not observed past the initial decay.

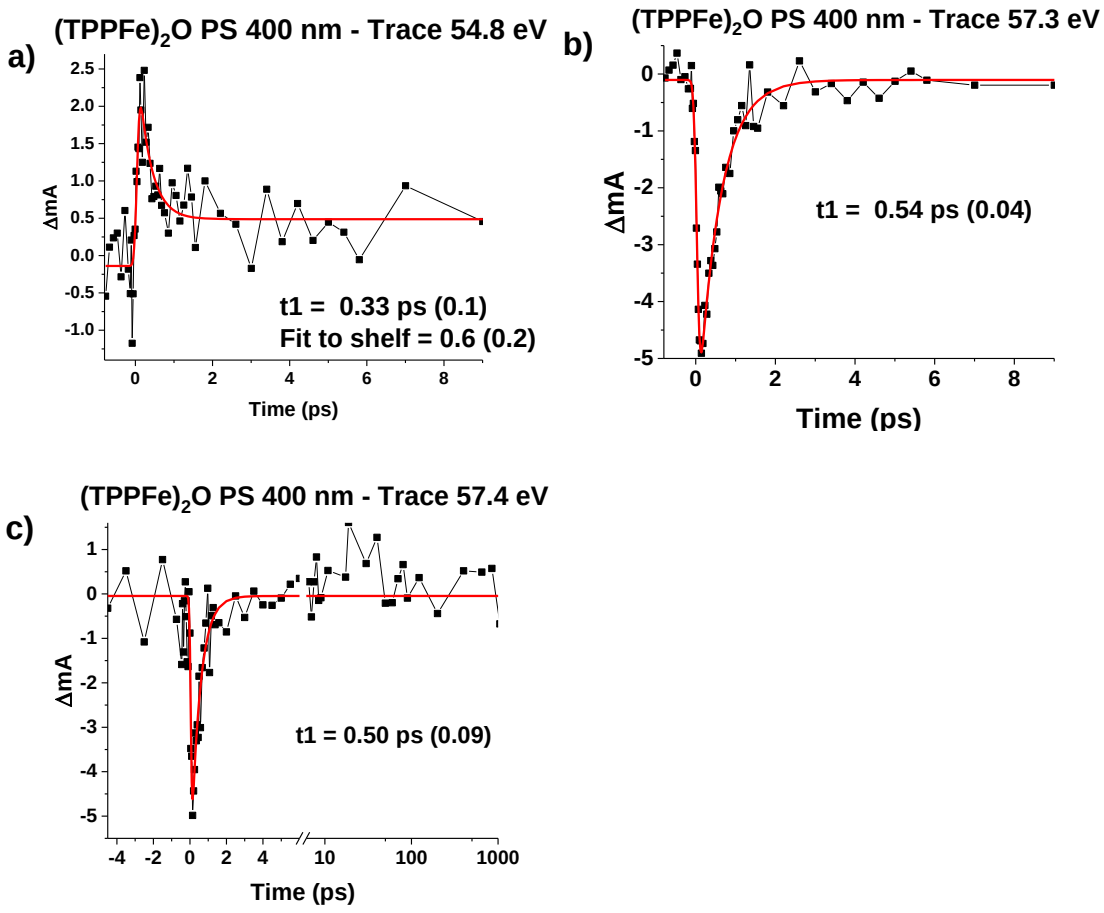

Figure 4.22: The time traces of the stacked porphyrin in a polystyrene film pumped at 400 nm with mono-exponential fits in red. The errors for the kinetic fit parameters are shown in parentheses following the value. a) The time trace at 54.8 eV out to 9 ps. The trace is fit with a shelf. b) The time trace at 57.3 e V with a time delay out to 9 ps. c) The time trace at 57.4 eV out to 1 ns.

The kinetic profile of the time traces corresponding to the positive feature and bleach feature of the stacked porphyrin pumped at 350 nm were also examined. In Figure 4.23a, the kinetics of the positive feature are determined by examining the time trace at 55.2 eV. The time

trace is fit with a mono-exponential decay function with a shelf. The time constant determined is 0.3 ps ± 0.2 ps and the value of the shelf is 0.4 ± 0.1. The time constants of the positive feature of the stacked porphyrin pumped at 350 nm and pumped at 400 are similar. Both time constants are near 0.3 ps and both mono-exponential functions were best fit to a shelf. The time trace of the bleach feature observed was monitored at 57.5 eV and fit with a mono-exponential function, depicted in Figure 4.23b. The mono-exponential function required that the time zero position be fixed into order to fit the decay. The value of time zero for the time trace was corrected with the position of time zero determined from a thin film of α-Fe_2O_3 pumped at 350 nm during the same time period as the stacked porphyrin data collection. The value of the time constant was determined to be 0.6 ps ± 0.3 ps. The time trace of the bleach was collected out to 1 ns, depicted in Figure 4.23c. The time trace representing the bleach feature was fit at 57.4 eV with a mono-exponential function. The time constant was determined to be 0.5 ps ± 0.2 ps. The time constant for the bleach feature from the time trace out to 1 ns is similar to the value of the time trace out to 6 ps. This suggests that the bleach feature centered at 57.4 eV for the stacked porphyrin pumped at 350 nm has a lifetime near 0.6 ps and there is not a detectable longer-lived state present.

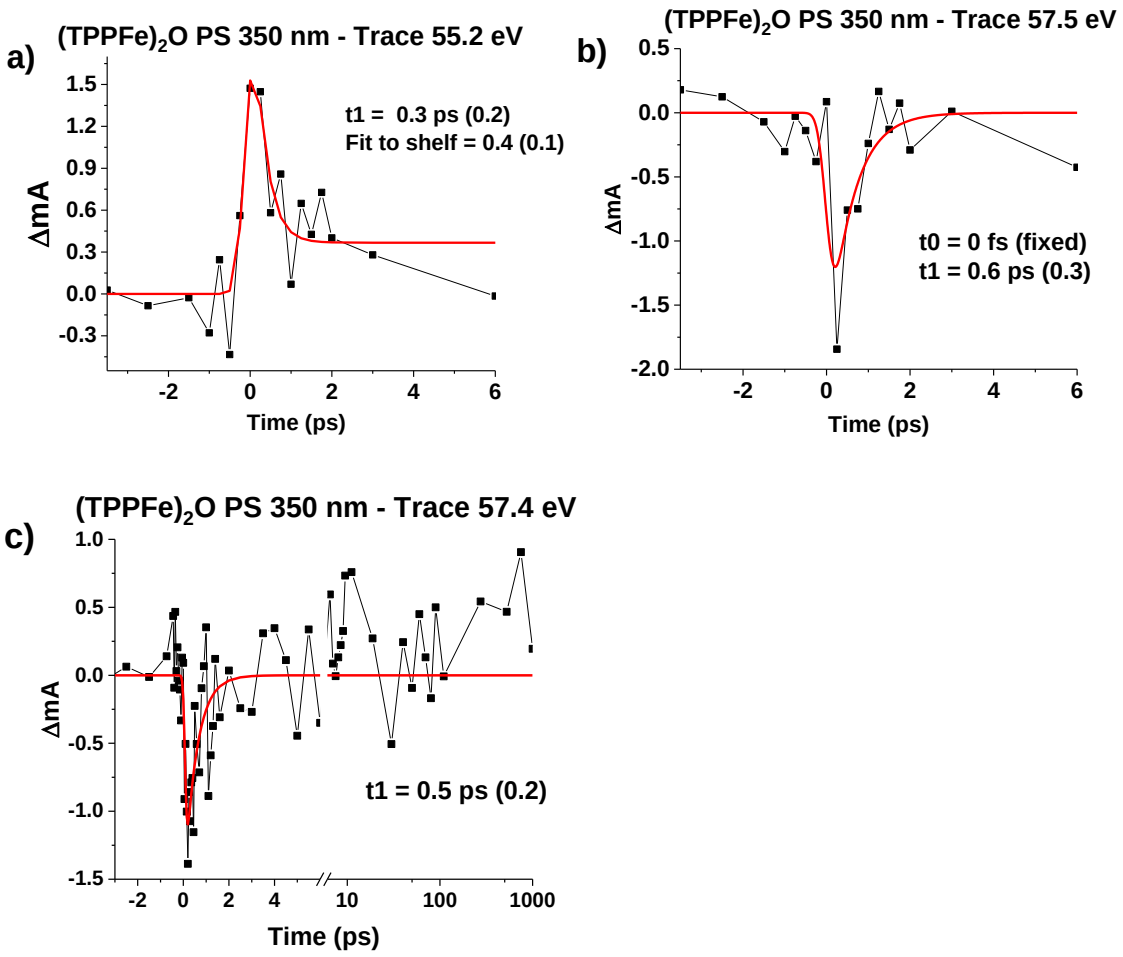

Figure 4.23: The time traces of the stacked porphyrin in a polystyrene film pumped at 350 nm with mono-exponential fits in red. The errors for the kinetic fit parameters are shown in parentheses following the value. a) The time trace at 55.2 eV out to 6 ps. The trace is fit with a shelf. b) The time trace at 57.5 e V with a time delay out to 6 ps. c) The time trace at 57.4 eV out to 1 ns.

When comparing the time traces for the stacked porphyrin pumped at 400 nm and 350 nm, the values obtained for the time constants for the bleach feature and positive feature are similar. Both pump wavelengths produced a bleach feature near 57.5 eV that decayed within 0.6 ps and produced a positive absorption feature with a lifetime near 0.3 ps when fit to a shelf. The similarity of the spectral features and lifetime of the pumped wavelengths suggest that the 400 nm and 350 nm may be creating the same excited state which follows the same decay pathway observable through XUV.

4.7 Stacked Porphyrin XUV Absorption Discussion

4.7.1 Global Analysis of Stacked Porphyrin tXUV Pumped at 400 nm

A global fit of the transient XUV spectra of the stacked porphyrin pumped at 400 nm out to 9 ps was performed. A global fit of the tXUV spectra pumped at 350 nm was not performed due to the similarity dynamics to the data pumped at 400 nm and because more time steps and a further delay windows was used for the 400 nm pumped data set. The global fit for the stacked porphyrin pumped at 400 nm contained a two-state sequential model which returns to the ground state (GS) with $A \rightarrow B \rightarrow GS$. A two-state sequential model was chosen due to the lifetimes observed from the single wavelength kinetic analyze. The short lifetime of the positive feature and bleach suggested the presence of a state with a lifetime less than 1 ps. The shelf required to fit the positive feature suggested the presence of a weak, long lived state.

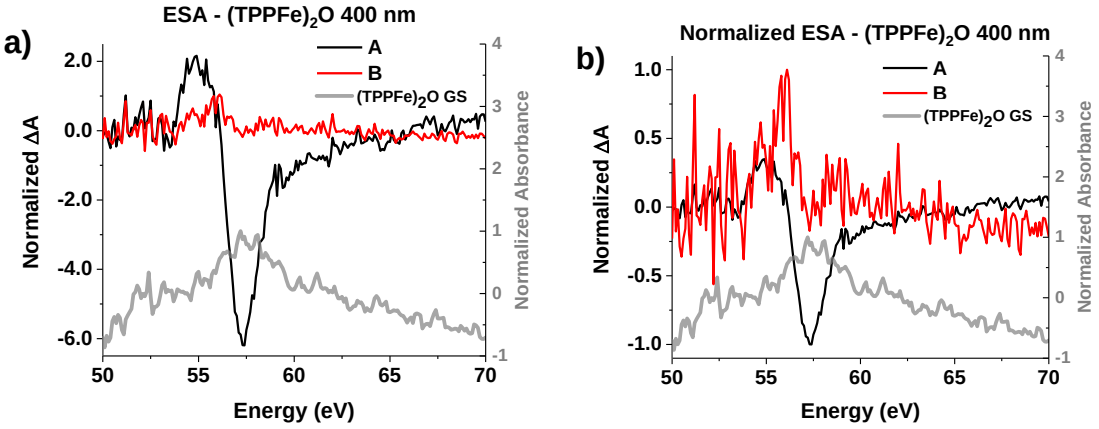

Figure 4.24: a) The component spectra of a 2-state sequential model global analysis of the transient XUV absorption of the stacked porphyrin in a polystyrene film pumped at 400 nm. b) The component spectra normalized to the strongest positive and negative absorption change feature. The gray plot in both a) and b) is the baselined and normalized ground state spectrum of a polystyrene film of the stacked porphyrin. The lifetime of State A is 0.5 ps and the lifetime of State B is 30 ps.

Figure 4.24a shows the component spectrum of State A and State B. The lifetime of state A is 0.5 ps and the lifetime of State B is 30 ps. Reconstructed traces from the global fit for the positive feature and bleach well. Figure 4.25a depicts the time trace of the positive feature at 55.5 eV with the fit from the global analysis and Figure 4.25b depicts the time trace of the bleach at 57.4 eV with the fit from the global analysis. In both plots, the fit from the two-state sequential model fits the experimental data well. For the positive feature, the fit appears to capture the long-

lived state present while also capturing the short-lived feature of the bleach. In Figure 4.24b the component spectra are normalized to compare the position of the spectral features. State A contains a small positive feature near 55 eV and a stronger bleach feature at 57.4 eV. In Figure 4.24a the plot contains the ground state spectrum of the stacked porphyrin in a polystyrene film with a peak from the Fe(III) center at 57.4 eV. The bleach present in State A is clearly a ground state bleach feature of the Fe(III) state. The spectral features of State A match the LMCT state identified in the excited state dynamics of the monoporphyrin Fe(III)TPPCl pumped at 400 nm.[8] The strong red-shifted absorbance of State A supports the claim that the state contains a Fe(II) LMCT state. State A also corresponds to the Fe(II)/Fe(III) excited state depicted in Figure 4.19. This excited state accounts for the population of the Fe(III) and the Fe(II) subunits that would be generated in an LMCT excited stated of the stacked porphyrin. Therefore, State A can be assigned as an LMCT state containing Fe(II) and Fe(III) centers.

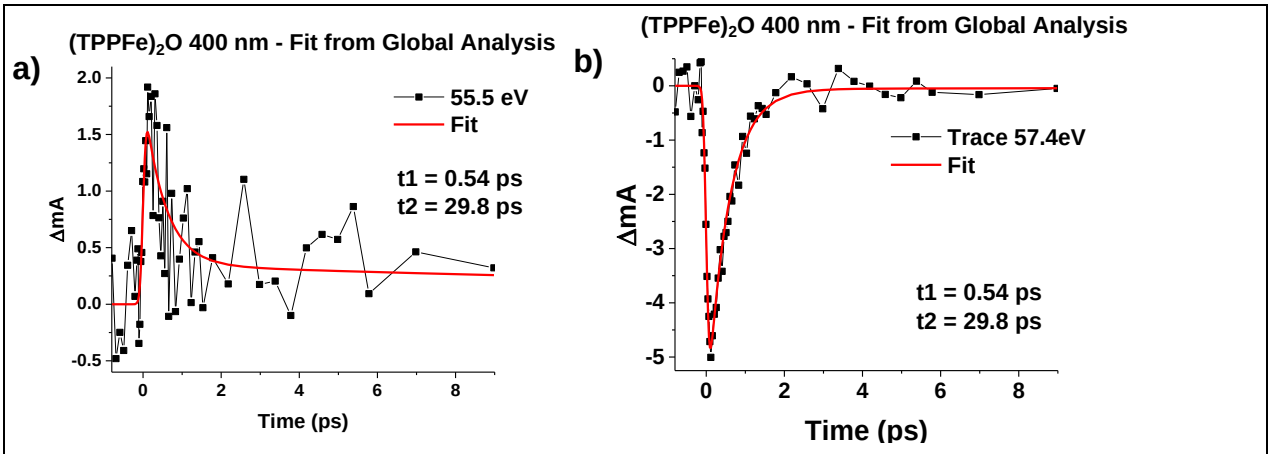

Figure 4.25: Times traces at 55.0 and 57.4 eV with the reconstructed traces from the two-state sequential global analysis. Stacked porphyrin pumped at 400 nm.

State B contains a positive feature at 56 eV that is approximately 3 times the noise of the baseline. The 30 ps lifetime of State B is longer than the delay time window of the data set used and should be considered an approximate lifetime. The transient signal of State B is weak and has an unnormalized magnitude of 1 mA at 56 eV. This weak, positive feature is consistent with a long-lived heat signal observed in other transient XUV and X-ray absorption experiments using thin films.[84] A long-lived heat signal is present in the XUV transient absorption results of the monoporphyrin Fe(III)TPPCl on a 50 nm Si_3N_4 film pumped at 400 nm. To determine if a long

lived transient signal was present in a thin polymer film, a transient XUV absorption experiment was conducted with Fe(III)TPPCl in a polystyrene thin film using similar instrument conditions to the stacked porphyrin experiment. It was found that heat signal, exhibited by a long-lasting positive feature at 54.7 eV. Figure 4.26 shows the kinetic trace of the positive feature of Fe(III)TPPCl with a mono-exponential fit. The mono-exponential function is fit to a shelf to account for the long-lasting heat signal. The similarity of the long-lasting positive feature for Fe(III)TPPCl and $(TPPFe)_2O$ suggests that this feature is a heat signal.

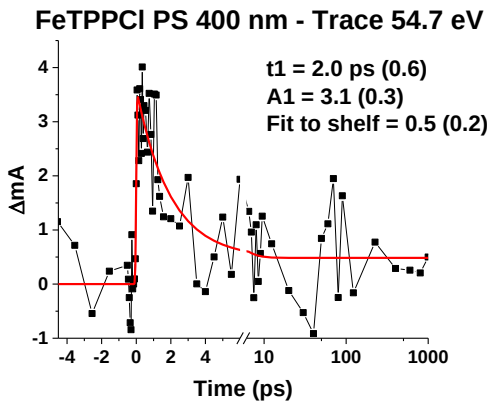

Figure 4.26: The time trace of the transient XUV absorption of FeTPPCl in a polystyrene pumped at 400 nm at the probe energy 54.7 eV. This trace is fit with mono-exponential to a shelf to capture the short-lived positive feature.

The component spectra do not support the formation of an transient species containing an Fe(IV) state. From Figure 4.19, the simulation of an excited state containing an Fe(II) and Fe(IV) would contain a positive features at 60 eV and 64 eV corresponding to the contributions from the Fe(IV). The spectra of State A and B do not contain positive features at these energies. With the excitation fractions used and noise level of the instrument, an Fe(IV)/Fe(II) Disproportionated state was not observed. This does not rule out the formation of an Fe(IV)/Fe(II) state but suggests that the population of Fe(IV)/Fe(II) stated formed upon excitation is not sufficient to be detected within these conditions. Furthermore, there does not appear to be an XUV active signal for the stacked porphyrin by 0.5 ps. This suggests that there are not any detectable excited states involving either of the iron center centers of the stacked porphyrin past the 0.5 ps decay. While the global analysis was performed on the 400 nm, the same conclusion of the formation of excited states can likely be applied to what was observed for the 350 nm pumped stacked porphyrin.

4.7.2 Comparison of OTA and tXUV Results

For each of the pump wavelengths for the stacked porphyrin transient optical absorption spectra, the initial State X spectral component has a lifetime of less than 1 ps. The similar timescale for each pump wavelength further supports the assignment of the same excited state for State X across each pump wavelength. The lifetime of State X is like the lifetime of State A

determined from the global analysis of tXUV of the stacked porphyrin pumped at 400 nm. The lifetime of the initial state from the OTA analysis is slightly larger than the lifetime of the initial state from the tXUV analysis. This difference in lifetime could be explained by the different sample matrix used between OTA (a benzene solution) and tXUV (polymer film). For the OTA results, it was found that the lifetime of the initial state was longer when the stacked porphyrin was in a benzene solution compared to the stacked porphyrin embedded in a polystyrene film. State A has been identified as the LMCT state of the stacked porphyrin after an electron has been excited from the bridging oxygen ligand to one of the Fe(III) centers to form an Fe(II) excited state. State X from the OTA analysis has been shown to have characteristics of an Fe(II) containing state based on the changes in absorption at 450 nm. Therefore, State X from the OTA global analysis and State A from the tXUV analysis represent the same initial LMCT state of the stacked porphyrin excited state dynamics.

From the tXUV analysis, State B appears to represent a heat signal from the thin film and does not appear relevant to the remaining excited states of the stacked porphyrin. Therefore, when considering the second and third component spectra from the OTA analysis, Y and Z, appear to represent states that are XUV-dark. This suggests that the oxidation state of the iron centers on state Y and Z contain the same oxidation state as the ground state of the stacked porphyrin which is an Fe(III). This supports the analysis of the component spectra of states Y and Z from the OTA studies which identifies states as the Anion/Cation state.

4.8 Proposed Stacked Porphyrin Pathway Upon Excitation

Based on the tXUV and OTA analysis of the stacked porphyrin pumped at 400 nm, the predominant relaxation pathway is proposed in the Jablonski diagram in Figure 4.27. The results suggest upon excitation of the stacked porphyrin, an LMCT state containing an Fe(II) and an Fe(III) center is formed. This state then relaxes in about 1 ps into the XUV-dark Anion/Cation state containing two Fe(III) centers. This second and third state

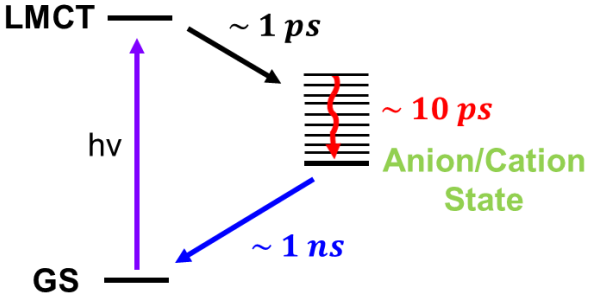

Figure 4.27: The proposed Jablonksi diagram for the decay pathway of the iron stacked porphyrin after photoexcitation.

determined from the OTA global analysis contain similar spectral features suggesting that the second state is a vibrationally hot excited state, and the third state is a vibrational cooled excited state. The vibrationally hot Anion/Cation state relaxes into the cooled vibrational state in about 10 ps. The cooled Anion/Cation then recombines to form the initial ground state in about 1 ns. This pathway suggests that upon photoexcitation, the stacked porphyrin predominantly follows Pathway B and forms the Anion/Cation state, depicted in Figure 4.28. Overall, this model suggest that within the experimental conditions of the tXUV and OTA studies in this work, the Disproportionated state containing an Fe(II)/Fe(IV)oxo intermediate was not observed.

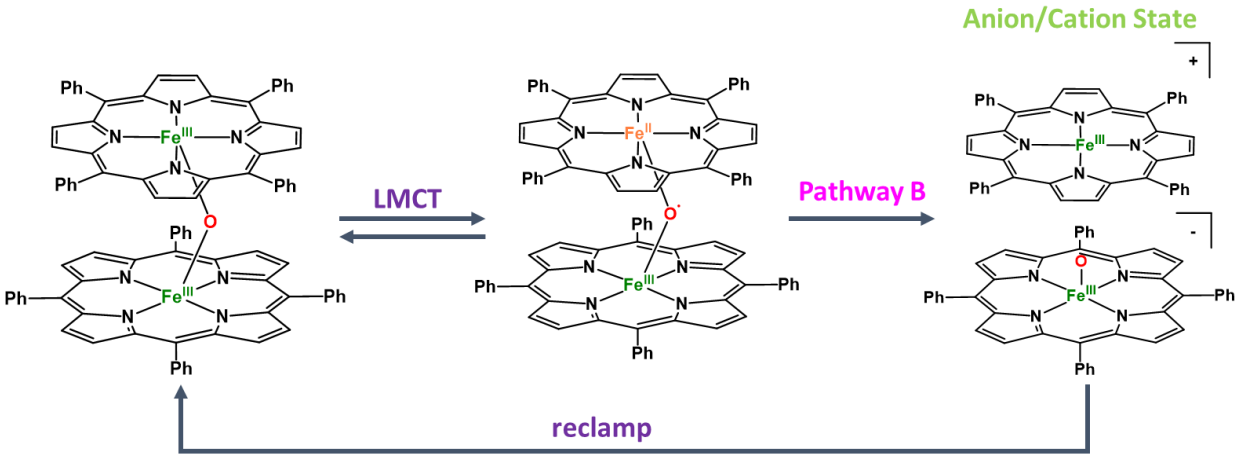

Figure 4.28: The relaxation pathway determined from the tXUV and OTA results of the stacked porphyrin pumped at 400 nm.

4.9 Conclusion

The excited state dynamics of the iron stacked porphyrin were probed with transient XUV spectroscopy and transient optical spectroscopy. It was found that an Fe(IV)oxo containing Disproportionated state was not observed for the experimental conditions used for the transient XUV and OTA studies. This information can be used to guide synthetic attempts at stabilizing the Fe(IV)oxo excited stated. With the availability of transient XUV spectroscopy from a tabletop source, immediate feedback of the excited state dynamics can be studied for future synthetically altered iron stacked porphyrins. The stabilization of the Fe(IV)oxo intermediate may lead to a higher yield for the catalysis of oxidation reactions at ambient pressure and temperatures.

4.9.1 Revaluation of Bisporphyrin Dynamics

In the 2003 Nocera study, the bisporphyrins studied, (DPD)Fe_2O shown in transient spectrum, were pumped at 405 nm in an attempt to excite the Ligand to Metal Charge Transfer (LMCT) band.[72] The kinetics of the excited state dynamics were ascertained from single wavelength temporal profiles. Time traces at 530 nm and 565 nm were used as probe wavelengths. With the time resolution available to perform this experiment and examine the kinetic traces, the authors asserted that there is a single transient species with a mono-exponential decay with a 1 ns lifetime of within a 5 ns time window. Upon excitation of the bisporphyrin system, the "sprung open" state appears within 20 ps of the excitation at 405 nm. The lifetime of this transient intermediate state is determined for each bisporphyrin with a value near 1 ns.

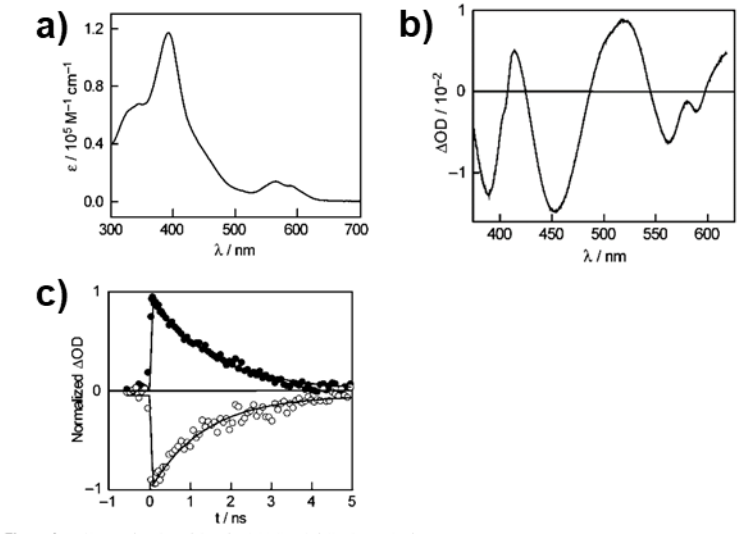

Figure 4.29: a) The electronic absorption spectrum of (DPD)Fe_2O in dry benzene. b) The transient absorption spectrum of the bisporphyrin 20 ps after excitation. c) The time profiles of the bisporphyrin at the probe wavelengths 530 nm (solid dots) and 565 nm (open dots) (figures from reference 72).

According to Figure 4.29a, the electronic absorption spectrum of the bridged bisporphyrin (DPD)Fe_2O contains a large peak near 400 nm, a shoulder near 350 nm, and two small Q-band peaks near 565 nm and 590 nm. The transient absorption spectrum at 20 ps after the 405 nm excitation in Figure 4.29b shows a large bleach near 450 nm, a broad positive feature centered around 520 nm, and small bleaches near 560 nm and 590 nm. When comparing this transient spectrum to the electronic spectrum, the small bleaches past 550 nm at 565 nm and 590

nm are assigned as the bleaches of the small Q-bands of the bisporphyrin. The transient species is assigned as the photoproduct of an LMCT excitation.[72]

The transient spectrum of the bridged bisporphyrin and stacked porphyrin can be compared to speculate the identity of the excited state after excitation near 400 nm, shown in Figure 4.8. To compare the position of the peaks of the transient spectra of the different porphyrins, the position of the transient bleaches and positive features can be compared relative to the ground state electronic spectrum of the respective porphyrin. For the bisporphyrin, the small bleaches past 550 nm correspond to the bleaching of the small Q-bands. For the stacked porphyrin, the bleaches at 560 nm and 605 nm corresponds to the bleaching of the Q-bands near 560 nm and 605 nm. For both the bisporphyrin and stacked porphyrin, the excited state exhibits a bleaching of the Q-bands. For both porphyrin excited state dynamics, there is a bleach near 450 nm. These similar features of the excited states near a 20 ps delay time indicates that the ~ 400 nm excitation of the porphyrins is excited into nearly identical states. This claim that the bisporphyrin from the Nocera study and the stacked porphyrin are following the same dynamics can be supported by the similar kinetics. For the bisporphyrin, with the time resolution available, it appeared that the decay was mono-exponential with a life time near 1 ns for the probe wavelengths 530 nm and 565 nm shown in Figure 4.29c. For the stacked porphyrin kinetics, with a time resolution near 100 fs, the dynamics within the first few picoseconds were determined and indicated a tri-exponential decay. The longest lifetime of the decay determined from global analysis from the 400 nm pump is 840 ps. This long time constant of 840 ps of the stacked porphyrin is near the 1 ns time constant determined for the bisporphyrin. The similarity of the structure of the transient excited state near 20 ps and the lifetime of the excited state for both the stacked and bis porphyrins indicates both complexes are following the same decay pathway. Therefore, conclusions drawn from the analysis of the stacked porphyrin excited state dynamics with the sub-ps time resolution can be applied to the dynamics of the bisporphyrin.

4.10 Acknowledgements

I would like to thank Clare Leahy for her synthesis of the iron stacked porphyrin, sample preparation of the stacked porphyrin solutions for OTA, and for the CTM4XAS simulations. I would also like to thank Yusef Shari'ati for developing the polymer-based film preparation technique.

SUPPORTING INFORMATION

Comparison of Noise with an EDC Liquid Sheet

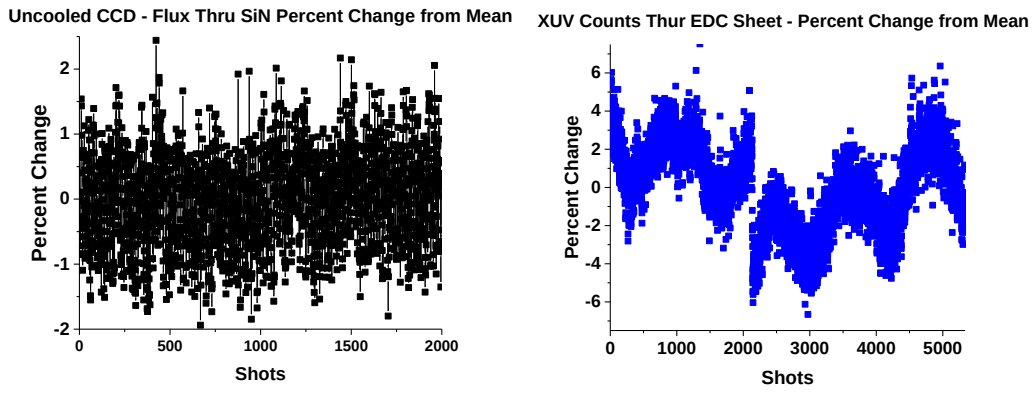

Supplementary Figure 5.1: The percent change from the mean for the XUV counted collected by an uncooled CCD through 100 nm of SiN. The percent change from the mean for the XUV counted collected by an uncooled CCD through an EDC liquid sheet.

Stainless-Steel Dampener Details

To reduce the pulsation caused by the HPLC pump, a simple dampener made with a 3.5-inch stainless-steel tube was used to stabilize the liquid sheet and dampen the pulsation in the liquid sheet. The dampener was assembled upright with the input tubing inserted from the top of the tube down ¾ of the length and the output tubing inserted from the bottom about ½ up the tube. It is essential to have the output tubing above the input tubing. When starting the liquid flow the dampener needs to be filled and pressure needs to be built before the liquid sheet was at the needed flow rate to form a liquid sheet. The liquid is flowed until the liquid level raises and forms an air bubble at the top of the dampener and enough pressure is built up to push liquid out of the outlet tubing. The air bubble at the top of the dampener absorbs the pulsation of the incoming liquid and creates a pulsation-free outlet flow. This method was not ideal because a dead volume of around 20 mL was needed to fill the dampener and maintain a volume needs to stabilize the pulsations. The dampener was unable to mitigate the pulsation for extended periods of time. This method of liquid flow with an HPLC pump and a dampener may be acceptable for spectroscopy techniques that are less susceptible to thickness changes, however, a more stable method was needed for XUV spectroscopy.

Oleophobic Coatings Used

1. 7TECH: Liquid Glass Guard Clear Screen Protector Nano Coating, Super Tempered Oleophobic with 9H Hardness
2. Ewadoo: Nano Liquid Glass Screen Protector, Anti-Scratch, 9H Hardness
3. Smitty's Glass Wax

Sample Cell and Liquid Sheet Holder for XUV Transmission

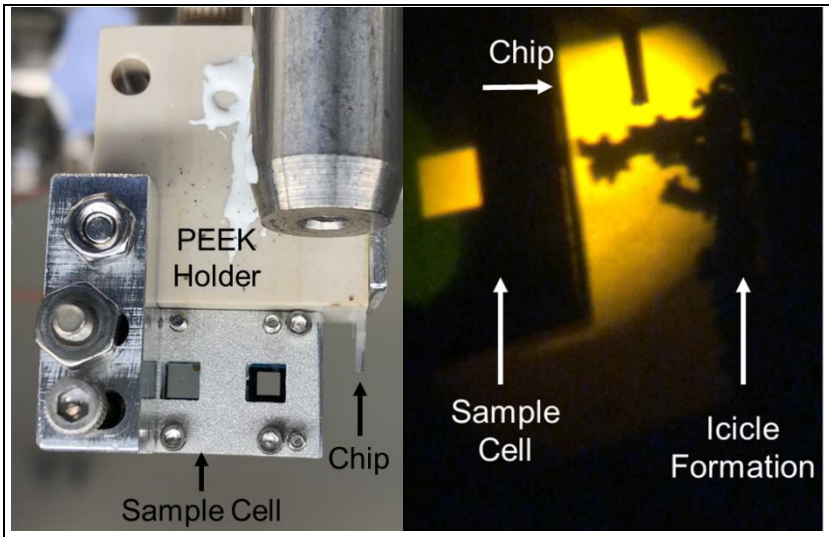

Supplementary Figure 5.2: a) The PEEK holder and sample cell mounted to an optics posted used in the sample chamber for XUV absorption experiments. B) The projection of the chip and sample cell while a liquid sheet of FeTPPCl in EDC is running. An icicle formation is shown below the chip.

CTM4XAS Calculations by Clare Leahy

The M-edge transition diagram for $(TPPFe)_2O$. While the overall complex is antiferromagnetic, each iron is considered separately as a high spin iron(III) in a square planar (D4h) ligand field. The broadband XUV probe excites a set of symmetry-allowed 3p→3d transitions. Electron-electron repulsion splits the $3p^6$-3d5 ground state and 3p5-3d6 core-hole state into the Russel-Saunders states shown. These states are further split due to the symmetry of the ligand field, accounted first through the octahedral field splitting followed by the square planar field splitting as a perturbation on the octahedral field – initial parameters were derived from Ryland *et al* 2018[22], with further modifications dependent on computational calculations and fitting the ground state of the $(TPPFe)_2O$ molecule to account for the minor change in ligand

field from the axial oxygen versus chloride in the monoporphyrin. This resulting ligand field states are designated by the appropriate Mulliken term symbols. Spin-orbit coupling further splits the ligand-field strength. The allowed transitions are determined using the point group-specific transition moment integral. The simulation also includes transition-specific Lorentzian lifetime broadening and 0.2 eV FWHM Gaussian broadening to account for the spectrometer resolution. The LFM method does not calculate absolute peak energies accurately, so both simulations are shifted to match the experimental peak. Finally, a Fano lineshape with q=3.5 is applied to account for interference between Auger and direct photoemission pathways. Primary simulation parameters are shown in Supplementary Table 5.1, additional details on the calculation are given in a previous publication. This calculations were performed using the program CTM4XAS.[33]

Supplementary Table 5.1: Parameters for CTM4XAS simulations for the Stacked Porphyrin Excited States

	Term Symbol	Element	Charge	Scaling of Slater integrals			SOC	Crystal Field Parameters		
				fdd	fpd	gpd		10Dq	Ds	Dt
S = 5/2	$^6A_{1g}$	Fe	3+	1	0.625	0.625	1	2.5	.15	.07
S = 2	$^5A_{1g}$	Fe	2+	1	0.625	0.625	1	2.5	.15	.07
S = 2	$^5A_{1g}$	Fe	4+	1	0.625	0.625	1	2.5	.15	.07

Contour Plots of The Stacked Porphyrin OTA Results

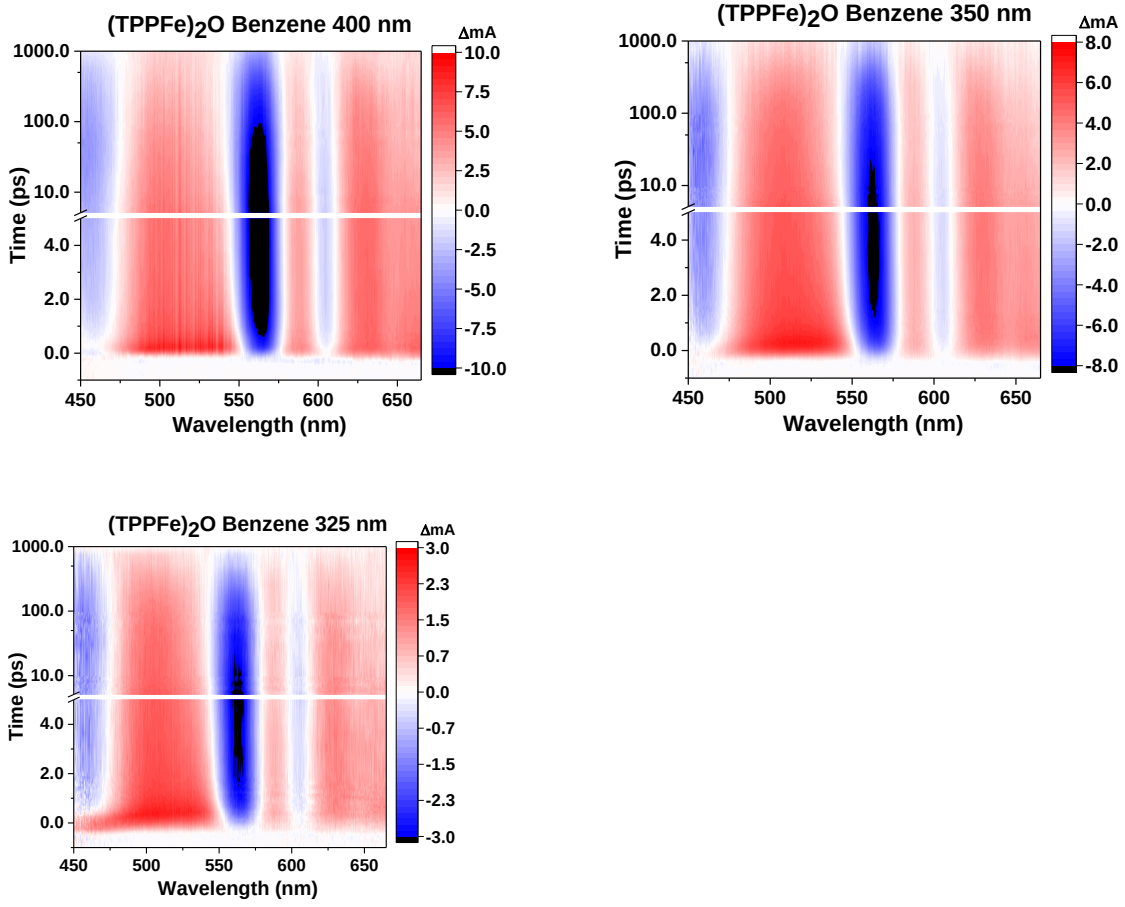

Supplementary Figure 5.3: The contour plots of the transient optical absorption of the iron stacked porphyrin in benzene pumped at 400 nm, 350 nm, and 325 nm.

Kinetic Modeling for the Stacked Porphyrin Pumped at 400 nm

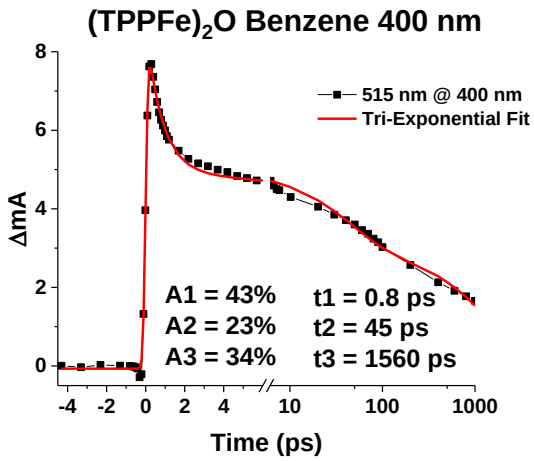

Supplementary Figure 5.4: The tri-exponential fit of the prove wavelength 515 nm for a solution of the stacked porphyrin in benzene pumped at 400 nm. The kinetic fit is poor at times between 10 ps and 100 ps. The second lifetime of τ_2 = 45 ps is significantly different from the time scales of the second lifetime for the stacked porphyrin pumped at 350 nm and 325 nm.

Three State Parallel Model for the OTA of the Stacked Porphyrin

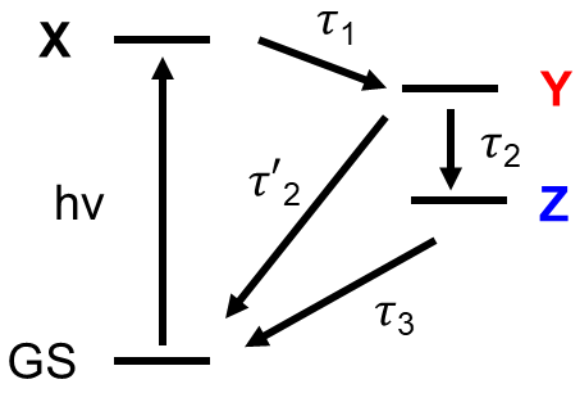

Supplementary Figure 5.5: Three State Parallel Model for Stacked Porphyrin OTA

A Three State Parallel Model was used to determine if the State Y and State Z represented a hot and cold excited state with State Y being the hot excited state and State Z being the cold excited state. The parallel model shows state that the initial State X relaxes into the hot excited State Y. In the hot excited state, the model branching with some of the population relaxing back to the ground state and another portion of the population relaxing into the cold excited state Z. The remaining population in State Z then relaxes into the ground state. This model was proposed because of the similar of the component spectra representing State Y and State Z in the three-state sequential model. The similarity of spectral features suggested that the two states may be representing the same excited state in a hot or cold state. This model was used to fit the data set; however, it was found that the fit of data did not improve with this model compared to the three-state sequential model. Supplementary Figure 5.6 below shows the fit from the parallel model does not fit the time trace of 515 nm from the stacked porphyrin in benzene pumped at 400 nm well after 10 ps. This suggests that there is not a population from State Z that relaxing to the ground state before relaxing through State Z.

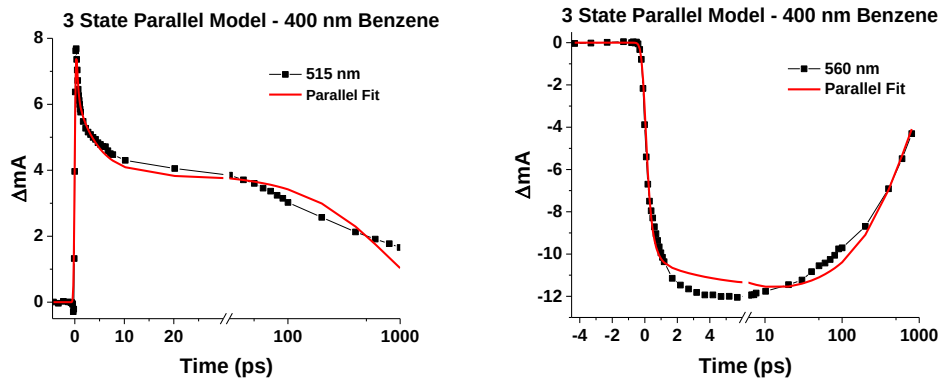

Supplementary Figure 5.6: Times traces at 515 and 560 nm for the stacked porphyrin in benzene pumped at 400 nm with the reconstructed traces from the three-state parallel global analysis model. The constants determined were τ_1 = 0.3 ps, τ'_2 = 14 ps, τ_2 = 6.3 ps, and τ_3 = 750 ps.

Kinetic Fits of the Three State Sequential Model

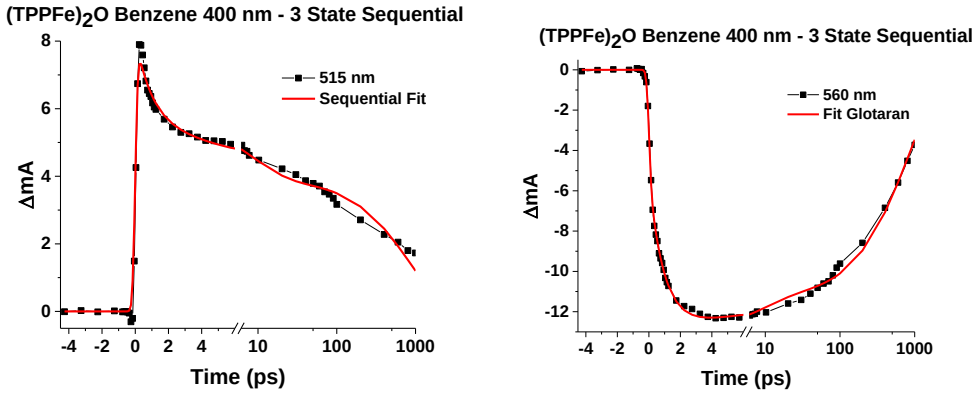

Supplementary Figure 5.7: Times traces at 515 nm and 560 nm for the stacked porphyrin in benzene pumped at 400 nm with the reconstructed traces from the three-state parallel global analysis model. The constants determined were τ_1 = 1 ps, τ_2 = 8.6 ps, and τ_3 = 840 ps. The model fits the data well for the 515 nm and 560 nm probe wavelength.

Kinetic Modeling of the Stacked Porphyrin OTA in Polystyrene Films

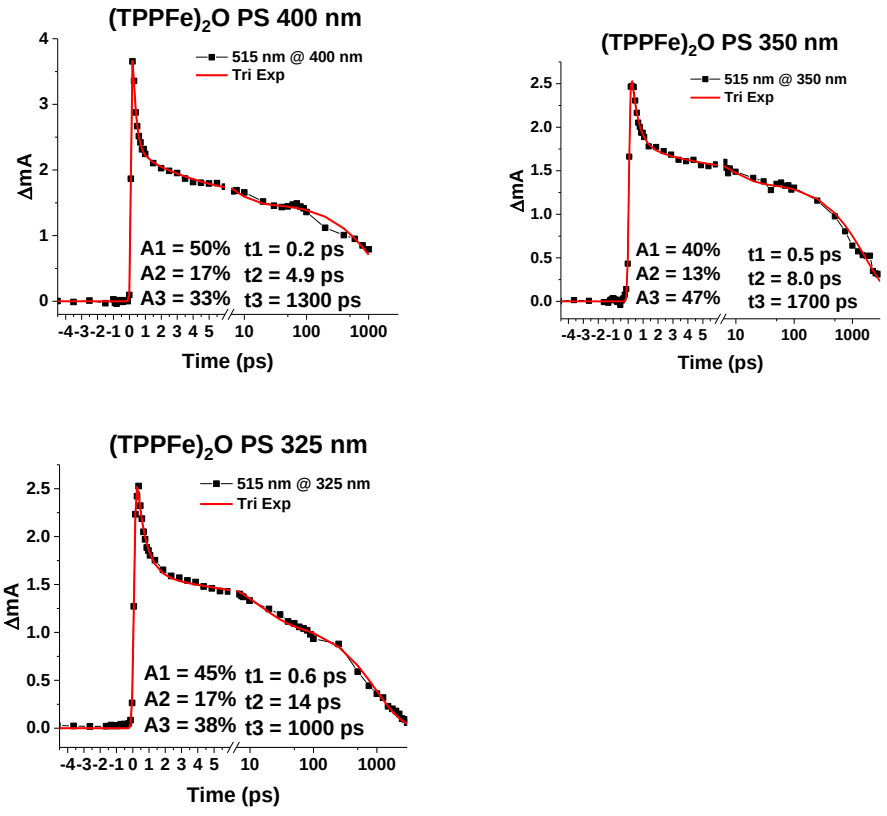

Supplementary Figure 5.8: The time traces at 515 nm for the stacked porphyrin in a polystyrene film pumped at 400 nm, 350 nm, and 325 nm.

Comparison of the Component Spectra of the Stacked Porphyrin Pumped at 350 and 325 nm to the Fe(IV) Simulated Difference Spectrum

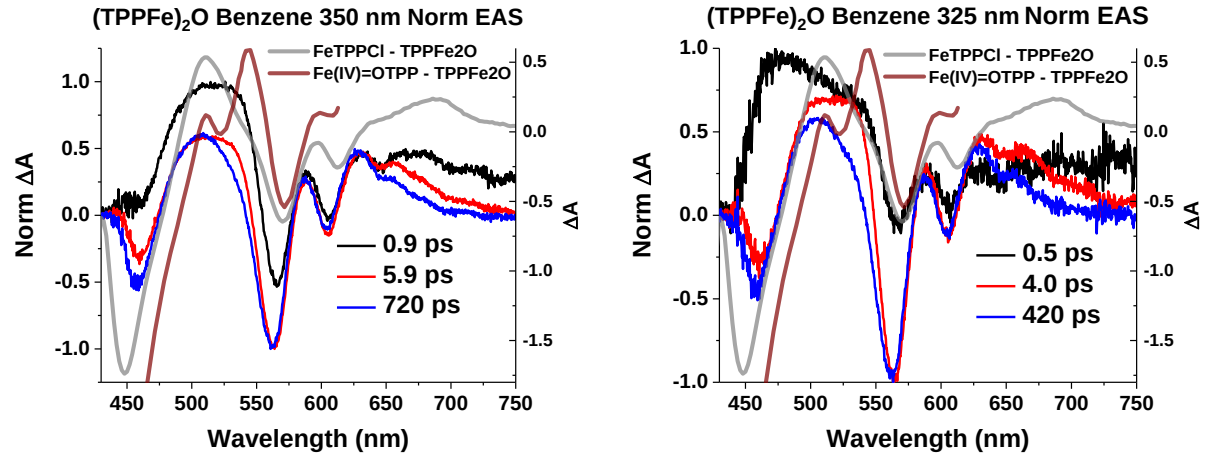

Supplementary Figure 5.9: a) The component spectra of the stacked porphyrin pumped at 350 nm in benzene model with a 3-state sequential model. b) The component spectra of the stacked porphyrin pumped at 325 nm in benzene model with a 3-state sequential model. Both figures contain the difference spectra of the stacked porphyrin subtracted from FeTPPCl, which is meant to simulate an Fe(III) excited state and the difference spectra of the stacked porphyrin subtracted from Fe(IV)=OTPP, which is meant to simulate an Fe(IV) excited state.

Supplementary Table 5.2: Kinetic Analysis results of 515nm probe wavelength of Stacked Porphyrin in varying solvent with varying pump wavelengths.

Pump 325 nm Solvent	τ_1 (ps)	τ_2 (ps)	τ_3 (ps)	Power	Excitation Fraction	Energy (μJ)	Pump Fluence (mJ/cm^2)
Benzene	0.9 (0.3)	7 (3)	830 (40)	0.7	5.7	0.7	0.86
DCM	0.89 (0.07)	54 (10)	1100 (70)	0.7	3.4	0.7	0.86
THF	0.7 (0.1)	11 (3)	820 (44)	0.7	3.3	0.7	0.86

Pump 350 nm Solvent	τ_1 (ps)	τ_2 (ps)	τ_3 (ps)	Power (mW)	Excitation Fraction	Energy (μJ)	Pump Fluence (mJ/cm^2)
Benzene	0.9 (0.2)	7 (2)	940 (30)	1.4	8.3	1.72	1.4
DCM	0.2 (0.1)	11(4)	880 (140)	1.4	7.2	1.72	1.4
THF	0.36 (0.4)	5.5 (0.5)	750 (35)	1.4	6.4	1.72	1.4

Pump 400 nm Solvent	τ_1 (ps)	τ_2 (ps)	τ_3 (ps)	Power	Excitation Fraction	Energy (μJ)	Pump Fluence (mJ/cm^2)
Benzene	0.81 (0.06)	45 (7)	1600 (230)	1.2	21.5	1.2	1.4
DCM	0.25 (0.01)	27 (2)	1110 (60)	0.6	9.6	0.6	1.4
THF	0.19 (0.02)	19 (2)	1240 (70)	0.6	7.1	0.6	0.7

Solvation and solvent polarity of the Stacked Porphyrin

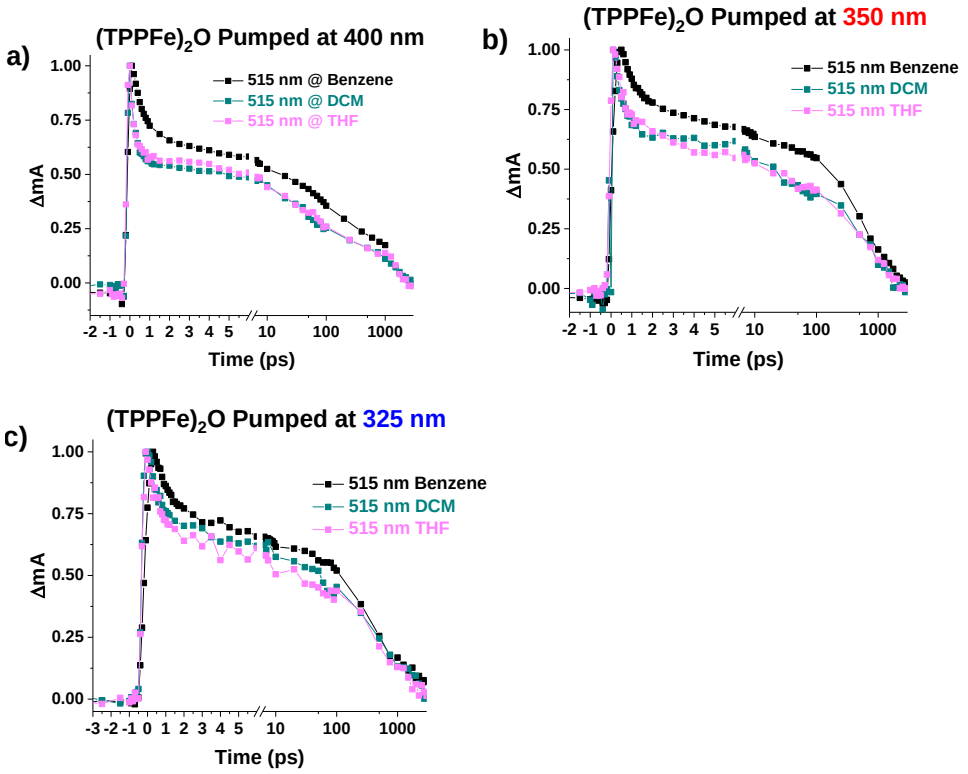

Supplementary Figure 5.10: The normalized time traces of stacked porphyrin pumped at a) 400 nm, b) 350 nm, and c) 325 nm in various solvents.

The solvents used for optical absorption spectroscopy of the stacked porphyrin were dry benzene, dichloromethane (DCM), and tetrahydrofuran (THF). The polarity of the solvents are as follows benzene (0.111), tetrahydrofuran (0.207) and dichloromethane (0.309).[36] This range of polarity was chosen to see if the polarity would have an effect on the lifetime of the stacked porphyrin excited state or the decay mechanism. Previous studies of FeTPPCl[23], FeTMPyP[37], and CoTPP[38] have shown that the polarity and coordinating ability of the solvent affected the lifetime of the initial LMCT state but did not alter the relaxation mechanism.[22] In the study of FeTPPCl, three different solvent environments were used to show the ultrafast dynamics upon excitation.[23] It was found that the spectrum of the LMCT state was slightly dependent on the solvent environment. According to Supplementary Table 5.2, the lifetime of the first state excited state varies for the stacked porphyrin at the probe wavelength of 515 nm at pump wavelengths 325 nm, 350 nm, and 400 nm, in various solvents used. Supplementary Figure 5.10

shows the difference in the lifetime of the initial state with solvents of varying polarity suggest that the initial state may be an LMCT state. The solvent difference does not alter the identity of the excited state therefore, not affecting the relaxation dynamics.

Comparison of the Mono- and Stacked Porphyrin XUV Ground State

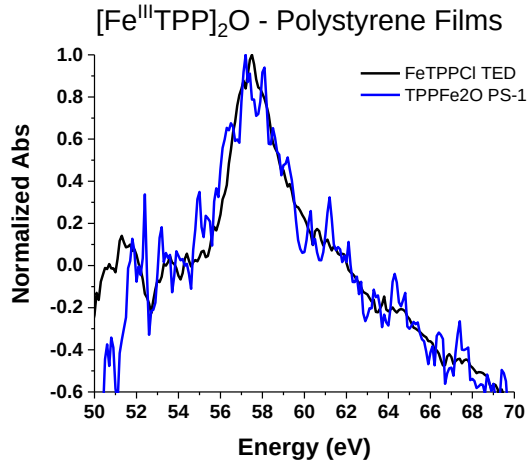

Supplementary Figure 5.11: Comparison of the XUV ground state of a polystyrene thin film of the stacked porphyrin (TPPFe)2O compared to a thermally evaporated film of the monoporphyrin Fe(III)TPPCl. The peak of both iron complexes occurs at 57.4 eV indicating that both complexes contain Fe(III) centers. Both ground state spectra are normalized to compare the location of the peaks.

Biexponential Fit of the tXUV Positive Feature

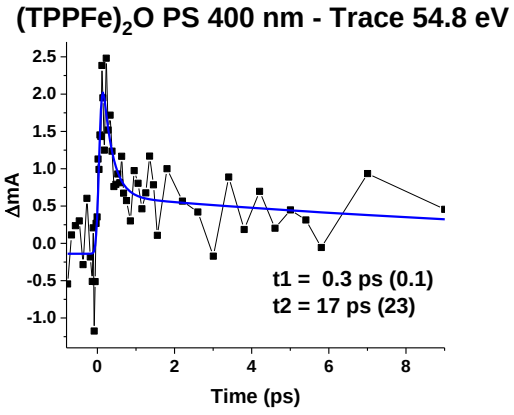

Supplementary Figure 5.12: The time trace at 54.8 eV for the stacked porphyrin pumped at 400 nm. The time trace is fit with a bi-exponential function. The function fits the data well however the error for the second time constant is larger and greater in value than the time constant.

REFERENCES

1. de Groot, F. M. F. & Kotani, A. *Core Level Spectroscopy of Solids*. (CRC Press, 2008).

2. Kraus, P. M., Zürch, M., Cushing, S. K., Neumark, D. M. & Leone, S. R. The ultrafast X-ray spectroscopic revolution in chemical dynamics. *Nat. Rev. Chem.* **2**, 82–94 (2018).

3. Zhang, K. *et al.* Shrinking the Synchrotron: Tabletop Extreme Ultraviolet Absorption of Transition-Metal Complexes. *J. Phys. Chem. Lett.* **7**, 3383–3387 (2016).

4. Geneaux, R., Marroux, H. J. B., Guggenmos, A., Neumark, D. M. & Leone, S. R. Transient absorption spectroscopy using high harmonic generation: A review of ultrafast X-ray dynamics in molecules and solids. *Philos. Trans. R. Soc. A Math. Phys. Eng. Sci.* **377**, (2019).

5. La-O-Vorakiat, C. *et al.* Ultrafast demagnetization dynamics at the M edges of magnetic elements observed using a tabletop high-harmonic soft X-ray source. *Phys. Rev. Lett.* **103**, 1–4 (2009).

6. Zhang, K., Ash, R., Girolami, G. S. & Vura-Weis, J. Tracking the Metal-Centered Triplet in Photoinduced Spin Crossover of Fe(phen)32+ with Tabletop Femtosecond M-Edge X-ray Absorption Near-Edge Structure Spectroscopy. *J. Am. Chem. Soc.* **141**, 17180–17188 (2019).

7. Benke, K. Ultrafast Extreme Ultraviolet Spectroscopy of Transition Metal Dithiolate Coordination Complexes. (University of Illinois Urbana-Champaign, 2021).

8. Ryland, E. S. *et al.* Tabletop Femtosecond M-edge X-ray Absorption Near-Edge Structure of FeTPPCl: Metalloporphyrin Photophysics from the Perspective of the Metal. *J. Am. Chem. Soc.* **140**, 4691–4696 (2018).

9. Ryland, E. S., Zhang, K. & Vura-Weis, J. Sub-100 fs Intersystem Crossing to a Metal-Centered Triplet in Ni(II)OEP Observed with M-Edge XANES. *J. Phys. Chem. A* (2019). doi:10.1021/acs.jpca.9b03376

10. Lin, M. F. *et al.* Carrier-Specific Femtosecond XUV Transient Absorption of PbI2Reveals Ultrafast Nonradiative Recombination. *J. Phys. Chem. C* **121**, 27886–27893 (2017).

11. Porter, I. J. *et al.* Photoexcited Small Polaron Formation in Goethite (α-FeOOH) Nanorods Probed by Transient Extreme Ultraviolet Spectroscopy. *J. Phys. Chem. Lett.* **9**, 4120–4124 (2018).

12. Popmintchev, T., Chen, M. C., Arpin, P., Murnane, M. M. & Kapteyn, H. C. The attosecond nonlinear optics of bright coherent X-ray generation. *Nat. Photonics* **4**, 822–832 (2010).

13. Sutherland, J. R. *et al.* High harmonic generation in a semi-infinite gas cell. *Opt. Express* **12**, 4430 (2004).

14. Smith, A. D. *et al.* Femtosecond Soft-X-ray Absorption Spectroscopy of Liquids with a Water-Window High-Harmonic Source. *J. Phys. Chem. Lett.* **11**, 1981–1988 (2020).

15. Cirmi, G. *et al.* Cut-off scaling of high-harmonic generation driven by a femtosecond visible optical parametric amplifier. *J. Phys. B At. Mol. Opt. Phys.* **45**, 1–10 (2012).

16. Sun, H.-W. *et al.* Extended phase matching of high harmonic generation by plasma-induced defocusing. *Optica* **4**, 976 (2017).

17. Chang, Z. *et al.* Temporal phase control of soft-x-ray harmonic emission. *Phys. Rev. A - At. Mol. Opt. Phys.* **58**, R30–R33 (1998).

18. Takahashi, E., Nabekawa, Y., Nurhuda, M. & Midorikawa, K. Generation of high-energy high-order harmonics by use of a long interaction medium. *J. Opt. Soc. Am. B* **20**, 158 (2003).

19. Ash, R. Probing the Reaction Coordinate of Photoinduced Spin-Crossover with Femtosecond M-Edge XANES. (University of Illinois at Urbana-Champaign, 2020).

20. Verkamp, M. A. Transient extreme ultraviolet spectroscopy of semiconductors. (University of Illinois, 2019).

21. Baker, M. L. *et al.* K- and L-edge X-ray absorption spectroscopy (XAS) and resonant inelastic X-ray scattering (RIXS) determination of differential orbital covalency (DOC) of transition metal sites. *Coord. Chem. Rev.* **345**, 182–208 (2017).

22. Limonov, M. F., Rybin, M. V., Poddubny, A. N. & Kivshar, Y. S. Fano resonances in

photonics. *Nat. Photonics* **11**, 543–554 (2017).

23. Vura-Weis, J. *et al.* Femtosecond M2,3-edge spectroscopy of transition-metal oxides: Photoinduced oxidation state change in α-Fe2O3. *J. Phys. Chem. Lett.* **4**, 3667–3671 (2013).

24. Stavitski, E. & de Groot, F. M. F. The CTM4XAS program for EELS and XAS spectral shape analysis of transition metal L edges. *Micron* **41**, 687–694 (2010).

25. Ash, R., Zhang, K. & Vura-Weis, J. Photoinduced valence tautomerism of a cobalt-dioxolene complex revealed with femtosecond M-edge XANES. *J. Chem. Phys.* **151**, (2019).

26. Ferreira, G. K. B., Carvalho, C. & Nakagaki, S. Studies of the catalytic activity of iron (III) porphyrins for the protection of carbonyl groups in homogeneous media. *Catalysts* **9**, 1–14 (2019).

27. Yi, J., Nakatani, N. & Nomura, K. Solution XANES and EXAFS analysis of active species of titanium, vanadium complex catalysts in ethylene polymerisation/dimerisation and syndiospecific styrene polymerisation. *Dalton Trans.* **49**, 8008–8028 (2020).

28. Della Longa, S. *et al.* Redox-induced structural dynamics of Fe-heme ligand in myoglobin by x-ray absorption spectroscopy. *Biophys. J.* **85**, 549–558 (2003).

29. Shelby, M. L. *et al.* Ultrafast Excited State Relaxation of a Metalloporphyrin Revealed by Femtosecond X - ray Absorption Spectroscopy. (2016). doi:10.1021/jacs.6b02176

30. CXRO - The Center for X-ray Optics.

31. Lin, M.-F., Verkamp, M. A., Ryland, E. S., Zhang, K. & Vura-Weis, J. Impact of spatial chirp on high-harmonic extreme ultraviolet absorption spectroscopy of thin films. *J. Opt. Soc. Am. B* **33**, 1986 (2016).

32. Baker, L. R. *et al.* Charge carrier dynamics of photoexcited Co3O4in methanol: Extending high harmonic transient absorption spectroscopy to liquid environments. *Nano Lett.* **14**, 5883–5890 (2014).

33. Ekimova, M., Quevedo, W., Faube, M., Wernet, P. & Nibbering, E. T. J. A liquid flatjet

system for solution phase soft-x-ray spectroscopy. *Struct. Dyn.* **2**, (2015).

34. Bush, J. W. M. & Hasha, A. E. On the collision of laminar jets: Fluid chains and fishbones. *J. Fluid Mech.* **511**, 285–310 (2004).

35. Watanabe, A., Saito, H., Ishida, Y., Nakamoto, M. & Yajima, T. A new nozzle producing ultrathin liquid sheets for femtosecond pulse dye lasers. *Opt. Commun.* **71**, 301–304 (1989).

36. Runge, P. K. & Rosenberg, R. Unconfined flowing-dye films for cw dye lasers. *IEEE J. Quantum Electron.* **8**, 910–911 (1972).

37. Galinis, G. *et al.* Micrometer-thickness liquid sheet jets flowing in vacuum. *Rev. Sci. Instrum.* **88**, 1–8 (2017).

38. Kubin, M. *et al.* Direct Determination of Absolute Absorption Cross Sections at the L-Edge of Dilute Mn Complexes in Solution Using a Transmission Flatjet. *Inorg. Chem.* **57**, 5449–5462 (2018).

39. Kubin, M. *et al.* Cr L-Edge X-ray Absorption Spectroscopy of CrIII(acac)3 in Solution with Measured and Calculated Absolute Absorption Cross Sections. *J. Phys. Chem. B* **122**, 7375–7384 (2018).

40. Kleine, C. *et al.* Soft X - ray Absorption Spectroscopy of Aqueous Solutions Using a Table-Top Femtosecond Soft X-ray Source. *J. Phys. Chem. Lett.* **10**, 52–58 (2019).

41. Koralek, J. D. *et al.* Generation and characterization of ultrathin free-flowing liquid sheets. *Nat. Commun.* **9**, 1–8 (2018).

42. Miller, N. A. *et al.* Polarized XANES monitors femtosecond structural evolution of photoexcited Vitamin B12. *J. Am. Chem. Soc.* **139**, 1894–1899 (2017).

43. Janik, I., Lisovskaya, A. & Bartels, D. M. Partial Molar Volume of the Hydrated Electron. *J. Phys. Chem. Lett.* **10**, 2220–2226 (2019).

44. Kuphaldt, T. R. *Lessons In Industrial Instrumentation*. (Samurai Media Limited, 2017).

45. Choo, Y. J. & Kang, B. S. Parametric study on impinging-jet liquid sheet thickness distribution using an interferometric method. *Exp. Fluids* **31**, 56–62 (2001).

46. Stenzel, O. *The Physics of Thin Film Optical Spectra: An Introduction*. *Springer Series in Surface Sciences* **44**, (2016).

47. Spectral Reflectance Calculator for Thin-Film Stacks.

48. Converting a spectrum to a colour.

49. Bremond, N. & Villermaux, E. Atomization by jet impact. *J. Fluid Mech.* **549**, 273–306 (2006).

50. Yang, J., Zhang, Z., Men, X., Xu, X. & Zhu, X. A simple approach to fabricate superoleophobic coatings. *New J. Chem.* **35**, 576–580 (2011).

51. Sumner, A. L. *et al.* Implications for Heterogeneous Chemistry in the Troposphere. *Phys. Chem. Chem. Phys.* **6**, 604–613 (2004).

52. Rury, A. S. & Sension, R. J. Broadband ultrafast transient absorption of iron (III) tetraphenylporphyrin chloride in the condensed phase. *Chem. Phys.* **422**, 220–228 (2013).

53. Walker, F. A. & Simonis, U. *Iron Porphyrin Chemistry*. *Encyclopedia of Inorganic and Bioinorganic Chemistry* **23**, (2011).

54. Wilson, K. R. *et al.* Investigation of volatile liquid surfaces by synchrotron x-ray spectroscopy of liquid microjets. *Rev. Sci. Instrum.* **75**, 725–736 (2004).

55. Ryland, E. S. Ultrafast Photophysics of Transition Metal Coordination Complexes Studied with Femtosecond Extreme Ultraviolet Transient Absorption Spectroscopy. (Univeristy of Illinois at Urbana-Champaign, 2019).

56. Jordan, S. L. & Taylor, L. T. HPLC Separation with Solvent Elimination FTIR Detection of Polymer Additives. *J. Chromatogr. Sci.* **35**, 7–13 (1997).

57. Maldotti, A. *et al.* Photochemistry of Iron-porphyrin complexes. Biomimetics and catalysis. *Coord. Chem. Rev.* **125**, 143–154 (1993).

58. Peterson, M. W., Rivers, S. & Richman, R. M. Mechanistic Considerations in the Photodisproportionation of Mu-Oxo-bis((tetraphenylporphinato)iron(III)). *J. Am. Chem. Soc.* **107**, 2907–2915 (1985).

59. Moody, P. C. E. & Raven, E. L. The Nature and Reactivity of Ferryl Heme in Compounds i and II. *Acc. Chem. Res.* **51**, 427–435 (2018).

60. Fleischer, E. B. & Srivastava, T. S. The Structure and Properties of μ-Oxo-bis(tetraphenylporphineiron(III)). *J. Am. Chem. Soc.* **91**, 2403–2405 (1969).

61. Guest, C. R., Straub, K. D., Hutchinson, J. A. & Rentzepis, P. M. Picosecond Absorption Studies on the Excited State of (μ-Oxo)bis[(tetraphenylporphinato)iron(III)]. *J. Am. Chem. Soc.* **110**, 5276–5280 (1988).

62. Hofmann, J. A. & Bocian, D. F. Resonance Raman spectra of oxygen- and nitrogen-bridged iron octaethylporphyrin dimers. *J. Phys. Chem.* **88**, 1472–1479 (1984).

63. Hoffman, A. B. *et al.* The Crystal Structure and Molecular Stereochemistry of μ-Oxo-bis[α,β,γ,δ-tetraphenylporphinatoironCIII)]. *J. Am. Chem. Soc.* **94**, 3620–3626 (1972).

64. Rosenthal, J., Pistorio, B. J., Chng, L. L. & Nocera, D. G. Aerobic Catalytic Photooxidation of Olefins by an Electron-Deficient Pacman Bisiron (III) μ -Oxo Porphyrin. *J. Org. Chem.* **70**, 1885–1888 (2005).

65. Richman, R. M. & Peterson, M. W. Photodisproportionation of .mu.-Oxo-bis[(tetraphenylporphinato)iron(III)]. *J. Am. Chem. Soc.* **104**, 5795–5796 (1982).

66. Pistorio, B. J., Chang, C. J. & Nocera, D. G. A phototriggered molecular spring for aerobic catalytic oxidation reactions. *J. Am. Chem. Soc.* **124**, 7884–7885 (2002).

67. Chang, C. J. *et al.* Structural, spectroscopic, and reactivity comparison of xanthene- and dibenzofuran-bridged cofacial bisporphyrins. *Inorg. Chem.* **41**, 3102–3109 (2002).

68. Rodgers, K. R., Reed, R. A., Spiro, T. G. & Su, Y. O. Resonance Raman and Magnetic Resonance Spectroscopic Characterization of the Fe(I), Fe(II), Fe(III), and Fe(IV) Oxidation States of Fe(2-TMPyP)n+(AQ). *Inorg. Chem.* **31**, 2688–2700 (1992).

69. Hashimoto, S., Tatsuno, Y. & Kitagawa, T. Observation of the Feiv=0 Stretching Raman Band for a Ferryl Porphyrin π Cation Radical. *J. Am. Chem. Soc.* **109**, 8096–8097 (1987).

70. Hashimoto, S., Mizutani, Y., Tatsuno, Y. & Kitagawa, T. Resonance Raman Characterization of Ferric and Ferryl Porphyrin π Cation Radicals and the FeIV=O

Stretching Frequency. *J. Am. Chem. Soc.* **113**, 6542–6549 (1991).

71. Chin, D.-H., Balch, A. & La Mar, G. N. Formation of Porphyrin Ferryl (FeO2+) Complexes through the Addition of Nirtrogen Bases to Peroxo-Bridged Iron(III) Porphyrins. *J. Am. Chem. Soc.* **102**, 1446–1448 (1980).

72. Hodgkiss, J. M., Chang, C. J., Pistorio, B. J. & Nocera, D. G. Transient Absorption Studies of the Pacman Effect in Spring-Loaded Diiron (III) μ -Oxo Bisporphyrins. *Inorg. Chem.* **42**, 8270–8277 (2003).

73. Helms, J. H. *et al.* Effect of Meso Substituents on Exchange-Coupling Interactions in μ-Oxo Iron(III) Porphyrin Dimers. *Inorg. Chem.* **25**, 2334–2337 (1986).

74. Peterson, M. W. & Richman, R. M. Photodisproportionation of (μ-Oxo)bis((tetrakis(4-carboxyphenyl)porphinato)iron(III)). *Inorg. Chem.* **24**, 722–725 (1985).

75. Goutermann, M. *Optical Spectra and Electronic Structure of Porphyrins and Related Rings. The Porphyrins* **Ill**, (ACADEMIC PRESS, INC., 1978).

76. Paulat, F. & Lehnert, N. Detailed Assignment of the Magnetic Circular Dichroism and UV - vis Spectra of Five-Coordinate High-Spin Ferric [Fe (TPP)(Cl)]. *Inorg. Chem.* **7**, 4963–4976 (2008).

77. Hendrickson, D. N., Kinnaird, M. G. & Suslick, K. S. Photochemistry of (5,10,15,20-Tetraphenylporphyrinato)iron(III) Halide Complexes, Fe(TPP)(X). *J. Am. Chem. Soc.* **109**, 1243–1244 (1987).

78. Rury, A. S., Goodrich, L. E., Galinato, M. G. I., Lehnert, N. & Sension, R. J. Ligand recruitment and spin transitions in the solid-state photochemistry of Fe (III)TPPCl. *J. Phys. Chem. A* **116**, 8321–8333 (2012).

79. Borrego-Varillas, R., Ganzer, L., Cerullo, G. & Manzoni, C. Ultraviolet transient absorption spectrometer with Sub-20-fs time resolution. *Appl. Sci.* **8**, 1–18 (2018).

80. Duda, M., Novák, O., Chyla, M., Smrž, M. & Mocek, T. Balancing the conversion efficiency and beam quality of second harmonic generation of a two-picosecond Yb:YAG thin-disk laser. *Laser Phys.* **30**, (2020).

81. Shari'ati, Y. & Vura-Weis, J. Polymer Thin Films for Extreme Ultraviolet Absorption Spectroscopy. *Unpubl. Work* Urbana, IL (2021).

82. Snellenburg, J. J., Laptenok, S., Seger, R., Mullen, K. M. & van Stokkum, I. H. M. Glotaran: A Java-based graphical user interface for the R package TIMP. *J. Stat. Softw.* **49**, 1–22 (2012).

83. Gao, D., Aly, S. M., Karsenti, P. L., Brisard, G. & Harvey, P. D. Increasing the lifetimes of charge separated states in porphyrin-fullerene polyads. *Phys. Chem. Chem. Phys.* **19**, 24018–24028 (2017).

84. Hayes, D. *et al.* Electronic and nuclear contributions to time-resolved optical and X-ray absorption spectra of hematite and insights into photoelectrochemical performance. *Energy Environ. Sci.* **9**, 3754–3769 (2016).